Multiple Particle Tracking to Assess the Microstructure of Biological Fluids

by

Thierry Savin

Submitted to the Department of Chemical Engineering
in partial fulfillment of the requirements for the degree of

Doctor of Philosophy

at the

MASSACHUSETTS INSTITUTE OF TECHNOLOGY

August 2006

© Massachusetts Institute of Technology 2006. All rights reserved.

Author_____

Department of Chemical Engineering
August 29, 2006

Certified by_____

Patrick S. Doyle
Doherty Associate Professor of Chemical Engineering
Thesis Supervisor

Accepted by_____

William M. Deen
Professor of Chemical Engineering
Chairman of the Committee for Graduate Students

Multiple Particle Tracking to Assess the Microstructure of Biological Fluids

by
Thierry Savin

Submitted to the Department of Chemical Engineering
on August 29, 2006, in partial fulfillment of the
requirements for the degree of
Doctor of Philosophy

Abstract

Tracking the Brownian motion of colloids was first used about a hundred years ago to demonstrate the molecular nature of matter. Today's colloidal scientists perform particle tracking experiments to assess the structural and mechanical properties of complex materials at a micron length scale. Indeed, the dynamics of micron sized probe particles embedded in a material can be related to the local mechanical response of the system. This probing technique, called microrheology, has received much interest in the last few decades due to the importance of a materials local properties in its function and its macro-scale characteristics. These new assessments are especially relevant in soft matter sciences such as biophysics.

Video microscopy particle tracking is an easy technique to implement experimentally. Movies of the fluctuating particles in a sample are recorded and analyzed off-line using custom algorithms. For this reason, it is widely used in studies of soft matter properties and in fluid dynamics. However, behind this apparent simplicity lie a number of subtle limitations that can alter significantly the validity of the measurements. The focus of the parts of this thesis is an exhaustive characterization of the errors incurred in the standard video microscopy particle tracking setup. Detailed understanding of these errors led to new methods to circumvent some of the intrinsic limitations.

The trajectories extracted from particle tracking are used to compute the mean-squared displacement that characterizes the dynamics of the probe particles. This measurement suffers from two kinds of limitations: the finite spatial resolution in the particle localization and statistical uncertainties. The source of localization errors was separated into two separate contributions. A "static error" arises in the position measurements of immobilized particles. A "dynamic error" comes from the particle motion during the finite exposure time that is required for visualization. We calculated the propagation of these errors on the mean-squared displacement and examined the impact of our analysis on theoretical model fluids used in biorheology. These theoretical predictions were verified for purely viscous fluids using simulations and a multiple particle tracking technique performed with video microscopy. We showed that the static contribution could be confidently corrected in dynamics studies by using static experiments performed at a similar noise-to-signal ratio. This groundwork allowed us to achieve higher resolution in the mean-squared displacement, and thus to increase the accuracy of microrheology studies.

When using video microscopy, tracking of a particle is possible only for the given duration when it travels within a finite volume of observation. Because the Brownian motion is stochastic, a statistical study is required to characterize this trajectory duration. We showed that the effect of a finite imaging volume leads to a peculiar sampling of material local properties. By thoroughly mod-

eling the sampling design, we derived estimators for the mean and variance of particle's dynamics that are independent, under well-defined conditions, of the peculiar statistics of the measurement output. These estimators serve to quantify a material heterogeneity.

Having gained a full characterization of the technique, we applied video multiple particle tracking to study a complex time-evolving system of self-assembling peptides. This material undergoes a transition from a purely viscous solution to an elastic hydrogel through the molecular assembly of the peptides into a fibrous network. We used the oligo-peptide KFE8 as a model self-assembling peptide and assessed the dependency of the gelation kinetics with the pH of the solution. We were able to develop a theoretical model for this dependency by using the Derjaguin-Landau-Verwey-Overbeek (DLVO) theory for the interaction between the peptides.

Thesis Supervisor: Patrick S. Doyle
Title: Doherty Associate Professor of Chemical Engineering

Acknowledgments

" Un seul mot, usé, mais qui brille comme une vieille pièce de monnaie : merci ! "
- Pablo Neruda

Although a PhD thesis is an individual accomplishment, this work could not have been completed without the help and support of many people. I would like to first express my gratitude to my advisor Patrick Doyle for guiding me through my research in the last five years. His methodical approach and planning (in contrast to my proclivity for disorganization) have shielded me against the vagaries of PhD student life, both academic and administrative, and taught me valuable lessons for the future. I thank the members of my thesis committee, Roger Kamm and Shuguang Zhang, for the motivating discussions we had and valuable advice I received through the course of my thesis. I would like to thank the members of the Doyle group for providing a great atmosphere in the office and for accompanying me through my academic journey during these past years. I am specially indebted to Patrick Underhill and Ramin Haghgooie, who joined the group at the same time as I did, for countless exchanges. I also thank Greg Randall for tutoring me during my first steps in the microscopy lab. Far from home, I was still receiving support from the old friends I left in Paris. I especially think of Julie, Ronan, Jan and Omri who came to visit me. "Merci les p'tits gars". Here in Cambridge, I received support from new friends. They include -in chronological order- Sam, Kirill, Joanna, Cindy, Alan, Carine, and Kelly. Thank you. Many others, too numerous to name, have also helped me to find life outside the lab, and I thank them for that. Finally I would like to express my gratitude and affection to my parents, my sister, my two brothers, my two little nieces (they were little at the time of writing) and their father. I dedicate this thesis to my mom and dad for their endless and unstinted support.

Funding for this research was provided by the DuPont-MIT Alliance.

Table of Contents

List of Figures

CHAPTER 1

Introduction

Colloidal suspensions exhibit formidable properties, and colloid science originated from stunning discoveries concerning the behavior of the suspended particles. The fact that thermal fluctuations are *observable* at the length scale of colloidal particles both provided with the primordial key to the establishment of statistical thermodynamics, but also justifies the actual importance of current studies in modern soft-matter science such as biophysics. At colloidal length scales structures are formed and functions exist under the influence of thermal energy and other comparably weak forces [1, 2]. Particle sizes in colloidal systems typically range from several nanometers to tenth of microns [2]. These length scales are large enough for straightforward observation with today's optical microscope, but they are also small enough to see their motion affected by molecular scale events. Specifically, thermal motion of colloidal particles is detectable on a wide range of time scales, and essentially reveals the inner molecular structure of the fluid.

1.1 Historical Introduction

These fundamental concepts are behind the motivations that drove scientists to elaborate techniques to measure the colloidal motion in the last century. In this section, I give a brief historical account of the very first measurements of Brownian motions tracking, which was made by Jean Perrin to confirm the molecular view of matter. I will also expose some technological challenges that were encountered in these first attempts to contrast with the current state of the art in microparticles tracking techniques presented in the next section. An interesting paper relating the history of Brownian motion and containing all the references to the classic original articles (not all referenced here) can be found in [3].

The molecular nature of matter is of no doubt today, but it was demonstrated irrefutably only a century ago by the experiments of Jean Perrin. After the initial discovery of the irregular motion of pollen grains suspended in water by Robert Brown (who originally presumed a living cause for the motion), the so-called Brownian motion appeared as the best candidate to experimentally check the discontinuity of matter hypothesis. Indeed between 1905 and 1908, parallel and complementary theoretical treatments made by Albert Einstein, Marian von Schmoluchowski and Paul Langevin were explaining the Brownian motion in terms of molecular impulses applied to the colloid by the surrounding matter.

Jean Perrin used the Brownian motion of granules to assess the molecular nature of the surrounding fluid, whereas the present work is intended to use the same thermal fluctuation of particles to measure "micromechanics" (hence a somewhat continuous property, at least on microns scale volume) and "microstructure" (hence an arrangement of matter components with microns length). However this study shares the underlying idea of relating some *averaged* measure of a Brownian *trajectory* to assess the structure of matter. Section 1.3 exposes the mathematical form of this statement.

In 1908, Victor Henri pioneered the use of a film camera, just invented a decade before, connected to a microscope. He attempted to perform Brownian motion measurements using this microcinematography technique that is truly the legitimate ancestor of video microscopy. For some reason that still remain unclear even now, Henri did not find quantitative agreement with Einstein's formula for the diffusion coefficient.

Perrin's experiments however justified the theory and were truly a technical *tour de force*. Confirmation of Einstein's theory required great precision in measurement of the size of the particles, control of their size distribution, high precision in measurement of the particle's displacements, and finally a high level of statistical accuracy. Jean Perrin had to develop numerous methods to attain maximum precision in all these aspects. To perform his tracking, Perrin and his student were plotting consecutive positions of individual granules on a grid at intervals of 30 seconds [4]. A total of about 500 displacements were gathered in each of his tedious experiments.

1.2 Micro Probes Tracking Techniques, Today's State of the Art

The use of video microscopy to track single micron-sized colloids and individual molecules has attracted great interest in recent years. Because of its numerous advantages and great flexibility, video microscopy has become the primary choice in many diverse tracking experiments encompassing numerous applications. In biophysical studies, it has been used to observe molecular level motion of kinesin on microtubules and of myosin on actin [5, 6], to investigate the infection pathway of viruses [7], and to study the mobility of proteins in cell membranes (see [8] for a review). Rheologists have tracked the thermal motion of Brownian particles to derive local rheological properties [9, 10] and to resolve microheterogeneities [11, 12] of complex fluids. The later class of application will be the subject of this study, and is introduced in detail in the next section 1.3 of this chapter. Colloidal scientists have pioneered the use of video microscopy in particle tracking experiments to study phase transitions [13] and to elucidate pair interaction potentials [14].

The standard setup for particle tracking video microscopy is presented in the next chapter. But briefly, it includes a CCD camera attached to a microscope that acquires images of fluorescent molecules or spherical particles. Typically hundred of particle can be tracked simultaneously, ensuring a high level of statistical accuracy. This setup gives access to a wide range of time scales,

from high speed video-rate to unbounded long time-lapse acquisitions, that are particularly suitable for studying biological phenomena. Subpixel spatial resolution is obtained by locating the particle at the extrapolated center of its diffraction image when it covers several pixels [15]. At usual magnifications of hundreds of nanometers per pixels, spatial resolutions of tens of nanometers is commonly achieved [16, 15]. These values are well below the optical resolution of about 250 nm [17].

Tracking particles with even higher precision has also been shown to be feasible with the use of more complex setups. Among the video-based techniques, low-light-level CCD detectors operated in photon-counting mode are used to increase signal [18, 19] in single molecule tracking. For such studies, background noise and signal levels (number of detected photons) are the limiting factors [20]. Improved observation techniques (such as internal reflection, near-field illumination, multiphoton or confocal microscopy) have been used to reduce the background fluorescence signal. Furthermore, elaborate extrapolation algorithms have been employed to refine particle positioning [15]. Under optimized conditions, spatial resolution as low as a few nanometers has been achieved [5]. However, in addition to their inherent complexity, these techniques are not well suited for studying large length scale dynamics, as they probe a reduced volume of sample [18].

Furthermore, subnanometer resolution can be achieved using laser interferometry [21] or laser deflection particle tracking [22, 23]. However these methods can not easily be extended to track several particles at the same time, unlike video microscopy.

1.3 Quantitative Studies

In this section we explain how quantitative studies can be performed from the probes' trajectories extracted by the techniques exposed above. Essentially, the amplitude of the particles motion depends on the mechanical properties of the surrounding environment. This property is often assess in terms of rheometric measurements. Thus we start this section by putting particle tracking *micro*rheology in perspective with classical rheology, to encompass several advantages of the micron scale approach.

1.3.1 From Rheology to Microrheology

Rheology is the study of the deformation and flow of a material in response to an applied stress. Simple solids store energy and provide an elastic response, whereas simple liquids dissipate energy through viscous flow. For more complex viscoelastic materials, rheological measurements reveal both the solid- and fluid-like responses which generally depend on the time scale at which the sample is excited [24]. Traditionally, rheological measurements are performed on several milliliters of material in a mechanical rheometer (e.g. a cone-and-plate geometry rheometer) by applying a small amplitude oscillatory shear strain $\gamma(t) = \gamma_0 \sin(\omega t)$ and measuring the resultant shear stress $\sigma(t)$. In the viscoelastic linear regime (or regime of small amplitude straining, typically $\gamma_0 \ll 1$), the shear stress is proportional to the amplitude of the applied strain γ_0 and is itself sinusoidally varying in time. It can be represented as:

$$\sigma(t) = \gamma_0 \big[G'(\omega) \sin(\omega t) + G''(\omega) \cos(\omega t) \big] \ . \tag{1.1}$$

In the above equation, the term proportional to $G'(\omega)$ is in phase with the strain, while the term containing $G''(\omega)$ is in phase with the rate of strain $\dot{\gamma}(t) = \mathrm{d}\gamma/\mathrm{d}t$. $G'(\omega)$ is called the storage

modulus and represents storage of elastic energy, and $G''(\omega)$ is called the loss modulus and represents the viscous dissipation of that energy. The complex shear modulus $G^*(\omega)$ is defined by $G^*(\omega) = G'(\omega) + iG''(\omega)$ [24, 25]. Rheology measurements such as these have given valuable insight into structural rearrangements and mechanical response of a wide range of materials. They are particularly valuable in characterizing soft materials or complex fluids. However, conventional mechanical techniques are not always well-suited for all systems. Typically, milliliter sample volumes are required, precluding the study of rare or precious materials, including many biological samples. Moreover, conventional rheometers provide a measurement of the averaged bulk response, and do not allow for local measurements in inhomogeneous systems.

To address this issues, a new class of measurement techniques has emerged. These have come to be called *microrheology* methods, and probe the material response on micrometer length scales, using microliter sample volumes [22, 26]. Among the methods currently available to perform such measurements, we focus here on the most popular one: particle tracking microrheology. This methods typically use embedded micron-sized mechanical probes to locally deform the medium, and information is extracted from their motion. Techniques using small particles tracking fall into two classes: those involving *active* manipulation of probe particles within the sample, and those employing *passive* observation of thermal fluctuations of such probe particles. In either case, the probes used are typically spherical beads of between a fraction of micrometer to several micrometers in diameter and measurements are made from their trajectories. Before tackling the quantitative studies that are made in particle tracking microrheology, we outline below the specific advantages and features of such measurements [27, 28, 26], based on considerations about the length scale, time scale and energy/force scale at which they operate:

- Probing at micrometer length scales allows the characterization of local viscoelasticity. This is particularly important in heterogeneous systems where viscoelasticity varies from location to location in the sample [29]. Also, changing the size of the probes permits the characterization of the hierarchical structures often encountered in complex fluids at various length scales of observation [30].

- The required amount of sample is significantly reduced. This causes a reduction in cost and an increase in flexibility, as pointed out in the next point.

- Patricle tracking microrheology measurements are usually rapid, enabling for example detailed phase diagrams to be quickly established [31]. Equally, chemistry and other conditions (temperature,...) are quickly equilibrated in the small sample volume, and specific designs allows the monitoring of transient rheological changes in the sample [32].

- Since the probe has low inertia it is possible to perform high frequency measurements of the material response. This requires however adapted detection techniques, such as laser tracking discussed in the previous section.

- In passive measurements relying only on the probe thermal motion, the excitation energy is on the order of $k_{\mathrm{B}}T$, inducing forces of typically a few piconewton. This allows the study of soft fragile structure such as intracellular cells properties without disrupting their components. Moreover, it is possible to be certain that measurements are in the linear rheological regime (see next point).

- Many microrheology measurements have been reported to show good agreements with bulk rheology values. Many questions remain opened on how the sample chemistry and heterogeneity relate to this agreement [9, 22, 33]. But in general, a required condition is that the relative size of the probes must be bigger to any structural length scale (e.g. mesh size) of the complex material in order to treat the medium as a continuum around the embedded probe (see the following discussion).

In the next section, we derive the relation between probes trajectory and material property, by using a continuum theory. Indeed, when the embedded particles are much larger than any structural size of the material, particle motions measure the macroscopic stress relaxation. Smaller particles measure the local mechanical response and also probe the effect of steric hindrances caused by the microstructure (see Figure 1.1).

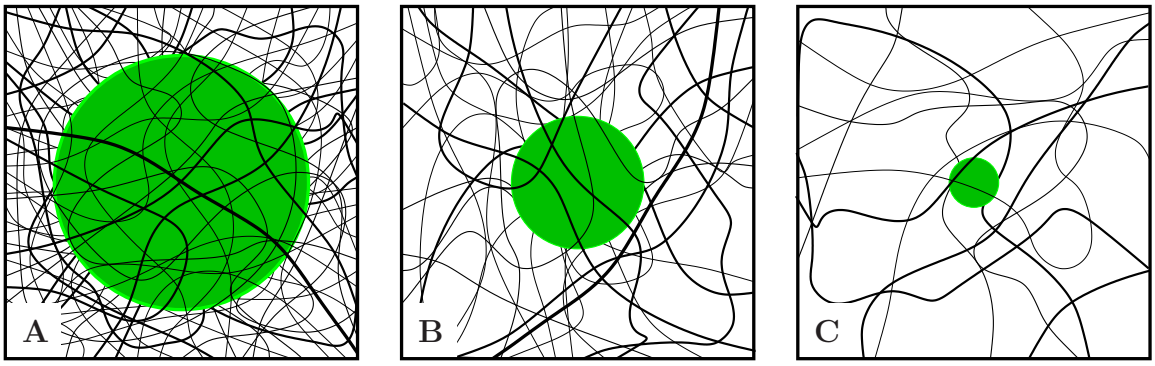

Fig. 1.1: Schematic of a probe particle of radius a embedded in a network of mesh size ξ. In A) $2a \gg \xi$, the probe is measuring bulk response; B) $2a \approx \xi$, the probe motion is highly coupled with the gel fluctuations; C) $2a \ll \xi$, the probe is exploring individual pore structure.

1.3.2 Quantitative Passive Microrheology

This research focuses on a particular passive particle tracking microrheology technique which is described in detail in chapter 2. The passive measurements use only the thermal energy $k_{\mathrm{B}}T$ to deform the medium, allowing the study of very fragile structures, but consequently, the material must be sufficiently soft to allow detectable motion of particles [34, 35]. Also, the intrinsic stochastic nature of thermal energy requires the measurement to collect a large amount of data in order to build a consistent statistic. The dynamics of particle motions are then revealed in the time dependent position correlation function of individual tracer particles [9], through either the power spectral density $S^*_{\mathbf{x}} = \langle |\mathbf{x}^*|(\omega) \rangle$, but more commonly through the mean-squared displacement, that is defined as:

$$\langle \Delta \mathbf{x}^2(\tau) \rangle = \left\langle \left[\mathbf{x}(t+\tau) - \mathbf{x}(t) \right]^2 \right\rangle , \tag{1.2}$$

Here $\mathbf{x}(t)$ is the d-dimensional particle position at time t, $\mathbf{x}^*(\omega)$ is its Fourier transform at the frequency ω, τ is called the lag time and the brackets $\langle \dots \rangle$ indicate an ensemble/time average. Such definitions are made possible thanks to some physically meaningful assumption on the process $\mathbf{x}(t)$, the main one being stationarity which can be justified by the thermal equilibrium assumption. When the bead evolves in a continuum, the generalized Stokes-Einstein relation relates the mean-squared displacement to the complex shear modulus [9, 36, 37]. In the Laplace[1] frequency space, it is written:

$$\tilde{G}(s) = \frac{s}{6\pi a}\left[\frac{2dk_{\mathrm{B}}T}{s^2\langle\Delta\tilde{\mathbf{x}}^2(s)\rangle} - ms\right] \tag{1.3}$$

where m and a are the spherical particle's mass and radius, k_{B} is the Boltzmann's constant and T the absolute temperature. In the next section, we will recall some limitations of applying this equation to colloidal dynamics. Within a valid frequency range, the inertial effect of the probe particle, ms in the above equation, can be neglected, and we obtain:

$$G^*(\omega) = \tilde{G}(i\omega) = \frac{dk_{\mathrm{B}}T}{3\pi a(i\omega)\langle\Delta\tilde{\mathbf{x}}^2(i\omega)\rangle} \ . \tag{1.4}$$

This equation represents a generalization of the Stokes-Einstein equation in the Fourier domain consistent with the convention of standard rheology. For example, we can easily get the behavior of $\langle\Delta\mathbf{x}^2(\tau)\rangle$ in a pure Voigt viscoelastic fluid model, for which $G^*(\omega) = G + i\omega\eta$. We find

$$\langle\Delta\mathbf{x}^2(\tau)\rangle = \frac{dk_{\mathrm{B}}T}{3\pi aG}\left(1 - e^{-G\tau/\eta}\right) \ , \tag{1.5}$$

from which we can restore the diffusive linear scaling $\langle\Delta\mathbf{x}^2(\tau)\rangle = 2dD\tau$ in a viscous liquid by setting $G = 0$. We introduced here the diffusion coefficient D through the famous Stokes-Einstein relation:

$$D = \frac{k_{\mathrm{B}}T}{6\pi a\eta} \ . \tag{1.6}$$

Unlike in simple fluids, the residual mean-squared displacement of the tracers in a complex material may scale differently with τ, and we can write $\langle\Delta\mathbf{x}^2(\tau)\rangle \sim \tau^{\alpha(\tau)}$. The coefficient α is called the *diffusive exponent*. The particles may exhibit subdiffusive motion ($0 < \alpha < 1$) or become locally constrained ($\alpha = 0$, see for example the elastic limit $\tau \gg \eta/G$ in relation (1.5)). It is important to note that, as an expression of the second law of thermodynamics, it is expected to have $\alpha \leq 1$ for all passive measurements in any material at equilibrium, independently of any time or length scale involved. In particular, this remark is valid even if the continuum assumption does not hold when the particle is too small. However, in that case, we understand that the probe is for instance likely to explore different microenvironment over the course of its trajectory (see Figure 1.1). This effect constitutes on obvious example in which the generalized Stokes-Einstein relation (1.3) can not be valid. We discuss the limits of the quantitative microrheology in the next section.

Beside the assumption of the continuum, which gives constraints on length scales, recent the-

[1] The Laplace Transform is defined as:

$$\mathcal{L}_t\big[g(t)\big] = \tilde{g}(s) \equiv \int_0^{+\infty} g(t)e^{-st}\mathrm{d}t \ .$$

oretical work has shown that the generalized Stokes-Einstein relation (1.3) holds only within a certain frequency range $\omega_B < \omega < \omega^*$ [38]. The lower limit gives the decay time ω_B^{-1} of the medium compression mode at the length scale of the bead, and the upper limit ω^* exists due to the onset of inertial effects of the material at the length scale of the bead. For typical soft materials and micron-size beads, there is a wide frequency range $1\,\mathrm{Hz} < \omega < 1\,\mathrm{MHz}$ where the generalized Stokes-Einstein relation is valid [34, 38, 39].

1.4 Motivations and Objectives

From the first colloidal particle tedious tracking experiments performed by Jean Perrin, to the actual performances of modern particles tracking techniques, gains in precision, temporal resolution and statistical accuracy have been colossal. Also the range of application has been much broaden, and the simple study of diffusion in purely homogeneous viscous fluid has given place to assessment in depth of more complex heterogeneous systems such as biological material. The importance of probing these system at the mesoscopic length scale is indisputable today, and video multiple particle tracking is one natural choice through its flexibility and availability. However, even though video microscopy particle tracking has seen a justified growing popularity in recent years, few characterization of the standard setup have been made. More strikingly, some fundamental limitations have not been pointed out. This work is intended to expose and understand some critical characteristics of the technique, but also to propose new methods and analysis scheme to take full benefit of the great quantity of information accessible with this type of measurement.

The advantages of this technique are illustrated in the assessment of an important class of biomaterials called self-assembling peptides. These systems have a considerable potential for a number of applications, including scaffolding for tissue repair and tissue engineering, drug delivery of molecular medicine, as well as biological surface engineering. One attracting characteristic of self-assembling peptides is that they undergo a solution/gel transition with time and/or by varying their chemical composition (pH, salt concentration,...). The experimental characterization of this transition is extremely challenging with conventional methods due to the high sensitivity and the fragility of the system. The microrheology technique exposed here is well-suited to study a give new physical insights in the self-assembly process.

The main objectives of this work are summarized below.

- Study of the limitations of video multiple particle tracking
- Optimize the technique and elaborate possible correction methods for these limitations
- Develop new analysis approach to fully exploit measurements output
- Assess the sol-gel transition of self-assembling peptides

1.5 Overview

This thesis is organized as follow. In chapter 2, we expose in detail the experimental technique of multiple particle tracking that is used and studied throughout the rest of the text. In particular, we end this chapter by pointing out two important characteristics and limitations of this technique, namely the spatial resolution (that will be studied in the following two chapter), and the statistical design of the measurements (that will be covered by a subsequent chapter).

Chapter 3 describes the localization errors arising when performing colloidal particle tracking. A general model for the errors is developed by separating their origin into two sources: the detector noise induces “static error” and the acquisition time leads to “dynamic error” in a particle tracking experiment. This model is experimentally verified for video microscopy particle tracking.

Chapter 4 is mainly theoretical and exposes the influence of the dynamic errors on the measured mean-squared displacement of probes moving in various model fluids. We show in particular that important misinterpretation can arise in microrheological measurement where the elastic modulus is calculated.

Chapter 5 presents an important study of the statistical design of the measurement output from video microscopy particle tracking. Since the particles in the sample can be detected only when they are traveling in a finite imaging volume, the extracted trajectories, and thus quantitative assessments that are made from these trajectories, have peculiar statistical properties that depend on the volume of observation. We present in this chapter a detailed mathematical route to account and characterize this effect.

At this point we can note that the localization errors exposed in chapter 3 and 4 occur in general at high frequencies of the measurements, whereas the statistical uncertainty presented in chapter 5 are mainly affecting low frequencies accuracy. Thus, in these 3 chpaters, we provide a characterization of the technique over the entire spectrum of measurements.

Finally, after having gained a full characterization of the technique and developed tools to correct some limitation and to extract new information, we applied multiple particle tracking to study a complex time-evolving system called self-assembling peptides, that forms a hydrogel biomaterial through a solution/gel transition. In particular, we present in chapter 6 the analysis of the kinetics of gelation of this system.

CHAPTER 2

Experimental Methods for Multiple Particle Tracking

This chapter explains in thorough detail the experimental technique that is used and studied in this project. Multiple particle tracking technique is performed by combining video microscopy and image processing to obtain time-resolved and simultaneous measurement of individual colloidal particles' trajectories. This chapter has been purposely written as a concise manual on the technique, from sample preparation to basic data analysis. But it is also intended to point out important characteristics and limitations, namely spatial resolution and statistical design of the measurements, that will be studied in depth in subsequent chapters.

Thus we first expose the experimental protocol that is consistently followed to prepare the probed material sample throughout the rest of the work presented in this manuscript, and we explain the details of the fluorescent microscopy movie acquisition. Next we briefly expose the main concepts of the image processing algorithm developed by Crocker and Grier [16] to extract colloidal trajectories from movies of the particles' motion. Finally in the last two sections we identify two significant limitations: the spatial resolution of the tracking and the statistical peculiar design of the output data.

2.1 Experimental Protocol

2.1.1 Sample Preparation

Fluorescent particles

The choice of the particles that will serve as probes is critical and must be made carefully. In this study, only fluorescent particles have been used to perform multiple particle tracking measurements. It is possible to track un-died particle in a bright field montage [28]. However, the diffraction figure of a submicron spherical particle obtained in bright field is peculiar: it is a roughly uniform black spot on a white background when the particle is on one side of the focal plane of the microscope objective, but becomes a black ring with a white halo when the probes travels to the other side of the focal plane. This introduces several limitations to the tracking algorithms when the movies are processed (see the following sections) and we limited our choice to fluorescence. Fluorescent microspheres are commercially available from several vendors: Polysciences (Warrington, PA), Invitrogen's Molecular Probes (Eugene, OR) or Bangs Laboratories (Fishers, IN) for example. The fluorescent microspheres are usually made of polystyrene at a density of $1.05\,\mathrm{g.mL^{-1}}$ that can be eventually matched by addition of heavy water D_2O in the suspension if the system's chemistry allows. These microspheres are proposed with a wide variety of dyes, sizes, and surface chemistry.

Common dyes include Yellow-Green fluorescence that is maximally excited at 441 nm and emits at a maximum wavelength of 486 nm (matches fluorescein filter sets), or Yellow-Orange that has fluorescence spectra at 529/546 nm excitation/emission maxima (matches rhodamine filters). Photobleaching of the dye embedded in the microspheres can be detected for the small trackable beads (about 100 nm, see later in this section), and it is preferable to deoxygenate the particles suspension by bubbling argon through the sample before injecting it into the observation chamber (see next section).

The sizes offered typically range from 0.02 to $10\,\mu$m, with usually coefficient of variation (CV) ranging from 20% for the smallest size to less than 5% for particles bigger than $0.2\,\mu$m (for certain vendors, the coefficient of variation increases to 10% for particles bigger than $6\,\mu$m). In microrheology and microstructure characterization, the size of the probe particle is the length scale at which the material is probed. Thus a high level of monodispersity (CV less than 5%) is essential. The range of actually used particle size is also limited by other factors related to the technique. On the lower size end, the fluorescent particles must emit sufficient photons and their diffraction image must be sufficiently wide so that they form on screen a measurable brightness two-dimensional profile. This limit of detection will be covered more in details in subsequent sections, but to fix the idea, for the industrial grade charge-coupled device camera used in our setup with higher magnification, we find that the minimum trackable particle size is about 100 nm. On the other end of the size range, the detection of small displacement is limited by the spatial resolution of the tracking technique (thoroughly characterized in the next chapter). As explained in chapter 1, the dynamics of Brownian probes, and hence the typical displacement amplitude, depend on their radius, on the time scale of observation and on the mechanical nature of the probed material (see the generalized Stokes-Einstein relation 1.3 derived in chapter 1). Hence, bigger probes will exhibit slower dynamics and for a given time scale of observation, will undergo smaller displacements. As a rule of thumb, we can use $k_\mathrm{B}T/(3\pi aG) \geq \varepsilon^2$ to find the maximum particle radius a trackable in a medium with elastic modulus G at a given time scale of observation. Here ε is the typical spatial resolution of

the tracking where k_B is the Boltzmann's constant and T is the absolute temperature. We get:

$$a_{max} \leq \frac{k_B T}{3\pi\varepsilon^2 G} \tag{2.1}$$

which typically gives $a_{max} = 0.3\,\mu$m at $T = 25°C$ for $G = 1\,$Pa and $\varepsilon = 10\,$nm. To this subtile trade-off between several imbricated experimental parameters, we must also recall at this point that the generalized Stokes-Einstein relation derived in the previous chapter (and used above to derive the rule of thumb Eq. 2.1) is valid only if the particle is moving in a continuum. This means that any structural changes in the material must occur at length scale much smaller than the probes diameter (see figure 1.1). Whether or not this relation can be applied depends on the size of the probes, which in turn must be chosen accordingly. Consequently, the physical interpretation of the results must be made carefully. Hence, these are general considerations of high importance when choosing the probes particle size for material property measurements using particle tracking.

The surface chemistry of the probes is an equally important experimental parameter, and it has been the subject of several studies in the very recent years [40, 41, 42]. Polystyrene plain particles are naturally uncharged and hydrophobic, but all vendors commercialize modified particles with a variety of surface functionalization. Most common functions includes carboxylate modification for which the particle surface is decorated with carboxyl groups COOH, resulting in hydrophilic and negatively charged probes at pH greater than about 4 (and uncharged below). Solution of such beads are very stable and often used for microrheology experiments. Amine-modified probes are hydrophilic particles with positively charged amine groups NH_2 relatively stable for pH below 9 at which the surface charge is not neutralized. The choice of probes surface chemistry depends on the material under study, but usually chemically inert particles with the least possible influence on the material properties are sought. It is also possible to use other functionalization such as a coating of the probes with Bovine Serum Albumin (BSA) protein, or decorate the particle with a layer of short polyethylen glycol (PEG) for steric hindrance [40, 41, 43].

Ideally, the particle should be uniformly dispersed in the material to be probed. Depending on the interactions between the materials and the probes, but also the interparticle interactions, beads can form aggregates. It is usually possible to distinguish aggregates of two or more beads from isolated particles and to discard them from the tracking. But for small particles, this becomes challenging and the monodispersity requirement can be violated. For all experiments, beads bulk solutions and, when possible, their suspension in the material of interest, will be thoroughly sonicated. We will be careful however to not overheat the solutions. Also, the concentration C_b of beads in the sample should be small enough to not alter significantly the property of the sample. In general, only a low volume fraction $\phi < 0.1\%$ of beads are dispersed in the sample.

Chamber of Observation

The sample is injected into a custom made chamber for observation with the video microscopy setup described in the next section. The chamber must be a perfectly sealed closed volume, as any leak induces a drain and/or evaporation that can produce unwanted convection motions of the particles. Also, when injecting the sample into the chamber, air bubbles needs to be avoided for similar reasons. To make the chambers of observation, we put two 1 cm-wide stripes of parafilm on a microscope slide (typically $24 \times 60\,$mm, No. $1\frac{1}{2}$ thickness - that is 0.16 to 0.19 mm thick), parallel and apart from each other by approximately 5 mm. A square coverslip ($18 \times 18\,$mm, No.

1 thickness or 0.13 to 0.17 mm) is then deposit to bridge both parafilm stripes, as described in the figure 2.1. The parafilm is briefly melted while moderate pressure is applied on the top coverslip for efficient sealing. We then obtain a channel open at both end, that is 5 mm wide and approximately 150 μm high.

The slides are preconditioned the following way for cleaning: we thoroughly wipe the slides with a detergent solution (Micro-90) to remove the oil used for their packaging; the slides are rinse with water and then put in a bath of NaOH (1 M) for at least 20 mn; after another rinsing with water, the slides are hold in boiling water for 5 to 10 mn. They are finally dried under argon. This cleaning protocol tends to turn the slides hydrophilic which facilitates the filling of the chamber by capillary forces without the formation of bubbles. Both end of the cell are sealed using vacuum grease shortly after injection of the sample in order to prevent drying and convective flow. We found that these chambers remain hermetically sealed for at least five days.

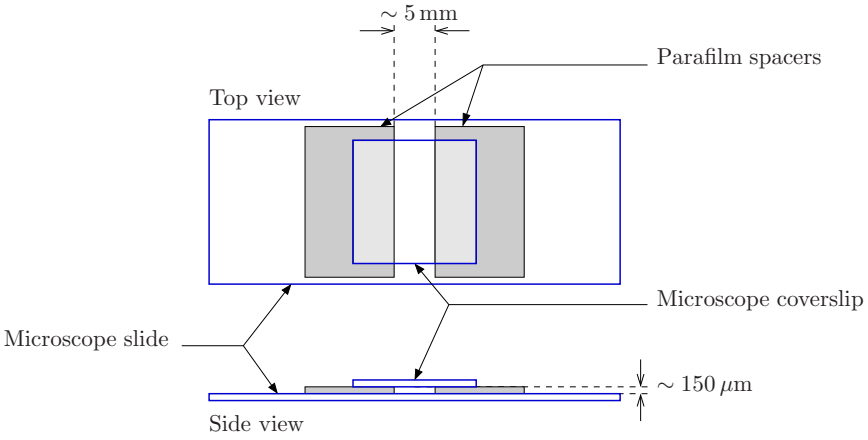

Fig. 2.1: Custom made microscope observation chamber for multiple particle tracking experiments. A standard glass microscope slide holds the chamber made by adding a cover slip separated by two parafilm spacers. The resulting chamber is approximately 5 mm wide and 150 μm high.

There are other techniques to build observation chambers, and some more sophisticated design have been developed using dialysis membrane to easily change the chemical composition of the material [32]. Also, Ibidi (Integrated BioDiagnostics GmbH, München, Germany) recently started commercializing plastic micro-slides for cell observation, that contains chambers which dimensions are similar to what is made here.

2.1.2 The Video Microscopy Setup

The fluorescent video microscopy setup in our laboratory consists of an inverted microscope (Zeiss Axiovert 200, Jena, Germany), to which an excitation Hg-lamp light source is attached to illuminate

the observed sample through the objective. The light beam passes through an excitation filter that transmits only a certain range of wavelengths. Within this range, the illumination is then almost entirely reflected by a dichroic filter towards the sample, through the objective, to excite the fluorescent probes. The latter emits a signal that returns through the objective to the dichroic filter, the latter being designed as nearly transparent at the emission wavelength. A final emission filter is placed on the optical train before the visualization ports of the microscope to block any stray transmitted excitation light. In almost all experiments, we used yellow-green fluorescent particles with a filter set (excitation, dichroic and emission) that matches fluorescein fluorescent spectrum (Omega Optical, Brattleboro, VT).

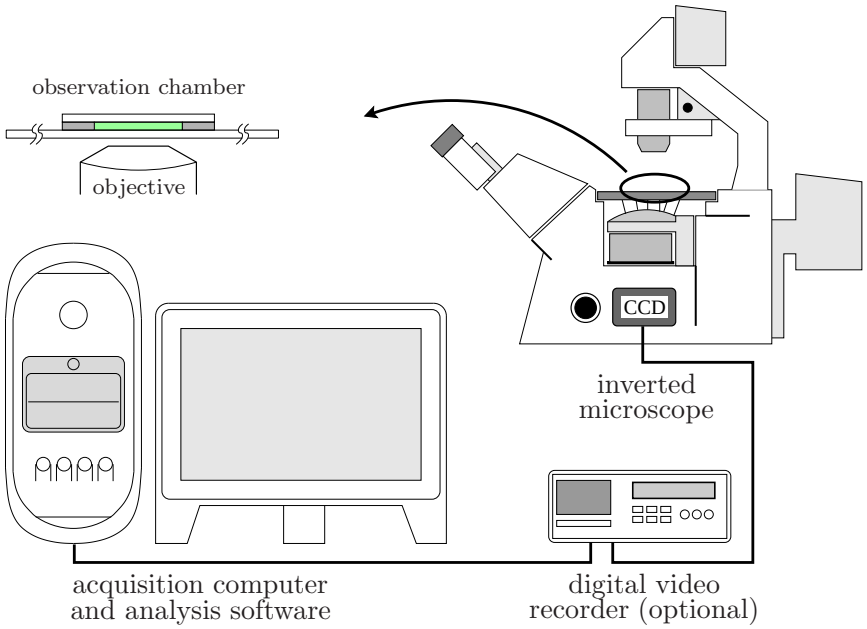

Fig. 2.2: Schematic of the video microscopy setup for multiple particle tracking. The sample is observed through a fluorescent inverted microscope equipped with a CCD camera. The camera is connected to a digital video recorder and movies are acquired and analyzed by a computer supplied with a frame grabber.

An industrial grade charge-coupled device (CCD) camera (Hitachi KP-M1A, Woodbury, NY) with variable electronic shutter speed ranging from 1/60 s to 1/10000 s, set to frame integration mode is attached to the side port of the microscope. The analog output of the camera is connected to a frame grabber PCI board (Scion LG-3, Frederick, MD) that digitized the video signal and is ran by a Power PC G4 computer (Apple Computer, Cupertino, CA). The analog-to-digital electronic chain provides an 8-bit dynamic range (that is a range from 0 to 255 analog-to-digital units or "ADU") output that is visualized and recorded using the software NIH Image at a maximum video rate of 30 fps. Image of 640×480 pixels are successively captures for a movie length ranging typically

from 1000 to 5000 frames, the latter duration being limited by the software's allowed memory. The movies are saved as an uncompressed three-dimensional tiff stack of images. These type of file are directly readable by the image processing software Interactive Data Language (Research Systems, Boulder, CO). An optional step consisting in recording the movies on tape is possible before digitization. However in general we avoided this step because the DV recording format used in our laboratory is a compressed numerical format that introduces a loss of information. The figure 2.2 gives an overview of the video microscopy setup.

We used several microscope objectives in the experiments. The most relevant parameters involved in multiple particle tracking experiments are given in table 2.1 for every objectives we used. Another important parameter not appearing on this table is the depth of tracking, that is the spatial interval in the direction perpendicular to the field of view and within which the particles are actually trackable. In most common multiple tracking experiments, measured trajectories are the two dimensional projection in the (x, y) field of view plane of the three dimensional probes motion. Tracking in the third dimension z can be performed using the z-dependent diffraction figure [44], but requires a new toolset of algorithms that have not been used here. Moreover, such three dimensional tracking is in general more constraining in terms of the experimental parameters. The resulting volume of observation in the sample is defined by the field of view in the (x, y) directions, and the depth of tracking in the z direction. The latter dimension depends on the depth of field of the objective, but also on the parameters used in the tracking algorithms. We will study this important quantity in details in subsequent sections of this chapter. The volume of observation is always chosen at least $50\,\mu$m away from the wall within the chamber of observation to minimize the unwanted effect of particle-wall hydrodynamics interactions on the probes motion.

The image processing step described in the next section uses brightness variations information from the movie to extract particle trajectories. A typically good, trackable image, should consist of white spots on a black background. The acquisition signal should cover the maximum dynamical range of the camera (darkest background and brightest particle's spot) without saturating the signal. In particular, the microscope aperture diaphragm can be adjusted or neutral density filter can be used to avoid camera signal saturation. Better, the camera electronic shutter can be shorten to reduce dynamic error in case of too bright signals.

Finally, it is important to point out a characteristic feature of the standard video signal. The horizontal scan for the video acquisition is such that a single frame is actually made of two interlaced fields, each of them containing either all the odd or all the even rows (hereafter defined as the x, or horizontal, direction) of the CCD matrix. These two fields are exposed $1/60\,$s apart, such that an object moving in the direction of the CCD rows will be captured at two different positions in each field. This has important implications in terms of the dynamic errors presented in the following two chapters, and the usual procedure is to de-interlace the tracking by analyzing each field individually. A temporal resolution of $60\,$Hz is thus achieved, but at the cost of a loss in the spatial resolution of the particle localization on each field. Indeed, each particle image contains only half the number of pixel after de-interlacing, which degrades the brightness weighted centroid estimation used in the algorithm (see next section). This effect is particularly significant in the direction perpendicular to the interlacing (that is the y direction, or vertical direction) for which the image is shrunk by a factor 2. Very often in the following studies we analyzed particle motion only in the horizontal direction.

Objectives	N.A.	Magnification	Field of View	Depth of Field
20× air	0.5	$0.642\,\mu$m.pxl^{-1}	$411 \times 308\,\mu$m	$15.3\,\mu$m
40× air	0.75	$0.329\,\mu$m.pxl^{-1}	$211 \times 158\,\mu$m	$5.2\,\mu$m
63× water im.	1.2	$0.210\,\mu$m.pxl^{-1}	$143 \times 101\,\mu$m	$2.1\,\mu$m
100× oil im.	1.4	$0.132\,\mu$m.pxl^{-1}	$84 \times 63\,\mu$m	$1.2\,\mu$m

Table 2.1: The different objectives and the corresponding parameters relevant in multiple particle tracking experiments. The magnifications are specific of the setup found in our lab, and depends in general on the microscope optics and CCD chip pixel size of the camera. The field of view is calculated based on 640×480 pixels frame size. The depth of field is calculated using an equation provided by the lens manufacturer (Zeiss): DOF(μm) $= 10^3/(7 \times \text{M} \times \text{N.A.}) + 0.5/(2 \times \text{N.A.}^2)$, with M the objective magnification (20 for the 20×, 40 for the 40×,...).

2.2 The Tracking Algorithms

The next step in the multiple particle tracking technique is to extract a list of probe trajectories from the movie of particle motions acquired with the video microscope. The image processing algorithms we used in this study were originally developed by Crocker and Grier [16]. The generic algorithms were written in IDL language (Research Systems, Boulder, CO) which handles efficiently manipulation of large arrays as a dedicated image processing language. Indeed, raw uncompressed movies from video microscopy measurements ends up being relatively big files. For example, a full camera field 640×480 pxl movie of 1000 frames, at 8-bit grayscale resolution (256 levels, from black to white), holds for 293MB of hard drive space. Also, the software routines have been made available online at http://www.physics.emory.edu/∼weeks/idl/ (they have been recently translated into a MatLab version), a website maintained by Eric Weeks. We recall briefly in this section the image processing principles underlying the tracking. Specifically, there are 3 steps to transform a movie into a list of probe trajectories: removing unwanted noise and background signal in each frame (image restoration), locating the particle images in each frames pixel array (feature location), and finally connecting successive positions into trajectories (labeling positions). A detailed description can be found in the original paper [16] and we will recall in this section only the main concepts of the algorithms.

2.2.1 Images Filtering

The filtering step of the raw image is made thanks to a linear band-pass spatial filter. The typical images obtain in colloidal video microscopy are composed of white circular spots distributed on a black background. The video images are affected by a noise from a variety of origins, discussed in detail in the appendix. Subtracting off the background is made by building a background image resulting from the convolution of the original image with a constant kernel of size $2w_1 + 1$, where w_1 is a larger than the typical radius in pixels of a single particle brightness profile on the array,

but smaller than the typical interparticle distance (w_1 is typically a particle image diameter). If the original array is described by $A_{i,j}$ the brightness value for the pixel indexed by (i, j) on the CCD matrix (say i is in the subscript in the x direction and j in the y direction), we obtain the background image by using the convolution:

$$B_{i,j} = (2w_1 + 1)^{-2} \sum_{|m|\leq w_1} \sum_{|n|\leq w_1} A_{i+m,j+m} \tag{2.2}$$

which corresponds to keeping the long spatial wavelength (low-pass filter in the spatial frequency space with a cutoff at $(2w_1 + 1)^{-1}$). Another random noise with small correlation length of about 1 pxl comes from digitization and camera noise, and is filtered by smoothing the original image with a narrow Gaussian kernel, with again a support square mask of size $2w_1 + 1 \gg 1$. The resulting Gaussian smoothed image is calculated by:

$$G_{i,j} = \left[\sum_{|m|\leq w_1} e^{-m^2/4}\right]^{-2} \sum_{|m|\leq w_1} \sum_{|n|\leq w_1} A_{i+m,j+m} \times e^{-(m^2+n^2)/4} \tag{2.3}$$

which is again a low-pass filter in the spatial frequency domain, the cutoff being this time $1\,\mathrm{pxl}^{-1}$. The difference between the noise-reduced image G and the background image B is an estimate of the ideal image $\widehat{A}$:

$$\widehat{A} = G - B = A * K \tag{2.4}$$

where the convolution kernel is given by:

$$K_{m,n} = \left[\sum_{|m|\leq w_1} e^{-m^2/4}\right]^{-2} \times e^{-(m^2+n^2)/4} - (2w_1 + 1)^{-2} \quad \text{for } |m|, |n| \leq w_1 \tag{2.5}$$

and $K_{m,n} = 0$ otherwise. The image resulting from this difference is a low intensity background with sharp circular spot corresponding to the original particle images. The choice of a support of size w_1 for the Gaussian filtering allows the calculation of a single convolution step of the image with the kernel K. The result is also usually a higher precision data arrays, if the original 8-bit image has been accordingly converted.

2.2.2 Locating Features

Candidate features are located at the pixel exhibiting the local brightest signal within a distance w_2. These local brightness maxima are identified using a non-linear morphological operation called gray-scale dilatation, with a disk of radius w_2 as the structural element. This operation sets the value of an image pixel, say $A_{i,j}$ to the maximum brightness value within a distance w_2 of the pixel coordinate (i, j). A pixel in the original image with same value as in the dilatation-transformed image is then a candidate feature location. This locally brightest pixel, say at coordinates (i, j), is presumably near the particle image true center. Resolution in locating this center can be gained by using the corresponding local brightness profile. A brightness-weighted centroid is calculated in a circular region centered in (i, j) and of radius w_2 such that

$$x = i + \mu_0^{-1} \sum_{m^2+n^2\leq w_2} m \times A_{i+m,j+n} \quad \text{and} \quad y = j + \mu_0^{-1} \sum_{m^2+n^2\leq w_2} n \times A_{i+m,j+n} \tag{2.6}$$

are the corrected positions of the brightness center obtained at a subpixel resolution, where $\mu_0 = \sum_{m^2+n^2\leq w_2} A_{i+m,j+n}$ is the integrated brightness of the corresponding spot. The radius w_2 of the mask is usually chosen slightly larger than the particle image radius to include eventual tails of

the profile. For each image, this calculation is repeated for all local maxima found by the previous dilatation transform. Ideally, each of these pre-located particle candidates correspond to a given brightness profile. Moments of each brightness local distribution are also calculated to characterize its shape. For example:

$$\mu_2 = \sum_{m^2+n^2 \leq w_2} (m^2 + n^2) \times A_{i+m,j+n} \tag{2.7}$$

can be used to evaluate the characteristic squared size of the brightness spot. Also, the original algorithms include the calculation of the eccentricity e of the brightness spot (from 0 to a perfectly circular profile to 1 for an elongated profile in a given direction).

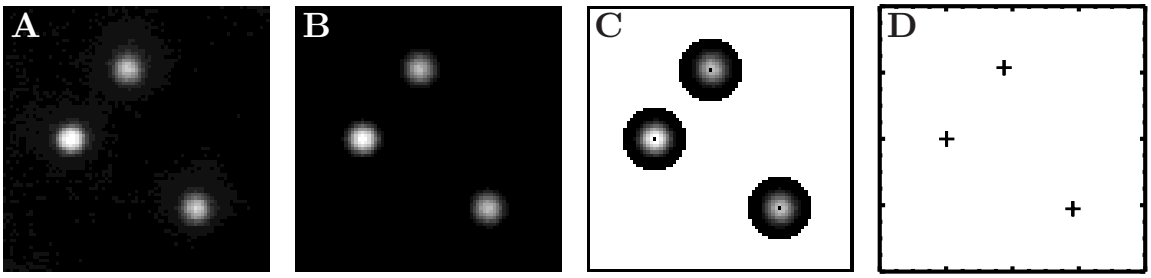

Fig. 2.3: Successive steps of feature location in the tracking algorithms. A) is a typical raw frame from a fluorescent colloidal video microscopy movie. B) is the result of the image restoration from the raw frame. C) illustrates how circular masks are centered on the local brightness maximum and used to clip the individual spot to calculate brightness integrated parameter, such as the center position of the intensity profile or its squared radius of gyration. D) shows the resulting subpixel resolution feature localizations

This feature location routine turns out to be very sensitive and will report many possible locations, including from false particle identification. The parameter space (μ_0, μ_2, e) is used to characterize the shape of the brightness profile of the found features. Reported in this characteristic space, true particles images will fall into a definite region whereas spurious identification (e.g. colloidal aggregates, noise and imperfections in the optical system) will lie outside this region. The measured cluster of point obtained in this space can be clipped to the specified region to remove false particle identification and to retain only valid data for the next step of the tracking. This clipping is particularly important in terms of spatial resolution and statistical characteristic of the output data. We allocated the next part of this chapter (section 2.3) to enter into greater details of this critical tracking step.

2.2.3 Building Trajectories

Once particles were located in every frame of the movie, found locations must be linked into trajectories. In other words, a given location in a given frame (i.e. at a given time) is assigned a

label and the same label must be assigned to the found position corresponding to the same detected particle in the next frame (that is, a priori among all candidate locations found in this frame). In practice, this is done by setting a cutoff w_3 in the maximum possible displacement between successive frame. Hence, the next position is found in a vicinity of a characteristic length scale w_3 around the current position. This is repeated for all located feature in all frame. The histogram of all displacements between successive frames is then plotted to check if w_3 is an appropriate cutoff on the distribution, namely to verify that w_3 does not clip a non-negligible number of event in the histogram. Naturally, the typical distance a particle moves between successive frames must be significantly smaller than the typical inter-particle separation in order to build valid trajectories. This is generally the case at the low volume fraction of probes used in the sample.

The resulting output of the tracking routines is a list of x and y positions, the time t and particle identities number. Typically, millions of positions are assigned to thousands of particle trajectories. As discussed earlier in the text, the particles are effectively detectable when they are traveling in a given volume of observation. This volume is defined by the video microscope field of view (an (x, y) plane of size x_b and y_b) and in the z direction by the depth of tracking z_b. This depth of tracking depends on the optics (depth of field of the objective). But it also depends on the pre-processing step of clipping the cluster of points in the parameter space (μ_0, μ_2, e) into a target valid region. We will explain this important parameter in the next section. For now, let us notice that particles can move in and out of the volume of trackable observation. When a particle moves out of sight and comes back, a new trajectory is started (a new label is assigned to the particle). A memory option in the tracking algorithm can be used to allow gap in trajectories when a feature is not found for a limited small number of frame. But in general, trajectories will have different duration. We will point out in the following sections how this observation is of high importance for studying heterogeneous systems.

2.3 False Data Removal

As explained in the previous section, the tracking algorithms developed by Crocker and Grier [16] locate images of particles on each frame (or field) of a movie. Each image is usually a bright (or white) spot on a black background. The algorithm places a mask on each spot over which signal (difference of the absolute brightness and the background level, obtained after filtering) is integrated to return the signal weighted location of the center of the particle image, but also the radius of gyration $\mu_2^{1/2}$, the signal total mass (integrated signal) μ_0 and the eccentricity e of the spot image (0 for a circle and approximately 1 for an elongated spot). After such measurements are performed on each frame, a post-processing of the raw data is applied to all found features by selecting a correct range for $(\mu_2^{1/2}, \mu_0, e)$ to avoid the detection of spurious particles (such as aggregates of particles). As the particle travels in the volume of observation $V_\mathrm{b} = x_\mathrm{b} y_\mathrm{b} z_\mathrm{b}$ and visit different altitudes z, the total mass and the radius of gyration of its image greatly vary (see figure 2.4) whereas the eccentricity has been found to remain essentially unchanged (data not shown in this section). This geometrical change is a consequence of diffraction, and has been used to perform three dimensional tracking [44, 16]. We perform here a precise characterization of the variations $\mu_0(z)$ and $\mu_2(z)^{1/2}$ that helps understanding how to perform the post-processing clipping in the $(\mu_2^{1/2}, \mu_0)$ space. We conclude by a determination of z_b.

In order to experimentally evaluate the variation of $\mu_0(z)$ and $\mu_2(z)^{1/2}$ as a function of z, we

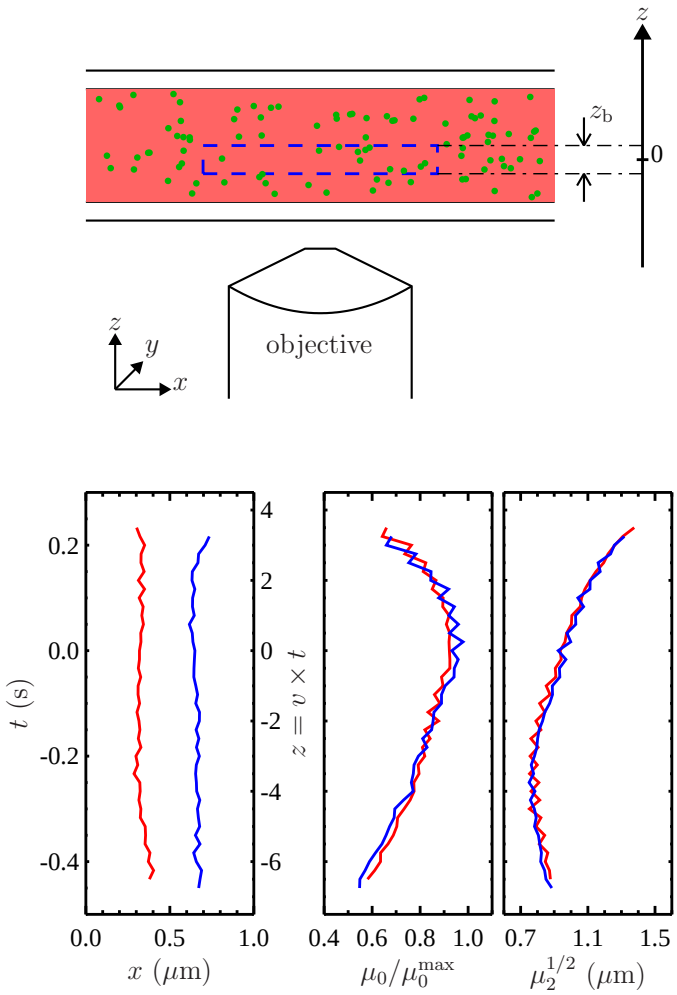

Fig. 2.4: Schematic for the experiments used to assess the variation of $\mu_0(z)$ and $\mu_2(z)^{1/2}$ with the altitude z. Probes are fixed in agarose and their tracking is performed while the objective is translated. A particle is tracked as long as it remains in the depth of filed of the moving objective. When seen at different altitudes in the volume of observation, the particle's brightness passes through a maximum, set to $z = 0$ for each particle in order to perform averages over several tracks. In the bottom plots we present examples of such variations for two particles (red and blue curves) for which we have matched the altitude of maximum brightness. The radius of gyration (right plot) shows also significant variations with z.

immobilized the probes in an agarose gel of concentration 1% w/v loaded in a microscope chamber for observation. The agarose (Seakem LE; BMA, Rockland, ME) was dissolved in boiling water, and

$0.925\,\mu$m diameter beads were added during the cooling, when the temperature reached 80°C. After a short vortexing, the chamber of observation was loaded with the warm solution. We verified that at this concentration of agarose, particles motions are well below the tracking limit of detection. Also, note that agarose has the same refractive index as water [45]. By attaching the microscope focusing knob to a motor, the 40× (see table 2.1) objective lens was translated in the z direction at a constant velocity $v_z = 15 \pm 0.5\,\mu\text{m.s}^{-1}$, while a movie of the focusing/defocusing of the dispersed particles was acquired. The tracking algorithms were applied on these movies at times when the volume of observation is between 30 and $70\,\mu$m above the bottom of the chamber. On this range, we visually checked the validity of the found features by overlaying the located particles with the original microscope images. Obvious false hits were manually removed when needed. For each trajectory, the signal integrated brightness $\mu_0(t = z/v_z)$ passes through a maximum value when plotted versus time. The altitude of maximum mass $\mu_0^{\max}$ (calculated from the time of maximum mass) is obtained when the corresponding particle crosses the plan of focus of the objective, and is set to 0 for all tracked particles as shown in figure 2.4. All curves $\mu_0(z)$, $\mu_2(z)^{1/2}$ and $e(z)$ then overlap to within 10% of the ensemble mean, even if the post processing visual selection was in general significantly less restrictive. We show in figure 2.5 the resulting averaged curve (red line) in the $(\mu_0, \mu_2^{1/2})$ parameter space, and the corresponding typical particle images obtained at various altitude z in the volume of observation (the mapping in the $(\mu_0, \mu_2^{1/2})$ space obtained from this particular particle is shown by the blue curve).

When clipping the cluster of points obtained in the $(\mu_0, \mu_2^{1/2})$ parameter space, it is preferable to provide a cutoff region such that the resulting tracking achieves highest resolution in the localization of the particles (see chapter 3). To determine the clipping region, we first set a value z_b of depth of tracking that is the width of an interval of altitude z out of which the found features are discarded. Namely, two altitudes z_1 and z_2 are chosen with $z_2 - z_1 = z_\text{b}$, and correspond to two points $(\mu_0, \mu_2^{1/2})_1$ and $(\mu_0, \mu_2^{1/2})_2$ in the clipping parameter space $(\mu_0, \mu_2^{1/2})$. Choosing particles for which $z \in [z_1, z_2]$ means discarding all features above the line connecting the points $(\mu_0, \mu_2^{1/2})_1$ and $(\mu_0, \mu_2^{1/2})_2$ (see figure 2.5). From the tracking performed with the remaining selected feature, we can calculate the resulting spatial resolution ε by evaluating the one-dimensional mean-squared displacement of the fixed particle, $\langle \Delta x^2 \rangle = 2\varepsilon^2$ (see chapter 3 for a full description of this method). For a given z_b, the set of points $(\mu_0, \mu_2^{1/2})_1$ and $(\mu_0, \mu_2^{1/2})_2$ such that the corresponding altitudes verify $z_2 - z_1 = z_\text{b}$ is not unique. Among the different possible resulting clipping lines, we choose the one that minimizes ε. For this experiment using $0.925\,\mu$m diameter beads observed through the 40× objective, this method to obtain the cutoff region has been applied to obtain clipping lines corresponding to the parameter $z_\text{b} = 6, 8, 10$ and $12\,\mu$m (see figure 2.5). We report in table 2.2 the corresponding minimum values of ε. In this table, this method to obtain z_b and ε is labeled (1) and the corresponding estimates are written $z_\text{b}^{(1)}$ and $\varepsilon^{(1)}$ respectively. Notably, we observe that the spatial resolution increases with an increasing depth of tracking.

To compare these results with a more typical experiment, we performed the tracking $0.925\,\mu$m diameter polystyrene beads dispersed in a 1 : 1 solution of H_2O/D_2O (polystyrene density matching) at a volume fraction $\phi = 2.6 \times 10^{-3}\%$. The tracking parameters were identical to those used in the agarose experiment described above. Specifically, we used the 40× objective and the volume of observation was $50\,\mu$m above the bottom of the chamber. The clipping region was chosen identical to what precedes in the agarose experiment for the different values of z_b investigated here. We repeated this experiments 20 times and combine the results into one tracking array. We plot on

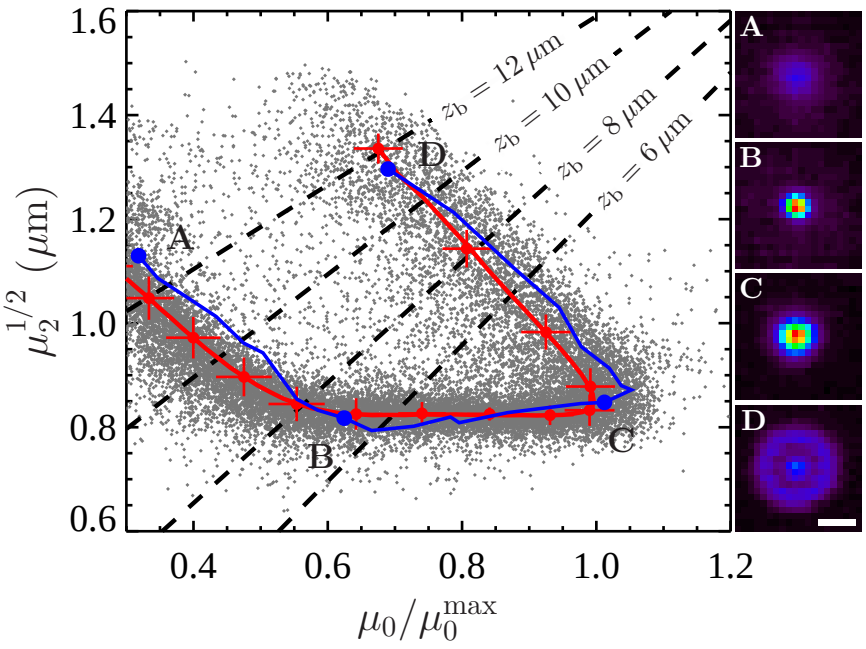

Fig. 2.5: Cluster of located features in the $(\mu_0, \mu_2^{1/2})$ space used for post-processing false particle removal. The red line correspond to the average trajectory in this parameter space as the probe travels the z direction in the volume of observation. The blue line is a single typical trajectory of the same event, and to the 4 dots labeled A, B, C and D along this line correspond the 4 particle images on the right hand side (image A is obtain when the particle is at the top edge of the volume of observation, and D is when the particle is at the bottom). The grey dots are the events for a typical tracking experiment for particles freely moving in water. The dashed lines corresponds to different clipping regions (only points below each line is kept) for false data removal, corresponding to the different values of z_b indicated on each line.

figure 2.5 the cloud of points obtained for this dynamic experiment in a viscous fluid, and observe very good agreement with the averaged red curve obtained with the static experiment in agarose. We can use the knowledge of the concentration of beads to obtain a quantitative agreement in the determination of z_b. The total instantaneous number $N_b(t)$ of tracked particles (over the 20 movies) calculated for each frame is a fluctuating variable with mean $\langle N_b \rangle = 337$ and standard deviation $(\langle N_b^2 \rangle - \langle N_b \rangle^2)^{1/2} = 17.5$ (that is, 5% of the mean). We then use $\langle N_b \rangle = 20 \times C_b x_b y_b z_b$ where $C_b = \phi/[\pi(2a)^3/6]$ is the concentration of beads. With $x_b = 202\,\mu$m and $y_b = 149.4\,\mu$m known from the magnification, we calculate a value $z_b^{(2)} = \langle N_b \rangle/(20 \times C_b x_b y_b)$ for each clipping input parameter z_b defined in the previous method (1). We report these values in table 2.2 and observe a good agreement with the previous estimation. Note that this method (2), does not depend on the particular dynamics of the particles, but as opposed to the previous method (1), it depends

$z_b^{(1)}$ (μm)	$z_b^{(2)}$ (μm)	$z_b^{(3)}$ (μm)	$\varepsilon^{(1)}$ (nm)	$\varepsilon^{(2)}$ (nm)
6 ± 1	6.0 ± 0.5	5.2 ± 0.4	9 ± 1	12 ± 7
8 ± 0.9	8.2 ± 0.5	6.7 ± 0.5	10 ± 1	14 ± 5
10 ± 0.9	10.7 ± 0.5	8.3 ± 0.8	11 ± 1	13 ± 5
12 ± 0.8	12.9 ± 0.5	9.5 ± 1	12 ± 1	15 ± 4

Table 2.2: Values of the depth of tracking z_b and of the spatial resolution ε as determined by different methods. The value $z_b^{(1)}$ of z_b is the parameter that defines the clipping region, and the corresponding $\varepsilon^{(1)}$ is the minimum spatial resolution calculated from the fixed particles remaining after clipping (see text and figure 2.5). We used the density of particles to determine $z_b^{(2)}$ from experiments in a viscous fluid. In these dynamic experiments, the spatial resolution $\varepsilon^{(2)}$ is determined from the mean-squared displacement intercept. The column $z_b^{(3)}$ are values obtained by matching the distribution of simulated trajectory durations with the corresponding distributions obtained from the particle tracking experiments in the viscous fluid (see section 2.4).

on the concentration C_b of the particles. Thus these two estimations of z_b are from two entirely independent methods. Also, using the study presented in chapter 3 we can calculate the spatial resolution from the intercept of the mean-squared displacement of the particle in the viscous fluid. These estimates $\varepsilon^{(2)}$ are also presented in table 2.2 but are affected by a large uncertainty due to statistical limitations. However, they are in the right order of magnitude as compared to the static evaluation $\varepsilon^{(1)}$.

The variations of $\mu_0(z)$ and $\mu_2^{1/2}(z)$ naturally depends on the optics, such that a different objective and different sizes of beads will give different results. Also, if the volume of observation is chosen deeper in the sample chamber, the background level is higher because of the reflected fluorescence of the layer of beads lying below the observed volume is greater in the inverted microscope geometry. This can also affect the variations of $\mu_0(z)$ and $\mu_2^{1/2}(z)$. However, the global shape of the corresponding line $(\mu_0(z), \mu_2^{1/2}(z))$ usually follows similar trends: an asymmetric drop of radius and maximum of total mass at the focal plane is essentially always observed, such that a "ring" of points similar to the one shown in figure 2.5 is obtained.

To conclude this section, we need to question the performance of this technique. The temporal resolution is mainly fixed by the frame rate of the camera, since the positions of the moving probes are evidently sampled only when a particle's image is captured on a video frame. The accuracy at which the particle is located in this image is however unanswered in this chapter. Since the position is calculated from the entire intensity profile of the particle image, through the brightness weighted centroid calculation given by equation 2.6, it is reasonable to wonder how the z-dependent shape of this profile affect the spatial resolution of the feature location. This important point will be thoroughly discussed in the next chapter.

2.4 Tracking Output Statistical Design

As pointed out in the previous section, the particles are trackable only when they travel in a given volume of observation $V_\mathrm{b} = x_\mathrm{b} y_\mathrm{b} z_\mathrm{b}$. This limitation, which is more stringent in the z direction along which the dimension of V_b is significantly smaller, is responsible for a peculiar statistical effect in the microscopy particle tracking technique. Individual trajectories of the probes are random processes, and when a statistical study is performed from the trajectory list output of the measurements, durations of the individual tracks must be carefully taken into account. For example, consider a heterogeneous system in which some particles travel throughout a porous structure, but in which a subpopulation of particles are tightly trapped in smaller pores (such behavior has been recently observed in actin gels [46]). Due to the finite volume of observation, the trajectories of the freely moving particles will be in general shorter and in higher proportion than the trajectories of the trapped probes that will remain in the volume of observation throughout the entire acquisition. This is particularly dramatic since a particle that leaves the observable space and comes back will be measured as two or more unconnected trajectories.

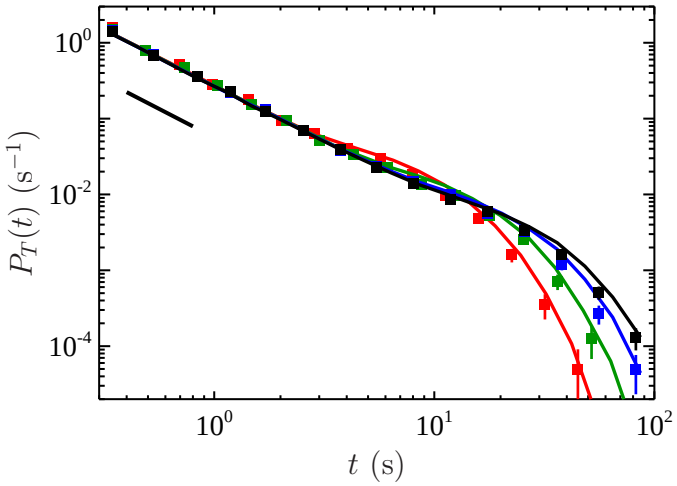

Fig. 2.6: Probability density function of trajectory durations from a 0.925 μm diameter particles tracking measurement in a 1 : 1 solution of H_2O/D_2O. The squares are experimental results obtained after using clipping region with depth of tracking parameter $z_\mathrm{b} = 6$ (red), 8 (green), 10 (blue) and 12 μm (black), whereas the respectively colored solid lines were obtained using the simulation method described in chapter 5 with corresponding values of z_b given in table 2.2. The scaling shown is $\propto T^{-3/2}$, typical of one-dimensional first passage time distribution [47].

To illustrate this peculiar statistics, we plot in figure 2.6 the probability density function of trajectory durations from the particle tracking measurement of the aqueous system described in the previous section with the various clipping parameters z_b. The material in which the particles are

moving is homogeneous, however the duration distribution shows that short tracks are highly more likely to be observed. The power-law scaling observed at short duration is typical of first-passage time distribution [47], since these short trajectories are mainly coming from particle entering and leaving the volume of observation by the same constant-z edge. This distribution depends mainly on z_b and on the dynamics of the particles, hence on the local mechanical property of the material they are probing. This fundamental problem, particularly challenging in heterogeneous system, will be treated in depth in chapter 5.

For completeness, we used the simulation method developed in chapter 5, that takes the finite imaging volume into account, to calculate the probability density function of trajectory durations in a similar viscous homogeneous material. We plot in figure 2.6 the results of these simulations performed with the values $z_\mathrm{b}^{(3)}$ of z_b that matches the best the experimental results obtained with the different clipping regions described in the previous section. The values of z_b obtain by this method (3) are reported in table 2.2. We observe that they are of the same order of magnitude as the ones estimated with particles fixed in agarose, although they are consistently smaller. This is likely to missing positions when building trajectories. Missed features in a single frame can come from several reasons: for example, if two particles are overlapping in the imaging volume, than the resulting spot want be circular or brighter, and will be discarded during the false data removal step; also, noise can bring a particle image out of the selection domain of valid data. Because of a missed position, a trajectory that was supposedly long is cut into two shorter trajectory. The distribution of trajectory durations presented in figure 2.6 is thus biased in both the short and long duration domain. This would result in an apparent smaller z_b, as observed in our results.

2.5 Conclusions

In this chapter we have unveiled the multiple particle tracking technique by adopting a very practical perspective. When the sample preparation, the observation methods and the tracking processing follow well established protocols, we have pointed out that two important problems arise. On one hand, the spatial resolution of the technique has not been characterized, and its consequences on the actual processed data (calculation of the mean-squared displacement for example) has not been quantified. On the other hand, an apparent peculiar limitation on the statistics of the stochastic output needs to be assessed. We will devote the next three chapters to bring some understanding to these problems, and we will see that they can have dramatic effects on the physical interpretation of the measurement.

CHAPTER 3

Errors in Particle Tracking Experiments

In the previous chapter we have presented the technique of video microscopy particle tracking. We have mentioned that the performance of this technique, in particular the spatial resolution of the tracking, needs to be clearly assessed. Naturally, any tracking technique has a finite spatial resolution. In this chapter we study the localization inaccuracies, not only their origin in the detection methods, but also their consequences on the measurements. This chapter was reproduced in part with permission from Savin, T. and Doyle, P. S., *Biophys. J.*, **88**, 623-638 (2005), copyright 2005 by the Biophysical Society.

3.1 Introduction

Among the applications of particle tracking, investigation of local mechanical properties of a medium, using the particle as a local probe, is frequently performed. In these studies, averaged quantities such as the mean-squared displacement or the power spectral density of the position [34] are calculated to quantify the particle's dynamics. Thus, a large amount of data must be acquired to ensure high statistical accuracy and to this regard, video microscopy is both widely available and allows the acquisition of a large amount of data in minutes leading to a great statistical accuracy.

However, a study by [48] recently showed that the limited spatial resolution of standard video microscopy particle tracking leads to errors that can significantly alter the physical interpretations. Thus, a compromise arises in the choice of the tracking technique between: on one hand, video

microscopy with great flexibility and high statistical accuracy but a low spatial resolution that limits the validity of microrheological measurements, and on the other hand, enhanced tracking techniques with a high spatial resolution but a limited extensibility to multiple particle tracking. The spatial resolution of particle tracking video microscopy has been thoroughly, both qualitatively and quantitatively, studied by observing immobilized particles [15, 20]. In the present study we refer to this contribution of the spatial resolution as the "static error" in particle localization. Due to the finite video frame acquisition time (also called exposure or shutter time), another sort of localization error arises when moving particles are observed. This contribution to the spatial resolution depends on the dynamics of the imaged particles and thus will be referred as "dynamic errors" in the text. To our knowledge, no quantitative studies have been performed on the effect of these dynamic errors on the mean-squared displacement or the power spectral density of the position. However, both types of error should be considered when calculating these two averaged quantities. We present methods to efficiently quantify the influence of these two types of errors on the estimation of the mean-squared displacement. We provide precise ways to correct for the static errors and derive expressions for the dynamic errors of several model fluids. Therefore, we show that accurate values of the mean-squared displacement can be obtained using standard video microscopy.

The balance of this chapter is organized as follows. We first present a generalized theoretical model to quantify the sources of error in particle tracking experiments, without restriction to video-based detection. We focus on the propagation of these errors on the mean-squared displacement and on the power spectral density. We then verify the model on purely viscous fluids using both simulation and experimental methods, and extend our theoretical prediction to other model fluids. Finally, we discuss the results, particularly in terms of rheological properties, to illustrate how these errors can mislead physical interpretations. Descriptions of correction methods are also presented.

3.2 Theory

In this section, we develop a model to calculate how the errors in the estimated particle position propagate on the power spectral density and the mean-squared displacement. To consider all sources of localization error, we separate the static contribution from the dynamic contribution. The so-called "static error" arises from noise inherent to any particle tracking experiment [49]. The "dynamic error" comes from the acquisition time (or shutter time) required for position measurements. In the calculations that follow, we perform averages on infinitely populated statistical ensembles and thus do not consider the inherent inaccuracy associated with the sample statistics of finite-sized ensembles. This is a good approximation in most particle tracking techniques adapted to studying local rheology as these setups are designed to acquire a large amount of data (at least 10^4 data points in most cases). A thorough statistical study of multiple particle tracking specific outputs is presented in Chapter 5. In this chapter, $\langle ... \rangle$ designates time averages for single particle tracking, while for multiple particle tracking, it designates a population and/or time average. Furthermore, the following models are general and do not require any assumptions about the dynamics of the tracked particles. For instance, results are equally valid for thermally fluctuating or actively manipulated (e.g., using optical tweezers) particles.

3.2.1 Static Error

We consider a setup that exhibits an intrinsic error in the determination of a particle's position as a result of the underlying noise in the measurements [49]. Systematic errors such as calibration inaccuracy or position- and time-independent offset are not considered here. The origin of the noise depends on the tracking setup, but without loss of generality, we assume that the true position $x(t)$ of the particle at time t is estimated by $\hat{x}(t)$ with the following relation:

$$\hat{x}(t) = x(t) + \chi(t) \ , \tag{3.1}$$

where χ is a stationary random offset with zero mean $\langle \chi(t) \rangle = 0$ and constant variance $\langle \chi^2(t) \rangle = \varepsilon^2$ that defines the spatial resolution ε of the setup. The error χ is also assumed to be independent of the position such that $\langle x(t)\chi(t') \rangle = 0$ for any (t, t'). The autocorrelation function of the position $C_x(\tau) = \langle x(t+\tau)x(t) \rangle - \langle x(t) \rangle^2$ (where τ is the lag time), is modified to

$$C_{\hat{x}}(\tau) = C_x(\tau) + C_\chi(\tau) \tag{3.2}$$

when the static errors in the measurement are taken into account. In Eq. 3.2, $C_\chi(\tau)$ is the autocorrelation function of the error. In the frequency domain, the power spectral density of the position becomes

$$\langle |\hat{x}^*|^2(\omega) \rangle = \langle |x^*|^2(\omega) \rangle + \langle |\chi^*|^2(\omega) \rangle \ , \tag{3.3}$$

as obtained by taking the Fourier transform on both sides of Eq. 3.2 and using the Wiener-Khinchin Theorem [50]. When the mean-squared displacement $\langle \Delta x^2(\tau) \rangle = \left\langle \big(x(t+\tau) - x(t)\big)^2 \right\rangle$ is to be calculated, we use the relation

$$\langle \Delta x^2(\tau) \rangle = 2C_x(0) - 2C_x(\tau) \tag{3.4}$$

to find

$$\langle \Delta \hat{x}^2(\tau) \rangle = \langle \Delta x^2(\tau) \rangle + 2\varepsilon^2 - 2C_\chi(\tau) \ , \tag{3.5}$$

where we have used the definition of the spatial resolution $C_\chi(0) = \varepsilon^2$.

3.2.2 Dynamic Error

For all experimental setups, a single measurement requires a given acquisition time σ during which the particle is continually moving. Thus, the position that is acquired at time t contains the history of the successive positions occupied by the particle during the time interval $[t - \sigma, t]$. We model this dynamic error by calculating the measured position as the average $\overline{x}(t, \sigma)$ of all the positions the particle takes while the shutter is open [51]:

$$\overline{x}(t, \sigma) = \frac{1}{\sigma} \int_0^\sigma x(t - \xi) \mathrm{d}\xi \ . \tag{3.6}$$

Note that by performing an average over the time σ, any dynamics involving variation of $x(t)$ over a characteristic time $\tau_R < \sigma$ can not be resolved. This has important ramifications as shown in several examples given in the next chapter. In the frequency domain, Eq. 3.6 becomes $\overline{x}^*(\omega, \sigma) = H^*_\sigma(\omega) \times x^*(\omega)$ with $H^*_\sigma(\omega) = (1 - e^{-i\omega\sigma})/(i\omega\sigma)$, so that the power spectral density of the position

is [50]:

$$\langle|\overline{x}^*|^2(\omega,\sigma)\rangle = |H_\sigma^*(\omega)|^2 \times \langle|x^*|^2(\omega)\rangle \quad \text{with} \quad |H_\sigma^*(\omega)|^2 = \frac{\sin^2(\omega\sigma/2)}{(\omega\sigma/2)^2} \ . \tag{3.7}$$

In the time domain, Eq. 3.7 is written $C_{\overline{x}}(\tau) = [h_\sigma * C_x](\tau)$ where $h_\sigma(\tau)$ is the inverse Fourier transform of $|H_\sigma^*(\omega)|^2$ (that is $h_\sigma(\tau) = (\sigma - |\tau|)/\sigma^2$ for $|\tau| \leq \sigma$ and $h_\sigma(\tau) = 0$ elsewhere) and $[h_\sigma * C_x]$ designates the convolution of h_σ and C_x. We can then calculate the mean-squared displacement using Eq. 3.4:

$$\langle\Delta\overline{x}^2(\tau,\sigma)\rangle = [h_\sigma * \langle\Delta x^2\rangle](\tau) - [h_\sigma * \langle\Delta x^2\rangle](0) \tag{3.8}$$

with

$$h_\sigma(\tau) = \begin{cases} (\sigma - |\tau|)/\sigma^2 & \text{for } |\tau| \leq \sigma, \\ 0 & \text{elsewhere.} \end{cases} \tag{3.9}$$

This relation is linear, but as opposed to the propagation formula for the power spectrum density (Eq. 3.7), it is rather difficult to invert. After simplifying, Eq. 3.8 can be written for $\tau \geq \sigma$:

$$\langle\Delta\overline{x}^2(\tau,\sigma)\rangle = \frac{1}{\sigma^2}\int_0^\sigma \Big[\langle\Delta x^2(\tau+\xi)\rangle + \langle\Delta x^2(\tau-\xi)\rangle - 2\langle\Delta x^2(\xi)\rangle\Big](\sigma-\xi)\mathrm{d}\xi \ . \tag{3.10}$$

We present in Chapter 4 relevant examples for model fluids that give specific insight on how the mean-squared displacement depends on this dynamic error. In the next chapter, we will also propose an alternative derivation of Eq. 3.8 in the time space rather than in the Fourier space as it is done here. After combining the contributions from the two errors, we obtain

$$\left\langle\left|\widehat{\overline{x}}^*\right|^2(\omega,\sigma)\right\rangle = |H_\sigma^*(\omega)|^2 \times \langle|x^*|^2(\omega)\rangle + \langle|\overline{\chi}^*|^2(\omega,\sigma)\rangle \tag{3.11}$$

for the measured power spectrum density, and

$$\left\langle\Delta\widehat{\overline{x}}^2(\tau,\sigma)\right\rangle = [h_\sigma * \langle\Delta x^2\rangle](\tau) - [h_\sigma * \langle\Delta x^2\rangle](0) + 2\overline{\varepsilon}^2 - 2C_{\overline{\chi}}(\tau,\sigma) \tag{3.12}$$

for the measured mean-squared displacement, where we have written the measured static error:

$$\langle|\overline{\chi}^*|^2(\omega,\sigma)\rangle = |H_\sigma^*(\omega)|^2 \times \langle|\chi^*|^2(\omega)\rangle \ , \tag{3.13}$$

$$C_{\overline{\chi}}(\tau,\sigma) = [h_\sigma * C_\chi](\tau) \quad \text{and} \quad C_{\overline{\chi}}(0,\sigma) = \overline{\varepsilon}^2 \ . \tag{3.14}$$

Note that the ideal static localization errors $\langle|\chi^*|^2(\omega)\rangle$ and $2\varepsilon^2 - 2C_\chi(\tau)$ considered at first in Eq. 3.3 and 3.5 are also transformed by the dynamic error during the course of the demonstration. It is the resulting quantities $\langle|\overline{\chi}^*|^2(\omega,\sigma)\rangle$ and $2\overline{\varepsilon}^2 - 2C_{\overline{\chi}}(\tau,\sigma)$ that are actually measured for immobilized particles, since any experimental measurement has a finite σ. This effect is usually implicitly considered in all models that relate the spatial resolution to the number of detected photons or the signal level (such as the one presented in the Appendix A). The former quantities are indeed themselves connected to the exposure time σ through the emission rate of the light source, which is detector independent. Additionally, we could have considered the dynamic errors first and then start from $\widehat{\overline{x}}(t) = \overline{x}(t) + \overline{\chi}(t)$ to obtain the same results as Eq. 3.11 and 3.12. In the rest of the article, $\langle|\overline{\chi}^*|^2(\omega,\sigma)\rangle$ and $2\overline{\varepsilon}^2 - 2C_{\overline{\chi}}(\tau,\sigma)$ will be referred as "static" errors.

3.2.3 Applications

The static localization errors are easily corrected in Eq. 3.11 and 3.12. However, in order to successfully replace the value of $\langle|\overline{\chi}^*|^2(\omega,\sigma)\rangle$ or $2\overline{\varepsilon}^2 - 2C_{\overline{\chi}}(\tau,\sigma)$ in a dynamic experiment by the one measured in a static study, one must ensure that the experimental conditions in both cases are identical. In particular, noise and signal quality must be reproduced, as $\chi(t)$ commonly depends on these parameters in the experimental data. To illustrate the importance of the dynamic errors, one can calculate the value of $|H^*_\sigma(\omega)|^2$ at the Nyquist frequency $\omega = \pi/\sigma$ (since the acquisition rate is less or equal than $1/\sigma$). We find $|H^*_\sigma(\pi/\sigma)|^2 = 0.4$, meaning that the apparent (measured) power spectral density is only 40% of its true value. In general, both the static and dynamic localization errors will have greater effect at high frequencies. As pointed out earlier, high frequency corrections can be applied on $\langle|\widehat{\overline{x}}^*|^2(\omega,\sigma)\rangle$ as the inversion of Eq. 3.7 to calculate $\langle|x^*|^2(\omega)\rangle$ is straightforward. Moreover, low frequency statistical inaccuracy of the microrheology techniques, not taken into account in the derivation, will limit the applicability of the propagation formulas Eq. 3.11 and 3.12.

In the present study, we used video microscopy to perform multiple particle tracking. In this setup, the noise primarily comes from background signal (that includes for example out of focus particles or autofluorescence of the rest of the sample), the photon shot noise, the CCD noise (readout noise and pattern noise, the dark current noise being usually negligible at video rate) and digitization noise in the frame grabber. Measurements of the noise in the electronic chain (CCD and frame grabber) is given in Appendix A.1. The tracking measurements are based on a centroid localization algorithm performed on images of particles (see Chapter 2). In this procedure, the spatial resolution can be related to the tracking parameters used for data processing and to the noise-to-signal ratio of the raw measurement. In particular, the spatial error will follow the same temporal distribution as the pixel intensity noise in the movie. From the noise characterization shown in Appendix A, the spatial error can thus be considered temporally white up to at least the frame rate frequency as well as independent of the shutter time at constant brightness. Then we can write $C_{\overline{\chi}}(\tau,\sigma) = 0$ for $\tau \geq \sigma$. Plugging this expression and $\langle\Delta x^2(\tau)\rangle = 2D|\tau|$ into Eq. 3.12, we find the apparent mean-squared displacement of a particle in a Newtonian fluid (see Eq. 3.25) for $\tau \geq \sigma$:

$$\langle\Delta\widehat{\overline{x}}^2(\tau,\sigma)\rangle = 2D\big(\tau - \sigma/3\big) + 2\overline{\varepsilon}^2 \ . \tag{3.15}$$

The self-diffusion coefficient for a spherical particle is calculated from $D = k_\mathrm{B}T/(6\pi a\eta)$, where k_B is the Boltzmann's constant, T the absolute temperature, η the viscosity of the fluid and a the particle radius. This model is verified in subsequent sections of the chapter through simulations and experiments.

Finally, a tracking setup may suffer from another sort of error called bias. It is defined as an inaccuracy in locating the particle that depends on the position [15]. In that case, χ depends on x and the correlation term $\langle x(t)\chi(t')\rangle$ can be non-zero, so that our theoretical predictions do not apply. For example, localization errors from pixelization are position depedent, as shown later in this chapter. However, we also demonstrate that these bias errors are small at typical noise-to-signal ratios encountered in our tracking technique, in accordance with the results of [15].

3.3 Specific Methods

In this section, we describe some specific method used for the study presented in this chapter.

3.3.1 Experiments

We used the multiple particle tracking technique that has been described in detail in Chapter 2. Here, $2a = 0.925\,\mu$m fluorescent beads (Polysciences, Warrington, PA) were dispersed in the sample at low volume fraction, $\phi < 0.1\%$. The samples were prepared following procedures described in section 2.1.1, and imaged using the fluorescent video microscopy setup given in section 2.1.2. We used a 63× water-immersion objective (NA=1.2) leading to an on-screen magnification of 210 nm/pxl. The focal plane was chosen near the center of the chamber (at least $40\,\mu$m away from the microscope slides) to minimize the effect of bead-surface hydrodynamic interactions on the observed dynamics. Movies were digitized at 8-bit dynamic range (that is a range from 0 to 255 analog-to-digital units or "ADU"), and recorded using the software NIH Image. The movies were analyzed off-line using the programs explained in section 2.2. Since a single video frame consists of two interlaced fields (each of them containing either the odd or the even rows of the CCD matrix) that are exposed 1/60 s apart, 60 Hz temporal resolution is achieved by analyzing each field independently. However, resolution is lost in the direction perpendicular to the interlacing [16]. Thus, in our study we analyzed particle motion in the horizontal direction (hereafter defined to be the x direction). Estimation of the spatial resolution in this direction is discussed throughout this chapter.

It is important to note here that the study of de-interlaced movie is required in order to study the effect of a finite shutter time. Indeed, the exposure time is related to the acquisition of each field individually, such that to obtain a full frame, the shutter is actually opened twice. If the full frame was analyzed to extract positions of the features, these position would actually be an average of the position extracted from each field individually, and thus the effective shutter time would be 1/60 s.

To verify the models we present here, we needed to evaluate average quantities on sufficiently populated ensembles to minimize the inaccuracy inherent to finite sample statistics. Details about this limitation are exposed in chapter 5. But briefly, to calculate the mean-squared displacement at a given lag time τ, an ensemble of displacements is built by subdividing each trajectory into fragments of length τ. Thus a particle labeled i tracked over a length T_i leads to a sample containing $\sim T_i/\tau$ trajectory steps in the statistical ensemble. Consequently, higher statistical accuracy is achieved at short lag times. In all the following, we chose the maximum lag times such that at least 5×10^4 data points were used to compute the mean-squared displacement. This leads to a relative error estimated by $(5 \times 10^4)^{-1/2} \sim 0.5\,\%$ that we verified to be well below any other sources of error.

3.3.2 Simulations

Static measurements

We first created an ensemble of 1000 images containing static Gaussian spots following the brightness distribution given by Eq. A.10 in Appendix A.2. The particles were randomly placed in the initial image and their positions did not change throughout the length of the movie. Signal independent Gaussian noise was generated and added to each frame. Such an additive model is justified for the video microscopy method used here, as shown in the Appendix A. The apparent radius was varied around the typical values observed for the particles imaged in the experiments: from 4 pxl to 5 pxl. We have investigated different noise-to-signal ratios by changing both the level of the signal and the level of the noise. The multiple particle tracking algorithms have been applied to

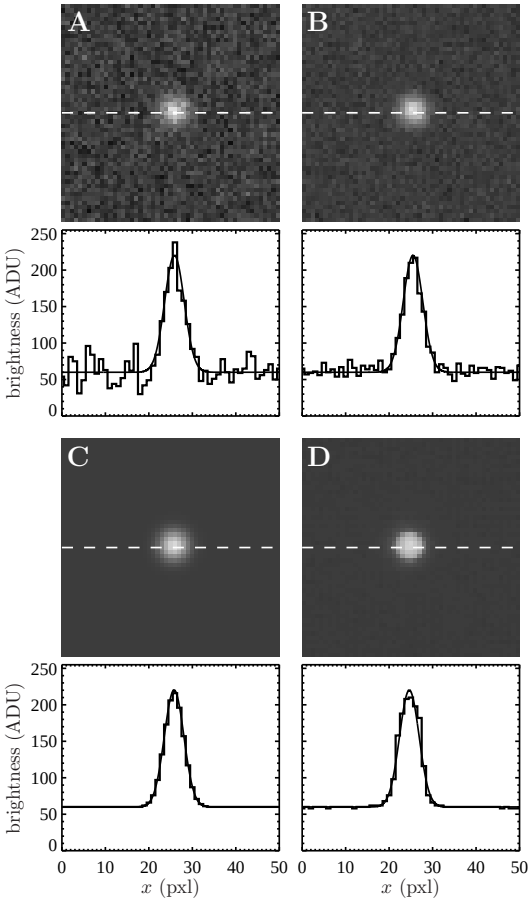

Fig. 3.1: Sample particle images created during the simulations and extracted from a typical static experiment. Corresponding brightness profiles along the white dashed line are displayed under each image, as well as the corresponding Gaussian function (*solid line*). The apparent radius in all images is $\hat{a} = 4.5\,\mathrm{pxl}$. (A), (B) and (C) are simulated Gaussian spots with the same signal levels but different noise levels. The resulting noise-to-signal ratios are respectively $N/S = 0.1$, $N/S = 0.05$ and $N/S = 0$. (D) Typical experimental profile of an in-focus particle image. The noise-to-signal ratio is $N/S = 0.01$ as extracted from our procedure. The profile differs slightly from a Gaussian function (*solid line*) and the image of the particle presents sharper edges than the theoretical Gaussian profile displayed in (C).

these movies after de-interlacing the fields (see the previous section), and the spatial resolution was measured from the mean-squared displacement $\langle \Delta\widehat{\overline{x}}^2 \rangle = 2\overline{\varepsilon}^2$ computed in the x direction of the interlacing. Fig. 3.1, A-C show typical particle images created for these movies at different noise-to-signal ratios, compared to an experimental image (Fig. 3.1D) of a particle obtained using

the static measurement described later.

Dynamic measurements

A Brownian dynamics simulation was developed to create bead trajectories. An explicit first-order algorithm [52] was used to advance the position of a particle at time t, $\mathbf{r}(t)$:

$$\mathbf{r}(t + \Delta t) = \mathbf{r}(t) + \Delta\mathbf{r} \ . \tag{3.16}$$

The displacement $\Delta\mathbf{r}$ was chosen from a Gaussian distribution satisfying

$$\langle \Delta\mathbf{r} \rangle = 0 \quad \text{and} \quad \langle \Delta\mathbf{r}\Delta\mathbf{r} \rangle = 2D\Delta t\, \boldsymbol{\delta} \ , \tag{3.17}$$

where Δt is the time step and $\boldsymbol{\delta}$ is the unit second-order tensor. Each trajectory was 10^6 time steps long and was then transformed in the following manner:

$$\overline{\mathbf{r}}(t) = \frac{1}{n} \sum_{i=0}^{n-1} \mathbf{r}(t - i\Delta t) \ , \tag{3.18}$$

where $\sigma = n\Delta t$ defines the shutter time. We chose $D = 0.5\,\mu\mathrm{m}^2/\mathrm{s}$, varied n between 10 and 100, and set the time step to $\Delta t = 1/6000\,\mathrm{s}$ which is 1/100 the value of the frame-rate ($1/60\,\mathrm{s}$). Thus, the shutter time varied between 1/60 and $1/600\,\mathrm{s}$ and we spanned a range of $D\sigma$ that is comparable to that found in the experiments. Also, we verified that our results did not appreciably change for smaller values of the time step Δt. On the resulting walks, a Gaussian distributed random offset with different standard deviations $\overline{\varepsilon}$ ranging from 0.01 to $0.05\,\mu\mathrm{m}$ was added to each position. Fig. 3.2 illustrates the different stages of the simulation. Results were generated from an ensemble of 100 trajectories.

3.3.3 N/S Ratio Extraction

Extracting the statistics of noise present in typical images produced by video microscopy particle tracking experiments is a challenging task. As explained in Appendix A.1, noise in the images is the result of several independent contributions, and its smallest correlation length is $l_\mathrm{n} = 1\,\mathrm{pxl}$. However, the signal's spatial frequency domain also includes the frequency $1\,\mathrm{pxl}^{-1}$, as the edges of the particle images are sharp. Thus, performing high-pass linear filtering using spatial operators (convolution) or frequency operators (Fourier transformation) that select only the noise frequency in the image will not provide a true estimate of the noise. Non-linear filters (like the median operator) and morphological grayscale operators (for example, the opening operator) are often used to reduce the noise in an image [53]. However, they possess the property of retaining the extreme brightness values of the raw image in the filtered result. Furthermore, an image obtained by subtracting the pixel values of the filtered image from the raw image contains black spots (zero brightness) where the particles are located. Thus, the brightness distribution of the noise isolated in this image includes an over-populated peak at 0 ADU, and the noise level is underestimated.

This suggests that the noise can not be evaluated at the particle positions, but only in the region of the raw image that is around the particles. We explain later some limitations of our method following from this observation. To isolate this region of interest, we used similar methods

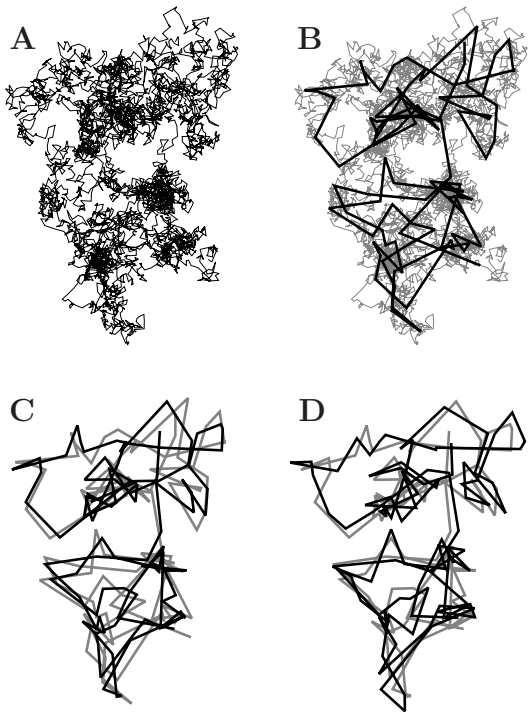

Fig. 3.2: Illustration of the dynamic simulation process to create trajectories of a Brownian particle which are sampled with a finite shutter time. First, a trajectory with a large number of time steps is created (A). In the second image, positions every 50 time steps are retained (B). In the third image, a position is recalculated by averaging the position of the particle at the previous 20 time steps (C). Finally, Gaussian random noise is added in each position (D). Gray trajectories are displayed to compare successive steps of calculation.

encountered in the tracking algorithms. We calculated two filtered images out of the raw data array: a noise-reduced image G, obtained after convolution with a Gaussian kernel of half width $l_\mathrm{n} = 1\,\mathrm{pxl}$, and a background image B, obtained by convolving the raw image with a constant kernel of size $2w + 1$ (w is the typical radius of the mask used for centroid computation, see [16] and the Appendix A for more details). We used the criteria $G - B \geq 1\,\mathrm{ADU}$ (or equivalently $G - B \geq 0.5$ if the images G and B are higher precision data arrays) to define the signal region that is complementary to the region of interest in the whole image (see Fig. 3.3B). As this criteria is very efficient in discriminating signal from sharp-edged spots (compare Fig. 3.3A and Fig. 3.3B), it does not select the whole signal arising from a larger object with smooth edges. This effect is illustrated in Fig. 3.4. To solve this issue, we then applied a binary dilation morphological operation on the resulting image with a $2w$ diameter disk as the structuring element. This has the effect to extend the area of influence of each of the spot revealed by the previous criteria (compare Fig. 3.3B and

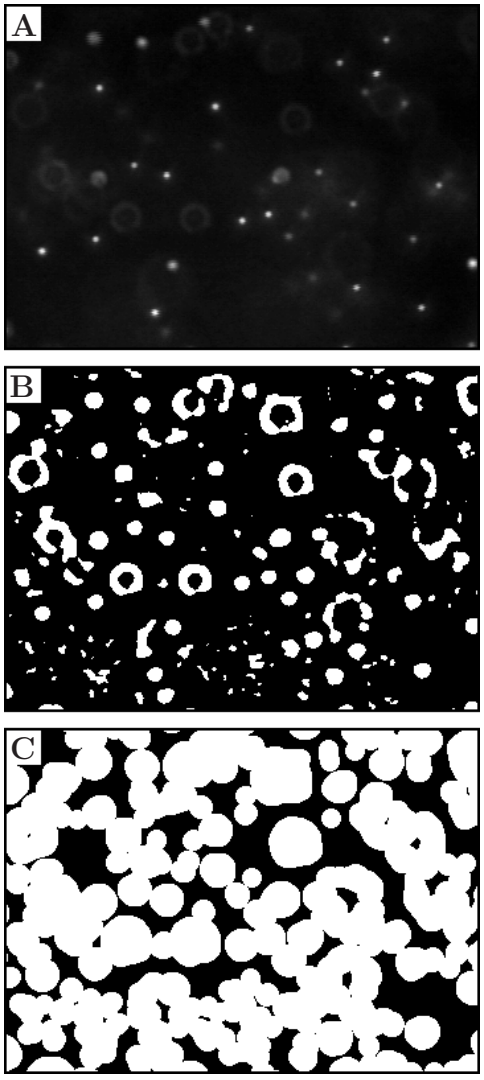

Fig. 3.3: Principle for the extraction of the noise-to-signal ratio N/S from a single movie frame. (A) A raw image taken out of a typical experimental movie for dynamic measurements. For clarity, intensity has been scaled to lie in the whole range from 0 to 255 ADU. (B) Regions of signal (*white regions*) selected based on the criteria that in these regions the noise-reduced image exceed the background image by 1 ADU or more (see text). (C) Result of the binary dilation operation applied on the previous image. This operation is required as the previous signal extraction does not include large images of out of focus particles (see Fig. 3.4). The black area is the region of interest that will be used to calculate the noise.

Fig. 3.3C). This last operation potentially eliminates several valid data points, but it significantly prevents the noise distribution from being biased by unwanted high brightness values that might be found near the particle images. Fig. 3.3 illustrates the different steps of our method, applied on a typical dynamic image. The noise is then the standard deviation of the brightness values of the raw image mapped to the region of interest.

Extraction of the signal is more straightforward. Only images of particles that participate in the statistical study are considered. The signal is then well defined by the difference between the local maximum brightness value of the spot and the average brightness value around the spot.

This method has been successfully verified on the simulated images and on the static experiments presented in the next section to an accuracy of 96%. However, this method has several limitations. For example, the concentration of particles can not be too high because the region of interest for the noise extraction will not be found. Another important limitation is the assumption that the noise is spatially uniform. This is required to have a noise level in the region around the particles (where the noise is extracted by our procedure) that is identical to the one found where the particles are located (which influences the particle position estimation). By construction, this is the case for the simulations. In real images, non-uniformity of noise can be caused by its signal dependency (as it is the case for the shot noise contribution for example). We show however in the Appendix A that this has a negligible effect. Other sources of non-uniformity include uneven illumination in the field of view or autofluorescence of the rest of the sample. Thus the background noise can have a wide range of spatial frequencies. We explain in the Appendix A that even background noise with a large correlation length has negligible influence in our setup. In addition, for dynamic experiments the computation of noise on a single frame can be biased by background fluorescence coming from particles that are out of focus and do not influence the estimation of positions for detected particles. An average over all frames takes advantage of the background fluorescence time fluctuations to accurately determine the noise involved in the particle localization. However, if the medium is too stiff or viscous, large motions of the particles are suppressed over the time scale of a movie. Thus, this eventual bias in the noise is constant throughout the entire length of the movie and the noise is not accurately estimated.

3.4 Results

3.4.1 Estimation of $\bar{\varepsilon}$ Using Fixed Beads

To experimentally estimate $\bar{\varepsilon}$, we fixed the fluorescent probes on a glass microscope slide, recorded movies containing 1000 frames of the immobilized beads with different shutter times, and performed the multiple particle tracking algorithm on the deinterlaced movies. We retained only the x position for each particle, and discriminated isolated particles from aggregates of several particles. We were able to vary the noise-to-signal ratio by changing the intensity of the excitation light source using neutral density filters. By varying the plane of observation, the particle images were captured in and out of focus to provide images that are similar to those actually observed in dynamic studies. Apparent radius and signal level were also varied in this manner. The noise-to-signal ratio was extracted from each frame using the procedure described in the previous section, and the overall ratio was estimated by averaging over the entire movie. The resulting estimate of noise-to-signal ratio compared well with measurements performed on manually extracted background regions in several frames.

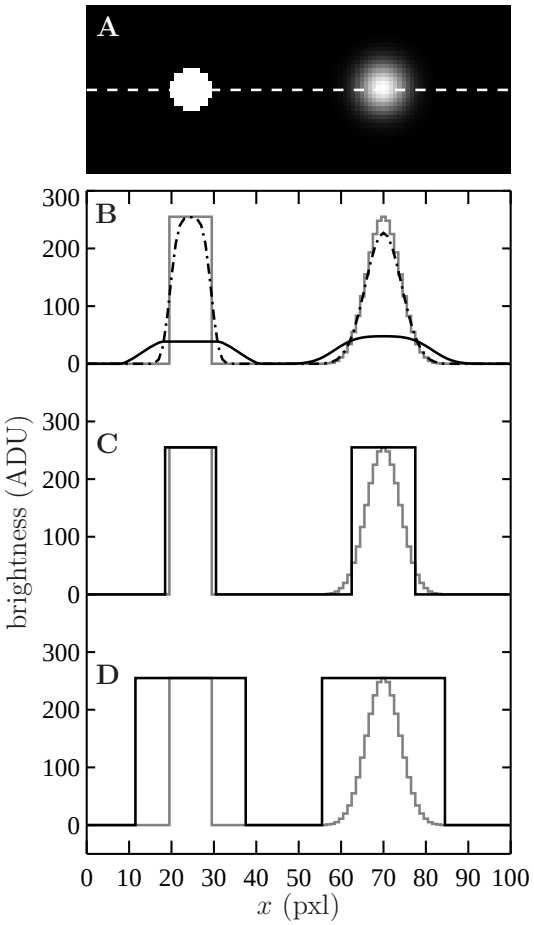

Fig. 3.4: The use of the binary dilation operation for signal area selection. (A) are model particle images: a hat-like spot on the left and a Gaussian spot on the right, both with comparable apparent radius. In (B), (C) and (D), gray lines are brightness profiles along the white dashed line seen in (A). (B) Brightness profile of the results of the background filter (*solid line*) and the noise-reduction filter (*dashed-dotted line*). (C) The solid line represents the signal selection using the criteria that the noise-reduced image exceed the background image by 1 ADU or more; this criteria is efficient for hat-like profile whereas the Gaussian profile is not fully selected. (D) Selected signal after applying the binary dilation operation on the previous selection; both profiles are now fully included in this selection.

We successfully compared the standard deviation $\bar{\varepsilon} = \left(\langle \widehat{\bar{x}}^2 \rangle - \langle \widehat{\bar{x}} \rangle^2\right)^{1/2}$ that defines the spatial resolution $\bar{\varepsilon}$ calculated from the individual trajectories with the value calculated from the mean-squared displacement $\bar{\varepsilon} = \left(\langle \Delta\widehat{\bar{x}}^2 \rangle / 2\right)^{1/2}$ at short lag time τ, for which statistical accuracy is best

(see section 3.3). Fig. 3.5A shows the experimental variation of $\overline{\varepsilon}$ with N/S, as compared to the theoretical predictions given by Eq. A.16 and Eq. A.21 obtained using respectively Gaussian and hat-like spots for the particle images (cf. Fig. 3.4A). We found good agreement between the theory applied on Gaussian spots (Eq. A.16) and the experimental data. The scatter of the points around the linear fit (solid line in Fig. 3.5) comes from different apparent radii encountered in the experiment. Fig. 3.5B compares the results of the simulation with the theoretical slopes. Since the Gaussian form was chosen for the spot in the simulations, the slight difference of the results with theory comes only from the pixelization of the images that is taken into account in the simulations. However in the experiments, the pixelization is also inherent and the linear fit mainly exhibits values of $\overline{\varepsilon}$ smaller than found in the simulations: $\overline{\varepsilon} = 268.5 \times N/S + 1.3\,\mathrm{nm}$ for the experimental data (solid line in Fig. 3.5) as compared to $\overline{\varepsilon} = 314.5 \times N/S + 0.2\,\mathrm{nm}$ on average for the simulation (not shown in Fig. 3.5). This difference arises from the true experimental shape of the spot seen in Fig. 3.1D, which has sharper edges than the Gaussian form. Thus we found that the experimental behavior slightly deviates from the Gaussian behavior toward the hat-spot behavior.

Another effect of pixelization is to create a constant offset $\Delta\widehat{\overline{x}}_{\mathrm{off}}$ between the position estimated in the odd and even field for a single immobile particle. We show in Fig. 3.6A an experimental observation of this constant shift. As a result, the trajectory $\widehat{\overline{x}}(t)$ of a single particle exhibits a 30 Hz periodic signal with amplitude $\Delta\widehat{\overline{x}}_{\mathrm{off}}$. The resulting mean-squared displacement averaged over an ensemble of fixed beads also oscillates between $2\overline{\varepsilon}^2$ and $\langle\Delta\widehat{\overline{x}}^2_{\mathrm{off}}\rangle + 2\overline{\varepsilon}^2$, so that our estimation of $\overline{\varepsilon}$ is biased. Furthermore, one can not expect to see $\overline{\varepsilon}$ vanishing as N/S approaches 0. From our experiments at low noise-to-signal ratio, we measured $\left(\langle\Delta\widehat{\overline{x}}^2_{\mathrm{off}}\rangle\right)^{1/2} \sim \langle|\Delta\widehat{\overline{x}}_{\mathrm{off}}|\rangle \sim 1\,\mathrm{nm}$. The causes of such an offset can be multiple: different noise and/or signal in the even and odd field coming from the acquisition, spatial distortion, etc... We investigated one cause that is closely related to image pixelization. As illustrated in Fig. 3.6B, this offset depends on the position $(\delta x, \delta y)$ of the real profile center inside a single pixel (see Fig. 3.6B for precise definition of δx and δy). We calculated the distribution of the values taken by $\Delta\widehat{\overline{x}}_{\mathrm{off}}$ as both δx and δy uniformly spans the range $[-0.5, 0.5[$ pxl, by using our simulation technique with Gaussian spots and $N/S = 0$. We found that $\left(\langle\Delta\widehat{\overline{x}}^2_{\mathrm{off}}\rangle\right)^{1/2} \sim \langle|\Delta\widehat{\overline{x}}_{\mathrm{off}}|\rangle \sim 0.5\,\mathrm{nm}$ and is fairly independent of the apparent radius of the particle in the range $\hat{a}$ equals 4 to 5 pxl.

Finally, we used the static simulations to evaluate the bias error described in the Theory section. In each frame we compared the true position of each particle (an input in our simulation) with the corresponding value found by the tracking algorithm. After time-averaging over all frames, we found the bias $\left\langle\widehat{\overline{x}} - \overline{x}\right\rangle = b(\overline{x})$ to be a 1 pxl periodic function of the x position of the bead, fairly independent of the noise-to-signal ratio for $N/S < 0.1$ and of the apparent radius for $4 < \hat{a} < 5\,\mathrm{pxl}$, comparable to results obtained by [15]. In Fig. 3.6C, we show the measured bias $b(\delta x)$ on both fields, odd and even, and for δx in the range $[-0.5, 0.5[$ pxl and $\delta y = 0$ (the shape is not appreciably modified for other values of δy). Also, when averaged over all particles, $\langle b^2\rangle^{1/2} \sim \langle|b|\rangle \sim 10^{-2}\,\mathrm{pxl} \sim 2\,\mathrm{nm}$. As opposed to the field offset described in the previous paragraph, the bias is not a component of the mean-squared displacement for the static experiments, as it adds a time independent offset to each immobile particle position. In dynamic experiments, it will have negligible influence since $\langle b(\overline{x})^2\rangle < 4\,\mathrm{nm}^2$ is much smaller than a typical value of $100\,\mathrm{nm}^2$ for $\overline{\varepsilon}^2$ (see next section). Additionally, the cross correlation of $\overline{x}(t)$ and $b(\overline{x}(t))$ needs to be evaluated (see the Theory section 3.2 of this chapter) and is negligible in many circumstances as shown in the next section.

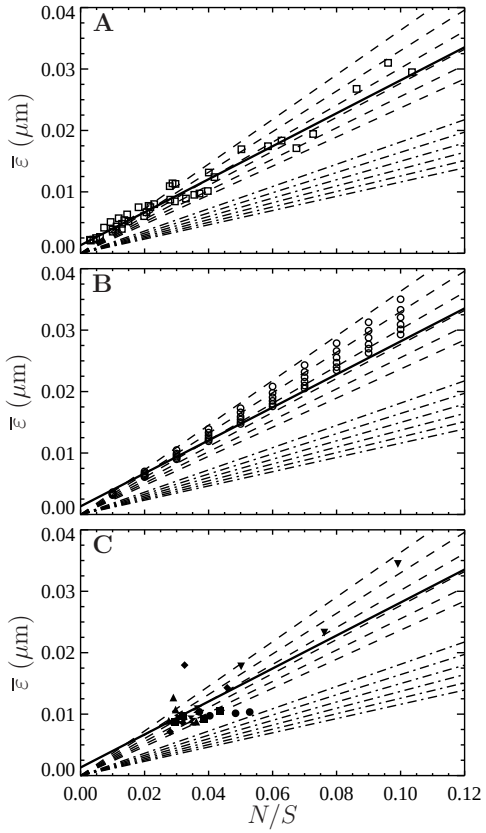

Fig. 3.5: Evolution of the spatial resolution $\bar{\varepsilon}$ with the noise-to-signal ratio N/S. For all three plots, the dashed lines and the dashed-dotted lines are theoretical slopes calculated from Eq. A.16 and Eq. A.21 respectively, with $w = 7\,\text{pxl}$ and $\hat{a}$ evenly incremented from 4 to 5 pxl (the slopes increase as $\hat{a}$ decreases). The solid line is the linear fit to the experimental static measurements: $\bar{\varepsilon} = 268.5 \times N/S + 1.3\,\text{nm}$. (A) Experimental evaluation of $\bar{\varepsilon}$ at different N/S using fixed beads (*squares*). Apparent radius $\hat{a}$ extracted from particle images ranged from 4.09 to 4.96 pxl. The non-zero y-intercept in the linear fit comes from the constant offset between positions calculated from odd and even field images (see text and Fig. 3.6). (B) Result of the simulations (*open circles*) for $w = 7\,\text{pxl}$ and $\hat{a}$ ranging from 4 to 5 pxl. We verify the linear behavior of $\bar{\varepsilon}$ versus N/S, with increasing slopes as $\hat{a}$ decreases. However, because the pixelization is inherent in the simulations, there are systematic deviations from the corresponding theoretical slopes computed using Eq. A.16 with same $\hat{a}$ (*dashed lines*). (C) Data extracted from the same set of dynamic experiments shown in Fig. 3.7, using values of $\bar{\varepsilon}$ as calculated by Eq. 3.21 (symbols are the same as in Fig. 3.7).

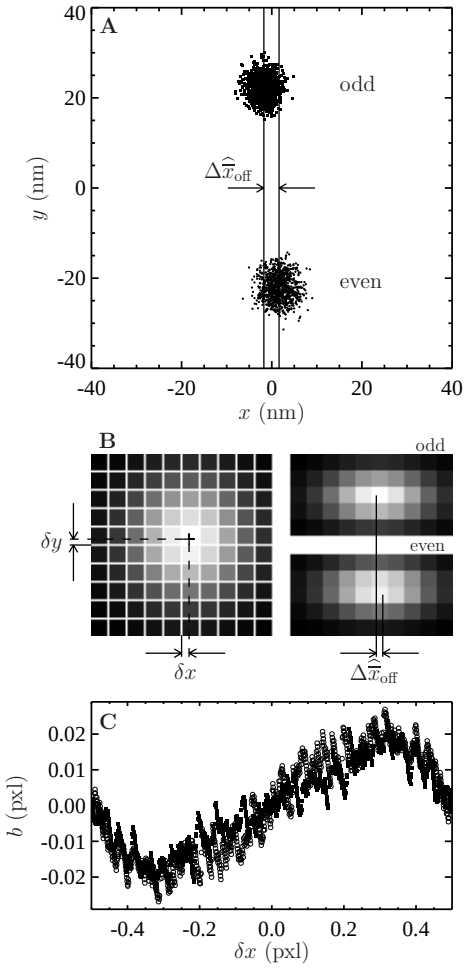

Fig. 3.6: Illustration of the position offset and bias measured from the two different camera fields. (A) Experimental position measurements of a single particle fixed to a slide at low noise-to-signal ratio ($N/S = 0.005$). The dots are results of 1000 measurements, and present two distinctly different positions extracted from the two fields. The offset in the y direction perpendicular to the interlacing is significant. The offset $\Delta\widehat{\overline{x}}_{\rm off}$ is calculated by differencing the averaged position estimated in each field (the two solid lines). (B) Schematic of a model to explain the observed offset. On the left, the center of a Gaussian spot is positioned at $(\delta x, \delta y)$ of a pixel corner. On the right, the resulting positions estimated from the odd and the even field of the same image are shifted (the magnitude of $\Delta\widehat{\overline{x}}_{\rm off}$ has been increased for clarity). (C) Measurement of the bias as a function of the position of the particle from a pixel corner at low N/S. The different symbols correspond to the two different fields, such that the difference of the two plots corresponds to $\Delta\widehat{\overline{x}}_{\rm off}$.

3.4.2 Dynamic Error

To verify Eq. 3.15, we applied multiple particle tracking on water and on solutions of glycerol at concentrations 20%, 40%, 55% and 82% volume fraction. The expected viscosities for these five

Newtonian solutions at room temperature ($T = 23°\mathrm{C}$) are approximately 1, 2, 5, 10, and 100 mPa× s respectively, weakly modified by the addition of particles at low volume fraction. We recorded movies of the fluorescent beads for a length of 5000 frames at 30 Hz (2 min 45 s), that is 10000 fields at 60 Hz. Four shutter times were used for acquisition: $\sigma = 1/60,\ 1/125,\ 1/250$ and $1/500$ s. These long movies provided enough statistics to accurately estimate the mean-squared displacement at small lag time, and the intercept $\langle \Delta\widehat{\overline{x}}^2(0,\sigma)\rangle$ and the slope $2D$ were evaluated by linear fit of the mean-squared displacement for lag times ranging from 1/60 s to 0.1 s (i.e., using the first six experimental points). We verified that at these lag times, at least 5×10^4 trajectory steps were used to compute the mean-squared displacement (see the Specific Methods section 3.3).

Fig. 3.7, A and B shows the variation of the intercept with the scaled shutter time $D\sigma$ for both these experiments and the simulations described earlier. According to relation Eq. 3.15, the theoretical model predicts

$$\langle \Delta\widehat{\overline{x}}^2(0,\sigma)\rangle = -2/3 \times (D\sigma) + 2\overline{\varepsilon}^2 \ . \tag{3.19}$$

This formula was verified by our experiments and simulations. For the simulations, we found the slope of -2/3 and the intercepts of the lines compared well with $2\overline{\varepsilon}^2$, where $\overline{\varepsilon}$ is the spatial resolution we input into the simulation. For the experimental data, we also found a slope of -2/3 and extracted a constant intercept of $2 \times 10^{-4}\ \mu\mathrm{m}^2$ leading to an average spatial resolution $\overline{\varepsilon} = 10$ nm. We show in Fig. 3.7C the error in the measured mean-squared displacement intercept as compared to the theoretical behavior expected for $\overline{\varepsilon} = 10$ nm. For both simulations and experiments, we computed this error in the following way:

$$\text{relative error} = \left| \frac{\langle \Delta\widehat{\overline{x}}^2(0,\sigma)\rangle - (2 \times 10^{-4} - 2D\sigma/3)}{(2 \times 10^{-4} - 2D\sigma/3)} \right| , \tag{3.20}$$

where both $\langle \Delta\widehat{\overline{x}}^2(0,\sigma)\rangle$ and $D\sigma$ are expressed in $\mu\mathrm{m}^2$. When $2D\sigma/3 \sim 2 \times 10^{-4}\,\mu\mathrm{m}^2$, the values of $\langle \Delta\widehat{\overline{x}}^2(0,\sigma)\rangle$ are small and the corresponding relative error can reach large values. This explains the peak observed in Fig. 3.7C at $D\sigma \sim 3 \times 10^{-4}\,\mu\mathrm{m}^2$. For other values of $D\sigma$, the relative error is approximatively 2% or less and 10% or less for simulations and experiments respectively.

Our results were aligned on a unique master line of slope -2/3 and intercept $2\overline{\varepsilon}^2$ only if $\overline{\varepsilon}$ was kept identical from one tracking experiment to the other. As suggested by our static study, we had to verify that the noise-to-signal ratio was kept identical from one movie to another. This is an experimental challenge because the noise-to-signal ratio can not be evaluated *a priori*. Since the illumination collected by the CCD decreases as the shutter time is reduced, identical signal was recovered by raising the intensity of the excitation light source. However, we had no control over the resulting noise. Thus, to validate our measurements, we computed the exact spatial resolution $\overline{\varepsilon}$ using the inverted formula

$$\overline{\varepsilon} = \left(\langle \Delta\widehat{\overline{x}}^2(0,\sigma)\rangle/2 + D\sigma/3\right)^{1/2} , \tag{3.21}$$

and we extracted the noise-to-signal ratio using the procedure explained earlier. The resulting points compare well with the static study, as shown on Fig. 3.5C. However several data points present significant deviation from the averaged static measurements. The noise-to-signal ratio of two points extracted from experiments made with 82% glycerol (*filled circles*) are over-estimated. In the movies corresponding to these two data points, the background fluorescence is not uniform, and the noise level calculated by our algorithm deviates from the actual noise influencing the

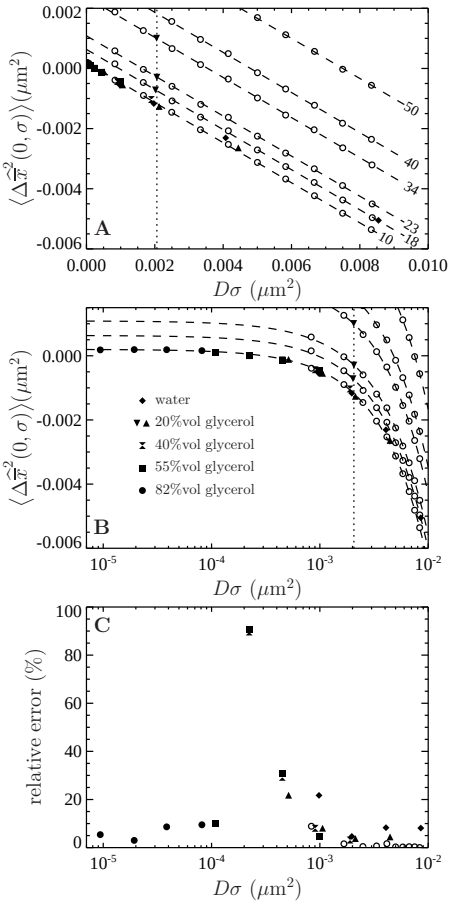

Fig. 3.7: Dependence of the mean-squared displacement intercept $\langle\Delta\widehat{\overline{x}}^2(0,\sigma)\rangle$ on the scaled shutter time $D\sigma$. Both $\langle\Delta\widehat{\overline{x}}^2(0,\sigma)\rangle$ and D are evaluated from a linear fit at small lag time. The filled symbols are from experimental results and the open circles are from simulations. For all experiments, the noise-to-signal ratio was kept constant, except for the inverted triangles which are extracted from a set of experiments in 20% glycerol with $\sigma = 1/125\,\mathrm{s}$ that have been performed with different noise-to-signal ratio (the dotted lines in (A) and (B) indicates the averaged $D\sigma$ for this set of experiments). (A) Linear-linear plot. The dashed lines represent slopes of -2/3 with intercept $2\overline{\varepsilon}^2$ (the value of $\overline{\varepsilon}$ is indicated in nanometers on the right hand side of each line). The simulation results lie on the lines with corresponding input values of $\overline{\varepsilon}$ (see text), and the experimental points obtained at identical noise-to-signal ratio (see Fig. 3.5) are in accordance with an intercept of 2×10^{-4} μm^2 ($\overline{\varepsilon} = 10\,\mathrm{nm}$). The set of experiments performed at fixed $D\sigma$ but with different N/S lie on lines with different intercepts corresponding to different values of $\overline{\varepsilon}$. (B) Linear-log plot to expand the region at small scaled shutter time $D\sigma$. (C) Relative error to the theoretical trend $2 \times 10^{-4} - 2D\sigma/3$ μm^2, as calculated using Eq. 3.20. The peak in the error corresponds to the regime where $2D\sigma/3 \sim 2\times10^{-4}$ μm^2 (see text).

particle centroid positioning. This bias constantly effects the noise estimation because the highly viscous medium eliminates relevant variations of the background fluorescence over the duration of the movie. Thus, the noise-to-signal ratio resulting from a time average over the whole movie is inaccurate. This limitation of our N/S extraction procedure was pointed out earlier. Also, two points exhibits larger values of $\bar{\varepsilon}$ than expected. They correspond to the larger values of $D\sigma$ encountered in our set of experiments: in water (*diamond*) and in 20% glycerol (*triangle*) with $\sigma = 1/60\,\mathrm{s}$. However, as seen in Fig. 3.7C, the corresponding relative error, more relevant because given in terms of mean-squared displacement, does not exceed 10%.

To complete the experimental verification of Eq. 3.19, we performed an additional set of experiments in which $D\sigma$ was kept constant, but the noise-to-signal ratio was varied. Beads were tracked in 20% glycerol solution and movies were acquired at $\sigma = 1/125\,\mathrm{s}$, giving $D\sigma \sim 2\times10^{-3}\ \mu\mathrm{m}^2$. The results are shown in Fig. 3.5 and Fig. 3.7 by the inverted triangles. For N/S evenly incremented from 0.03 to 0.1, identical $D\sigma$ were extracted (see the dotted line in Fig. 3.7A), and the exact spatial resolution calculated using Eq. 3.21 is in good agreement with the static experiments (cf. Fig. 3.5C).

Finally, we investigated the influence of bias on the mean-squared displacement. We used the Brownian dynamics simulations to create 1 dimensional trajectories $\overline{x}(t)$, and added a position dependent localization error $\overline{\chi}(t) = b(\overline{x}(t))$ at each time step. The bias is well modeled by $b(x) = 0.02\times\sin(2\pi x)$ where both b and x are expressed in pixels (see Fig. 3.6C). The bias is negligible when particle motions amplitude $(Dt_{\mathrm{tot}})^{1/2}$ (where t_{tot} is the duration of tracking) is large as compared to the bias period of 1 pxl. We observe that for $1\,\mu$m diameter beads tracked for 3 min, the bias remains negligible for solutions up to 1000 times more viscous than pure water when only time average on a single particle is performed, but to much higher values when a population average is performed on several particle trajectories.

3.5 Further Theoretical Results

In this section we use Eq. 3.10 to calculate the dynamic error for three standard model fluids. The Voigt and Maxwell fluids are the simplest viscoelastic model fluids that are commonly used to model the mechanical response of biological materials [54, 55]. A third model in which the mean-squared displacement exhibits a power-law dependency with the lag time is also investigated. This model is relevant to microrheological studies, where data is often locally fit to a power-law in order to easily extract viscoelastic properties [37]. This last model is also known as the structural damping model, recently used to fit the mechanical response of living cells [56].

In the next chapter we will expose an extended study of the effect of dynamic errors on model fluids and gain a deeper understanding of this peculiar effect.

3.5.1 Voigt Fluid

We first examine the Voigt model [54] for which the complex shear modulus frequency spectrum is of the form $G^*(\omega) = G(1 + i\omega\tau_R)$, where τ_R is the fluid's relaxation time. In such a medium, the mean-squared displacement of an inertialess bead is that of a particle attached to a damped oscillator:

$$\langle \Delta x^2(\tau)\rangle = \Delta x_0^2\big(1 - e^{-\tau/\tau_R}\big) \quad \text{with} \quad \Delta x_0^2 = \frac{2k_{\mathrm{B}}T}{6\pi a G}\ . \tag{3.22}$$

Using Eq. 3.10, we then calculate

$$\langle \Delta\overline{x}^2(\tau,\sigma)\rangle = \Delta x_0^2\left[\frac{e^{-\sigma/\tau_R}-1+(\sigma/\tau_R)}{(\sigma/\tau_R)^2/2} - e^{-\tau/\tau_R}\frac{\cosh(\sigma/\tau_R)-1}{(\sigma/\tau_R)^2/2}\right] , \tag{3.23}$$

for which we verify

$$\langle \Delta\overline{x}^2(\tau,0)\rangle = \langle \Delta x^2(\tau)\rangle \ . \tag{3.24}$$

The viscous limit is obtained for $\tau/\tau_R \ll 1$ (since $\sigma < \tau$, we have also $\sigma/\tau_R \ll 1$):

$$\langle \Delta\overline{x}^2(\tau,\sigma)\rangle = 2D\big(\tau-\sigma/3\big) \ , \tag{3.25}$$

where $D = k_\mathrm{B}T/(6\pi a\eta)$ is the bead self-diffusion coefficient and η is the viscosity of the fluid ($\eta = G\tau_R$ in the Voigt model). Equation 3.25 was found by [19] and is experimentally verified in our study. The elastic limit is obtained when $\tau/\tau_R \gg 1$ for which

$$\langle \Delta\overline{x}^2(\tau,\sigma)\rangle = \Delta x_0^2\frac{e^{-\sigma/\tau_R}-1+(\sigma/\tau_R)}{(\sigma/\tau_R)^2/2} \ . \tag{3.26}$$

Furthermore, if $\sigma/\tau_R \gg 1$, as is the case for a purely elastic solid ($\tau_R = 0$), we find that $\Delta\overline{x}^2(\tau,\sigma) = 0$. As previously mentioned, dynamics occurring at time scales smaller than σ can not be resolved. This is a fundamental problem encountered when studying Maxwell fluids, as outlined in the next section.

3.5.2 Maxwell Fluid

For the Maxwell fluid model [54], $G^*(\omega) = Gi\omega\tau_R/(1+i\omega\tau_R)$, and the mean-squared displacement of an inertialess embedded bead is [57]

$$\langle \Delta x^2(\tau)\rangle = \Delta x_0^2\big(1+\tau/\tau_R\big) \quad \text{with} \quad \Delta x_0^2 = \frac{2k_\mathrm{B}T}{6\pi aG} \ , \tag{3.27}$$

for which we calculate:

$$\langle \Delta\overline{x}^2(\tau,\sigma)\rangle = \frac{\Delta x_0^2}{\tau_R}\big(\tau-\sigma/3\big) \ . \tag{3.28}$$

This result is identical to that found for a purely viscous fluid (Eq. 3.25). The plateau region observed in Eq. 3.27 for $\tau < \tau_R$ corresponds to a frictionless bead in a harmonic potential. Since we also neglect inertia in this model, it is a peculiar limit where the particle can sample all possible positions infinitely fast. Thus, after position averaging over any finite time scale, the particle is apparently immobile and the resulting mean-squared displacement is zero. Consequently, the elastic contribution in Eq. 3.27 is unobservable. This limit is exposed in detail in chapter 4.

3.5.3 Power-Law Mean-Squared Displacement

The propagation of the dynamic error can be applied to a regime in which the mean-squared displacement follows a power-law:

$$\langle \Delta x^2(\tau)\rangle = A\tau^\alpha \ , \tag{3.29}$$

or in a dimensionless form with $\tilde{x}^2 = x^2/(A\sigma^\alpha)$ and $\tilde{\tau} = \tau/\sigma$:

$$\langle \Delta\tilde{x}^2(\tilde{\tau})\rangle = \tilde{\tau}^\alpha \ . \tag{3.30}$$

We find

$$\langle \Delta\overline{\tilde{x}}^2(\tilde{\tau})\rangle = \frac{(\tilde{\tau}+1)^{2+\alpha} + (\tilde{\tau}-1)^{2+\alpha} - 2\tilde{\tau}^{2+\alpha} - 2}{(1+\alpha)(2+\alpha)} \ . \tag{3.31}$$

In Fig. 3.8A we compare the true mean-squared displacement $\langle \Delta\tilde{x}^2(\tilde{\tau})\rangle$ with the one that includes our model dynamic error $\langle \Delta\overline{\tilde{x}}^2(\tilde{\tau})\rangle$. We see that the amplitude of the Brownian fluctuation is decreased by this error (lower apparent mean-squared dispacement). At the smallest lag time $\tilde{\tau} = 1$, we calculate the apparent diffusive coefficient as a function of the true α:

$$\overline{\alpha}(\tilde{\tau}=1) = \left.\frac{\mathrm{d}\big(\log\langle \Delta\overline{\tilde{x}}^2(\tilde{\tau})\rangle\big)}{\mathrm{d}\big(\log\tilde{\tau}\big)}\right|_{\tilde{\tau}=1} = 1 + \frac{\alpha}{2} > 1 \ , \tag{3.32}$$

which means that apparent superdiffusion will always be induced by the dynamic error. This can lead to significant misinterpretation of experimental data (see the Discussion section 3.6).

To establish a criterion to neglect dynamic error, we evaluate the minimum dimensionless lag time $\tilde{\tau}_{99\%}$ such that, for $\tilde{\tau} > \tilde{\tau}_{99\%}$, we have $\langle \Delta\overline{\tilde{x}}^2(\tilde{\tau})\rangle / \langle \Delta\tilde{x}^2(\tilde{\tau})\rangle = 99\%$ at least. In Fig. 3.8B, we computed $\tilde{\tau}_{99\%}$ for α ranging in $]0,1]$. We see that as the material gets stiffer (that is, as α decreases), the criteria $\tilde{\tau} \gg 1$ is not sufficient to avoid large dynamic error.

3.6 Discussion

We have classified the sources of spatial errors of particle tracking into two separate classes: static and dynamic. We have been able to precisely quantify each contribution for the particular case of Brownian particles moving in purely viscous fluids. Theoretical models for the errors were developed and validated using both simulations and experiments. The magnitudes of the static and dynamic errors were varied by respectively changing the noise-to-signal ratio and the shutter time of the measurements. In the Newtonian fluids we studied with video microscopy, both dependencies are linear. We found that the contributions from the two errors have antagonistic effects, and in some cases comparable values.

One parameter frequently used to characterize thermal motion is the diffusive exponent $\alpha(\tau)$ introduced in the previous section, and defined as:

$$\alpha(\tau) = \frac{\mathrm{d}\big(\log\langle \Delta x^2(\tau)\rangle\big)}{\mathrm{d}\big(\log\tau\big)} \ . \tag{3.33}$$

When directly computed from the estimate of mean-squared displacement of probes in a purely viscous fluid, one finds the apparent diffusive exponent:

$$\widehat{\alpha}(\tau) = \big[1 + \overline{\varepsilon}^2/(D\tau) - \sigma/(3\tau)\big]^{-1} \ . \tag{3.34}$$

Thus $\widehat{\alpha} < 1$ if $\overline{\varepsilon}^2/D > \sigma/3$, and an apparent subdiffusion is observed. On the other hand, $\widehat{\alpha} > 1$ if $\overline{\varepsilon}^2/D < \sigma/3$ and the particles exhibit an apparent superdiffusion in a purely viscous fluid. Fig. 3.9A

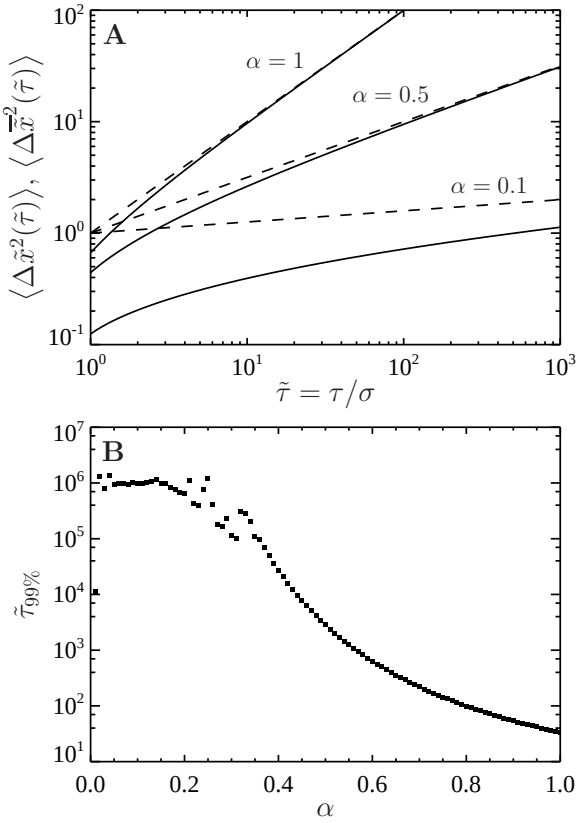

Fig. 3.8: Effect of the dynamic error on particles that exhibit a power-law mean-squared displacement. (A) Comparison of $\langle \Delta\bar{\tilde{x}}^2(\tilde{\tau})\rangle$ (*solid lines*) with the true $\langle \Delta\tilde{x}^2(\tilde{\tau})\rangle$ (*dashed lines*) for different values of α. Short lag time behavior is always superdiffusive. (B) Minimum lag time required to consider that the dynamic error has negligible effect. To solve $\langle \Delta\bar{\tilde{x}}^2(\tilde{\tau}_{99\%})\rangle = 0.99\langle \Delta\tilde{x}^2(\tilde{\tau}_{99\%})\rangle$, we use a globally-convergent Newton's method that becomes inefficient for $\alpha < 0.35$.

illustrates these two artifacts by showing experimentally measured mean-squared displacements in the two different regimes. Note that the results for 82% glycerol (*filled circles*) exhibit oscillations at short lag times. In this viscous fluid, particle displacements from one frame to the next are much smaller than 1 pxl. Thus, the offset between the position estimated in the odd and even field, as described in the previous section, becomes relevant. Furthermore, computation of the diffusive exponent from the mean-squared displacement is altered by these oscillations.

More striking are the errors arising in the rheological properties of the medium computed from the mean-squared displacement of the embedded particles. Using the generalized Stokes-Einstein equation, the complex shear modulus frequency spectrum $G^*(\omega) = G'(\omega)+iG''(\omega)$ can be evaluated

by [37]:

$$G^*(\omega) \approx \frac{k_\mathrm{B}T}{3\pi a} \frac{\exp\left[i\pi\alpha\left(1/\omega\right)/2\right]}{\left\langle \Delta x^2\left(1/\omega\right)\right\rangle \Gamma\left[1+\alpha\left(1/\omega\right)\right]} \ , \tag{3.35}$$

where Γ designates the gamma function. If $\alpha < 1$, the material exhibits a storage modulus $G'(\omega) \neq 0$. Thus when calculated from $\langle \Delta\widehat{\overline{x}}^2(\tau,\sigma)\rangle$ in the regime where $\widehat{\overline{\alpha}} < 1$, the shear modulus of glycerol has an apparent elastic component. We illustrate this effect in Fig. 3.9B. Furthermore, Fig. 3.9A shows a third regime where the two sources of error compensate: $\overline{\varepsilon}^2/D \sim \sigma/3$. These results suggest that more subtile mistakes can be made when interpreting the microrheology of complex fluids. Because dynamic error attenuates high-frequency elasticity, they can mask true subdiffusive behavior at short lag times and lead to an apparent diffusive mean-squared displacement. Several physical interpretations can arise from the observation of the mean-squared displacement, and it is thus essential to quantify the sources of errors to avoid any mistakes in one's line of reasoning.

Once the errors are quantified, corrections can be confidently made. The static error can be evaluated by fixing the particles on a substrate, and by performing measurements in similar noise and signal conditions as the rest of the experiments. The trivial subtraction of the measured static mean-squared displacement is validated, but not sufficient to recover the true mean-squared displacement. Further theoretical studies must be done to find ways to correct for the dynamic error. As stated earlier, corrections for this type of errors can be applied on the power spectral density of the position by using Eq. 3.7, and additionally on the mean-squared displacement if an analytic model describing its variation is available. However, this dynamic contribution can be reduced by ensuring $\sigma/\tau \ll 1$. Nevertheless, this criteria must be carefully verified for stiffer materials, as explained in earlier sections. As the exposure time is reduced, the collected illumination decreases, and thus the noise-to-signal ratio increases. Thus a compromise between reducing the dynamic error or the static error follows if non-averaged quantities are extracted. On the other hand, if the interest is focused on averaged properties, the shutter time should be decreased and correction for the static error should be performed. In this study, noise-to-signal ratios as high as 0.1 were examined. As $N/S = 1$ represents a fundamental limit, further studies should be performed in the range of N/S between 0.1 and 1 encountered in single molecule tracking. On the other hand, noise-to-signal ratio lower than 0.03 are difficult to achieve with standard video microscopy setup used for dynamic experiments at small shutter time. Thus, the spatial resolution in the tracks can not be lower than 10 nm ($\sim 5 \times 10^{-2}$ pxl), in accordance with results obtained in similar conditions by other groups [16, 15]. Also, we predict that the resolution of the mean-squared displacement can be reduced to values between 1 nm^2 and 10 nm^2 after corrections, limited only by statistics, accuracy in the estimation of $\overline{\varepsilon}$ and/or the position offset inherent to pixelization that were described earlier. However, further analysis should be performed to accurately evaluate this effective resolution, as the present study is limited to purely viscous fluids, for which the corrections are straightforward to apply.

We have used a video microscopy multiple particle tracking technique to perform the experiments. The methods employed here for noise measurements, as well as the relation between noise and spatial resolution are specific to this technique. However, static and dynamic errors from noise and finite exposure time are actually intrinsic to any particle tracking setup without restriction to the video microscopy based method. Also, the propagation formulas are valid for any dynamics, and should be considered even in active microrheology methods. For example, the spring constant of the trap created by optical tweezers is sometimes computed from the equilibrium mean-squared

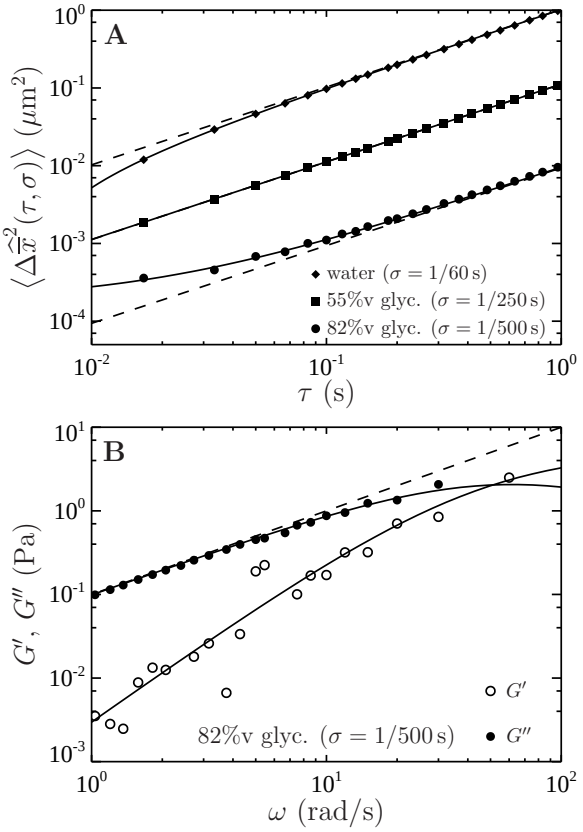

Fig. 3.9: Demonstration of how the errors in the mean-squared displacement can lead to spurious rheological properties. On both plots, solid lines are data computed from linear fit extracted from the mean-squared displacement at small lag times, and dashed lines are data obtained after applying corrections explained in the Discussion section. (A) Mean-squared displacements from three experiments. For an experiment in water with $\sigma = 1/60\,$s and $2D\sigma/3 > 2\bar{\varepsilon}^2$, an apparent superdiffusion can be observed. In 82% glycerol with $\sigma = 1/500\,$s and $2D\sigma/3 < 2\bar{\varepsilon}^2$, the mean-squared displacement exhibits apparent subdiffusion. The errors compensate one another, $2D\sigma/3 \sim 2\bar{\varepsilon}^2$, in 55% glycerol with $\sigma = 1/250\,$s. (B) Elastic and viscous moduli computed from the mean-squared displacement using the generalized Stokes-Einstein relation (Eq. 3.35). The apparent subdiffusion observed in 82% glycerol with $\sigma = 1/500\,$s leads to an apparent elastic behavior at high frequencies. The scatter in the experimental data comes from the inaccurate estimation of the diffusive exponent from the measured mean-squared displacement with a numerical differentiation using 3-point Lagrangian interpolation.

displacement of the trapped bead [58], and can be biased by these errors. Moreover, [59] already suggested that the amplitude of Brownian fluctuations can be underestimated when video detection

is used in optical tweezers experiments.

3.7 Conclusions

To conclude, we demonstrated that dynamic and static errors can cause great deviations in the experimental results obtained using particle tracking techniques. We provided procedures to both quantify and correct these errors. We show that standard video microscopy (using simply industrial grade cameras) can then be used to perform high resolution microrheology, and thus could become a primary choice for such experiments. Overall, our study brings to light the fact that great care must be taken in interpreting data obtained from particle tracking experiments.

CHAPTER 4

Dynamic Errors on Model Fluids

The role of a finite exposure time σ on measuring rheological properties using microrheology techniques has been presented in the previous chapter. In this chapter, we concentrate on studying the effect of this dynamic error on fluid models in which an embedded probe particle has a plateau in its mean-squared displacement. A analysis is performed to compare the resulting experimentally measured mean-squared displacement of the particle to its expected value in the fluid model. This chapter was reproduced in part with permission from Savin, T. and Doyle, P. S., *Phys. Rev. E*, **71**, 041106 (2005), copyright 2005 by the American Physical Society.

4.1 Introduction

As explained in previous chapters, passive microrheology uses thermally fluctuating micron-sized probes to determine local mechanical properties of a host medium [26]. In this class of techniques, time correlation of the particle position or displacement, through either the power spectral density $S^*_{\mathbf{x}}(\omega) = \langle |\mathbf{x}^*|^2(\omega) \rangle$ or the mean-squared displacement $\langle \Delta \mathbf{x}^2(t) \rangle = \langle [\mathbf{x}(\theta + t) - \mathbf{x}(\theta)]^2 \rangle$, is often calculated [34, 9]. Here $\mathbf{x}(t)$ is the particle position at time t, $\mathbf{x}^*(\omega)$ is its Fourier transform at the frequency ω, and the brackets $\langle \ldots \rangle$ indicate an ensemble average over a particle population and/or a time average over θ. Using a generalized Stokes expression for the drag applied on the particle by the medium (continuum assumption) and the fluctuation-dissipation theorem (thermal equilibrium assumption), these correlations can then be related to the shear modulus spectrum $G^*(\omega)$ of the material over a large frequency range [34, 37]. This range is limited in the high frequencies by the

fluid and/or the probe inertial effects (1 to 10 MHz in usual conditions), and in the low frequencies by the network compressibility (less than 1 Hz) [34, 38, 39]. The Brownian motion of a particle embedded in a complex fluid thus involves time scales from a variety of dynamical regimes, including the material viscoelastic relaxation modes.

Several techniques can be used to measure the particles position correlations (see Ref. [28] for a review). In the previous chapter, we outlined a general classification of the errors arising in these techniques. On the one hand, the noise in the detection scheme induces an error independent of the particle dynamics, and thus can be measured with a static particle and corrected on the averaged time correlations. On the other hand, the sampling method of the particle motions leads to an error that depends on the particle dynamics, and is challenging to correct. The latter error is referred to as "dynamic error" in the following study.

This chapter focuses on the role of a finite exposure time and the resulting dynamic-dependent errors when measuring an elastic modulus using microrheology techniques. The first section shows the general expression for the apparent mean-squared displacement resulting from the propagation of these errors on the true mean-squared displacement. The second part explores three model fluids exhibiting a purely elastic regime, for which the dynamic error can have a dramatic effect. In the third section we discuss implications of these results on microrheology measurements.

4.2 Dynamic Error

Experimentally, microrheology involves measuring particle displacements using some sort of detector (e.g. CCD for video microscopy or quadrant photodiode for laser deflection tracking). A single measurement requires a given exposure time σ during which the particle is continually moving. Thus, the position that is acquired at time t contains the history of the successive positions occupied by the particle during the time interval $[t-\sigma, t]$. We model this dynamic error by calculating the measured position as the average $\overline{\mathbf{x}}(t,\sigma)$ of all the positions the particle takes during the acquisition [51]:

$$\overline{\mathbf{x}}(t,\sigma) = \frac{1}{\sigma}\int_0^\sigma \mathbf{x}(t-\xi)\mathrm{d}\xi \ . \tag{4.1}$$

The finite sampling acts as a moving average low-pass linear filter [50]. To estimate $\langle \Delta\overline{\mathbf{x}}^2(t,\sigma)\rangle$, we use a method similar to that used in Ref. [60] and we write

$$\overline{\mathbf{x}}(\theta+t,\sigma) - \overline{\mathbf{x}}(\theta,\sigma) = \frac{1}{\sigma}\int_0^\sigma \mathrm{d}\xi' \int_\theta^{\theta+t} \mathrm{d}t'\, \mathbf{v}(t'-\xi') \ , \tag{4.2}$$

where $\mathbf{v}(t)$ is the true velocity of the particle. In terms of the velocity auto-correlation function $C_\mathbf{v}(|t''-t'|) = \langle \mathbf{v}(t')\cdot\mathbf{v}(t'')\rangle$, we find

$$\begin{aligned}
&\langle \Delta\overline{\mathbf{x}}^2(t,\sigma)\rangle = \left\langle \left[\overline{\mathbf{x}}(\theta+t,\sigma) - \overline{\mathbf{x}}(\theta,\sigma)\right]^2 \right\rangle \\
=&\frac{1}{\sigma^2}\int_0^\sigma \mathrm{d}\xi' \int_0^\sigma \mathrm{d}\xi'' \int_0^t \mathrm{d}t' \int_0^t \mathrm{d}t''\, C_\mathbf{v}\big(\big|(t'-\xi') - (t''-\xi'')\big|\big) \\
=&\frac{2}{\sigma^2}\int_0^\sigma \mathrm{d}\xi\, (\sigma-\xi)\int_0^t \mathrm{d}\theta\, (t-\theta)\Big[C_\mathbf{v}\big(\theta+\xi\big) + C_\mathbf{v}\big(|\theta-\xi|\big)\Big]
\end{aligned} \tag{4.3}$$

after multiple changes of variable and partial integrations. By comparing this expression to the similar expression obtained for the true mean-squared displacement [60]:

$$\langle \Delta \mathbf{x}^2(t) \rangle = 2 \int_0^t (t-\theta) C_{\mathbf{v}}(\theta) \mathrm{d}\theta \ , \tag{4.4}$$

we finally find, under the condition $t \geq \sigma$:

$$\langle \Delta \overline{\mathbf{x}}^2(t,\sigma) \rangle = \frac{1}{\sigma^2} \int_0^\sigma \Big[\langle \Delta \mathbf{x}^2(t+\xi) \rangle + \langle \Delta \mathbf{x}^2(t-\xi) \rangle - 2 \langle \Delta \mathbf{x}^2(\xi) \rangle \Big] (\sigma - \xi) \mathrm{d}\xi \ . \tag{4.5}$$

This relation is linear, but in general is difficult to invert.

We present in the next section three relevant examples for model viscoelastic fluids in which Brownian particles exhibit a known mean-squared displacement $\langle \Delta \mathbf{x}^2(t) \rangle$. These examples give specific insight into how the resulting measured mean-squared displacement $\langle \Delta \overline{\mathbf{x}}^2(t,\sigma) \rangle$ compares with the true mean-squared displacement $\langle \Delta \mathbf{x}^2(t) \rangle$.

4.3 Fluid Models

4.3.1 Power-Law Relaxation Model

We first consider a toy-model where the mean-squared displacement has the following form:

$$\frac{\langle \Delta \mathbf{x}^2(t) \rangle}{\langle \Delta \mathbf{x}_p^2 \rangle} = \begin{cases} (t/\tau)^\alpha & \text{if } t \leq \tau, \\ 1 & \text{if } t > \tau, \end{cases} \tag{4.6}$$

where $\langle \Delta \mathbf{x}_p^2 \rangle$ is the plateau value and τ is the characteristic time required to reach this plateau. The fluctuation-dissipation theorem and the generalized Stokes relation gives $\langle \Delta \mathbf{x}_p^2 \rangle = k_B T/(\pi a G)$, where a is the radius of the spherical particle, G is the elastic modulus of the medium and $k_B T$ is the Boltzmann temperature. The mean-squared displacement described by this model is qualitatively observed in many systems, though the sharp break introduced at $t = \tau$ is not physically realistic. This model allows us to consider on one hand the characteristic plateau onset time τ, as well as the nature of the particle dynamics through the exponent α.

For this model, we find that a plateau is reached for $t > \overline{\tau}(\sigma)$, where $\overline{\tau}(\sigma) = \tau + \sigma$ is the apparent relaxation time, and takes the following values:

$$\frac{\langle \Delta \overline{\mathbf{x}}_p^2(\sigma) \rangle}{\langle \Delta \mathbf{x}_p^2 \rangle} = \begin{cases} 1 - \dfrac{2(\sigma/\tau)^\alpha}{(1+\alpha)(2+\alpha)} & \text{if } \sigma \leq \tau, \\ \dfrac{\alpha}{(\sigma/\tau)^2} \left(\dfrac{2(\sigma/\tau)}{1+\alpha} - \dfrac{1}{2+\alpha} \right) & \text{if } \sigma > \tau. \end{cases} \tag{4.7}$$

One can also calculate the apparent short time power-law $\overline{\alpha}(t = \sigma, \sigma)$ where the local apparent power-law scaling is defined by

$$\overline{\alpha}(t,\sigma) = \frac{\mathrm{d}\big(\log \langle \Delta \overline{\mathbf{x}}^2(t,\sigma) \rangle\big)}{\mathrm{d}\big(\log t\big)} \ . \tag{4.8}$$

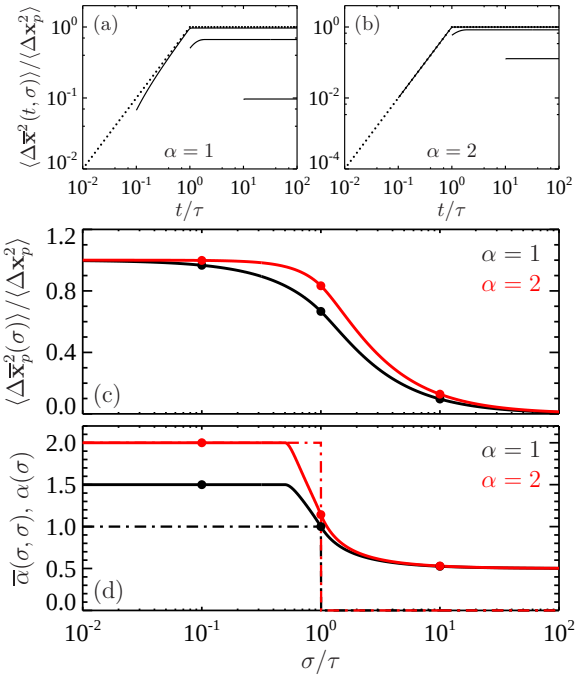

Fig. 4.1: Results for the power-law relaxation model. (a) and (b) are the exact mean-squared displacement (dotted lines) from Eq. (4.6) and its apparent values (solid lines) obtained from Eq. (4.5) with $\sigma/\tau = 0.1$, 1 and 10. (c) shows the apparent plateau values, as given by Eq. (4.7). The filled circles correspond to the three values of σ/τ used in (a) and (b). (d) is the short time power-law scaling (Eq. (4.8), solid lines) vs. σ/τ. The dashed-dotted lines are the values for the exact scaling $\alpha(t = \sigma)$.

We show in Fig. 4.1 the evolution of these quantities as a function of the acquisition time σ. Effects of the finite sampling become important for $\sigma \gtrsim \tau$. The apparent plateau value vanishes when $\sigma \gg \tau$ as shown in Fig 4.1(a). More dramatic is the effect of the sampling process on the short time power-law scaling (Fig. 4.1(d)). In general, the true scaling is not recovered in the apparent mean-squared displacement when $\sigma \lesssim t \ll \tau$ [1]. An exception to this is the ballistic case $\alpha = 2$ for which measured displacements are independent of σ, as shown by plugging a constant velocity $\mathbf{v}(t) = \mathbf{v}$ in Eq. (4.2).

[1] In Fig 4.1(d), one can not see $\overline{\alpha}(\sigma,\sigma) \to \alpha$ as $\sigma \to 0$. In that limit, both t and σ are tending to 0 together since we set $t = \sigma$. One can show however that $\overline{\alpha}(t,\sigma) = \alpha(t) + \mathcal{O}(\sigma/t)^\nu$ whith $\nu > 0$.

4.3.2 Voigt Fluid Model

The shear modulus spectrum of the Voigt fluid viscoelastic model is given by

$$G^*(\omega) = G(1 + i\omega\tau_v) \tag{4.9}$$

where G is the elastic modulus and τ_v is the relaxation time. The equation governing the particle dynamics for this model is then given by

$$\tau_v\tau_b\ddot{\mathbf{x}}(t) + \tau_v\dot{\mathbf{x}}(t) + \mathbf{x}(t) = \mathbf{f}(t)/(6\pi aG) \tag{4.10}$$

where $\tau_b = m/(6\pi aG\tau_v)$ is the Brownian time (m being the mass of the particle), and $\mathbf{f}(t)$ is the Brownian force [61]. By taking the Fourier Transform on both sides of Eq. (4.10), we can calculate the power spectral density of the position by

$$S^*_{\mathbf{x}}(\omega) = \big\langle |\mathbf{x}^*|^2(\omega)\big\rangle = \frac{\tau_v k_B T/(\pi aG)}{(1+\tau_+^2\omega^2)(1+\tau_-^2\omega^2)} \ , \tag{4.11}$$

where we have introduced the relaxation times

$$\tau_\pm = \frac{\tau_v}{2}\big(1 \pm \sqrt{1 - 4\tau_b/\tau_v}\big) \ , \tag{4.12}$$

that can be complex numbers in the under-damped case $4\tau_b > \tau_v$. To write Eq. (4.11), we have also used the fluctuation-dissipation theorem $S^*_{\mathbf{f}}(\omega) = \langle|\mathbf{f}^*|^2(\omega)\rangle = 36\pi aG\tau_v k_B T$. The inverse Fourier transform of $S^*_{\mathbf{x}}(\omega)$ gives the position auto-correlation function $C_{\mathbf{x}}(t)$ and we use the relation $\langle\Delta\mathbf{x}^2(t)\rangle = 2C_{\mathbf{x}}(0) - 2C_{\mathbf{x}}(t)$ to find:

$$\frac{\langle\Delta\mathbf{x}^2(t)\rangle}{\langle\Delta\mathbf{x}_p^2\rangle} = \frac{\tau_+\big(1-e^{-|t|/\tau_+}\big) - \tau_-\big(1-e^{-|t|/\tau_-}\big)}{\tau_+ - \tau_-} \ . \tag{4.13}$$

For the over-damped regime $4\tau_b/\tau_v \ll 1$, shown in Fig. 4.2(a), a plateau region is obtained for $t \gg \tau_v$. However, for the under-damped limit $4\tau_b/\tau_v \gg 1$, plot in Fig. 4.2(b), the plateau is reached for $t \gg \sqrt{\tau_b\tau_v}$ and the mean-squared displacement exhibits oscillations around the plateau value with a period of $\sim 2\pi\sqrt{\tau_b\tau_v}$.

Using Eq. (4.5), we can calculate the apparent mean-squared displacement $\langle\Delta\overline{\mathbf{x}}^2(t,\sigma)\rangle$ and obtain the plateau value by letting $t \gg \max\big(\tau_v, \sqrt{\tau_b\tau_v}\big)$:

$$\frac{\langle\Delta\overline{\mathbf{x}}_p^2(\sigma)\rangle}{\langle\Delta\mathbf{x}_p^2\rangle} = \frac{\tau_+ + \tau_-}{\sigma/2} - \frac{\tau_+^3\big(1-e^{-\sigma/\tau_+}\big) - \tau_-^3\big(1-e^{-\sigma/\tau_-}\big)}{\sigma^2(\tau_+ - \tau_-)/2} \ . \tag{4.14}$$

We first consider the over-damped limit. In that case, the characteristic time scale is τ_v and Eq. (4.14) simplifies to

$$\frac{\langle\Delta\overline{\mathbf{x}}_p^2(\sigma)\rangle}{\langle\Delta\mathbf{x}_p^2\rangle} = \frac{\tau_v}{\sigma/2} - \frac{1-e^{-\sigma/\tau_v}}{(\sigma/\tau_v)^2/2} + \mathcal{O}(\tau_b/\tau_v) \tag{4.15}$$

as obtained by keeping σ/τ_v finite and $\tau_b/\tau_v \to 0$.

It is interesting to consider the under-damped regime of the Voigt model since we will show it is similar to the short time behavior of the Maxwell model in the next section. The apparent plateau

value is obtained by keeping $\sigma/\sqrt{\tau_b\tau_v}$ finite and $\tau_v/\tau_b \to 0$:

$$\frac{\langle \Delta\overline{\mathbf{x}}_p^2(\sigma)\rangle}{\langle \Delta\mathbf{x}_p^2\rangle} = \mathrm{sinc}^2\left(\frac{\sigma}{2\sqrt{\tau_b\tau_v}}\right) + \mathcal{O}(\tau_v/\tau_b)^{1/2} \tag{4.16}$$

where $\mathrm{sinc}(x) = \sin(x)/x$ is the sine cardinal function. Note that the same results would have been obtained if the following approximated mean-squared displacement were plugged into Eq. (4.5):

$$\frac{\langle \Delta\mathbf{x}^2(t)\rangle}{\langle \Delta\mathbf{x}_p^2\rangle} = \begin{cases} 1 - e^{-t/\tau_v} & +\mathcal{O}(\tau_b/\tau_v)\ , \\ 1 - \cos\big(t/\sqrt{\tau_b\tau_v}\big) & +\mathcal{O}(\tau_v/\tau_b)^{1/2}\ , \end{cases} \tag{4.17}$$

by respectively keeping t/τ_v or $t/\sqrt{\tau_b\tau_v}$ finite. In particular, the apparent mean-squared displacement in the inertialess limit $\tau_b/\tau_v = 0$ is found to be:

$$\frac{\langle \Delta\overline{\mathbf{x}}^2(t,\sigma)\rangle}{\langle \Delta\mathbf{x}_p^2\rangle} = \epsilon_\sigma\big(1 - \beta_\sigma e^{-t/\tau_v}\big)\ , \tag{4.18}$$

with

$$\epsilon_\sigma = \frac{\langle \Delta\overline{\mathbf{x}}_p^2(\sigma)\rangle}{\langle \Delta\mathbf{x}_p^2\rangle} = \frac{\tau_v}{\sigma/2} - \frac{1 - e^{-\sigma/\tau_v}}{(\sigma/\tau_v)^2/2}\ , \tag{4.19}$$

$$\beta_\sigma = 1 - \frac{\sinh(\sigma/\tau_v) - \sigma/\tau_v}{1 - e^{-\sigma/\tau_v} - \sigma/\tau_v}\ . \tag{4.20}$$

Similar to the power-law relaxation model, the plateau value shown in Fig. 4.2(c) is greatly modified by the finite sampling for σ greater than the characteristic plateau onset time. In the underdamped case the plateau is reached through oscillations and its apparent value is non-monotonically decreasing with increasing acquisition time (cf. the colored line in Fig. 4.2(c)).

4.3.3 Maxwell Fluid Model

In the single relaxation time Maxwell fluid viscoelastic model, the shear modulus spectrum is given by

$$G^*(\omega) = G\frac{i\omega\tau_m}{1 + i\omega\tau_m} \tag{4.21}$$

where G is the elastic modulus and τ_m is the relaxation time. The equation governing the particle dynamics for this model is then

$$\tau_m\tau_b\ddot{\mathbf{v}}(t) + \tau_b\dot{\mathbf{v}}(t) + \mathbf{v}(t) = \mathbf{f}(t)/(6\pi aG\tau_m) \tag{4.22}$$

where $\mathbf{v}(t) = \dot{\mathbf{x}}(t)$ is the velocity of the particle [61]. By taking the Fourier Transform on both sides of Eq. (4.22), we can calculate the power spectral density of the velocity by

$$S_{\mathbf{v}}^*(\omega) = \big\langle |\mathbf{v}^*|^2(\omega)\big\rangle = \frac{k_BT/(\pi aG\tau_m)}{(1 + \tau_+^2\omega^2)(1 + \tau_-^2\omega^2)} \tag{4.23}$$

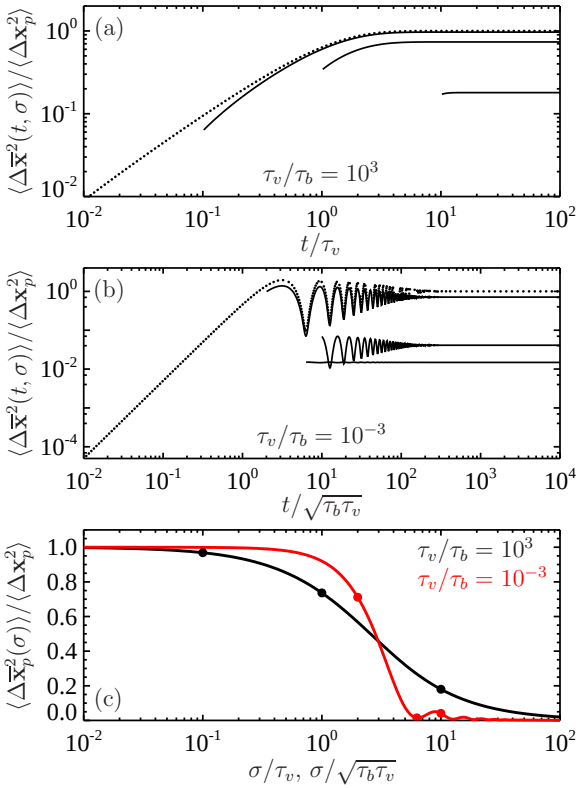

Fig. 4.2: Results for the Voigt fluid model. (a) and (b) are the exact mean-squared displacement (dotted lines) from Eq. (4.13) and its apparent value (solid lines) obtained from Eq. (4.5) with $\sigma/\tau_v = 0.1$, 1, 10 in (a), and $\sigma/\sqrt{\tau_b\tau_v} = 2$, 2π, 10 in (b). (c) shows the apparent plateau values, as given by Eq. (4.14). The filled circles on each line denote the values of σ used in (a) and (b).

where we have introduced the complex relaxation time

$$\tau_\pm = \frac{\tau_b}{2}\left(1 \pm i\sqrt{4\tau_m/\tau_b - 1}\right) \tag{4.24}$$

and we have used the fluctuation-dissipation theorem $S^*_{\mathbf{f}}(\omega) = 36\pi a G \tau_m k_B T$. The inverse Fourier transform of $S^*_{\mathbf{v}}(\omega)$ returns the velocity auto-correlation function $C_{\mathbf{v}}(t)$ and the use of Eq. (4.4) gives finally[2]:

$$\frac{\langle \Delta\mathbf{x}^2(t)\rangle}{\langle \Delta\mathbf{x}_p^2\rangle} = \frac{|t|}{\tau_+} + \frac{|t|}{\tau_-} - \frac{\tau_+^3\left(1-e^{-|t|/\tau_+}\right) - \tau_-^3\left(1-e^{-|t|/\tau_-}\right)}{\tau_+\tau_-(\tau_+ - \tau_-)}\ . \tag{4.25}$$

[2]Note that the plateau scaled value obtained from Eq. (4.25) is $1 - \tau_b/\tau_m$.

We investigate only the physically realistic regime where $\tau_m/\tau_b \gg 1$.

For the Maxwell Model, a plateau region is obtained for $\sqrt{\tau_b\tau_m} < t < \tau_m$ and its apparent value is found to be

$$\begin{aligned}\frac{\langle\Delta\overline{\mathbf{x}}_p^2(\sigma)\rangle}{\langle\Delta\mathbf{x}_p^2\rangle} &= \lim_{t/\sqrt{\tau_b\tau_m}\to\infty}\left[\frac{\langle\Delta\overline{\mathbf{x}}^2(t,\sigma)\rangle}{\langle\Delta\mathbf{x}_p^2\rangle} - \frac{t}{\tau_+} - \frac{t}{\tau_-}\right] \\ &= \frac{\tau_+^5\big(1-e^{-\sigma/\tau_+}\big) - \tau_-^5\big(1-e^{-\sigma/\tau_-}\big)}{\sigma^2\tau_+\tau_-(\tau_+-\tau_-)/2} \\ &\quad - \frac{\tau_+ + \tau_-}{\sigma/2} - \frac{\tau_+^3+\tau_-^3}{\sigma\tau_+\tau_-/2} - \frac{\sigma}{3\tau_+} - \frac{\sigma}{3\tau_-}\ .\end{aligned} \tag{4.26}$$

For $2\pi\sqrt{\tau_b\tau_m} < \sigma \le t$, the sampling rate is not high enough to detect the oscillations in the mean-squared displacement, and we introduce the following approximation[3]:

$$\frac{\langle\Delta\overline{\mathbf{x}}^2(t,\sigma)\rangle}{\langle\Delta\mathbf{x}_p^2\rangle} \approx \epsilon_\sigma\left(\frac{t}{\tau_m\epsilon_\sigma}+1\right)\ , \tag{4.27}$$

with $\epsilon_\sigma = \langle\Delta\overline{\mathbf{x}}_p^2(\sigma)\rangle/\langle\Delta\mathbf{x}_p^2\rangle$ and obtained by discarding oscillatory terms in $\langle\Delta\overline{\mathbf{x}}^2(t,\sigma)\rangle$. Eq (4.27) also shows that the apparent Maxwell relaxation time is

$$\overline{\tau}_m(\sigma) = \tau_m\epsilon_\sigma\ . \tag{4.28}$$

Next, we calculate the limiting behavior of Eq. (4.26) as $\tau_b/\tau_m \to 0$. By keeping $\sigma/\sqrt{\tau_b\tau_m}$ finite, we obtain:

$$\frac{\langle\Delta\overline{\mathbf{x}}_p^2(\sigma)\rangle}{\langle\Delta\mathbf{x}_p^2\rangle} = \mathrm{sinc}^2\left(\frac{\sigma}{2\sqrt{\tau_b\tau_m}}\right) + \mathcal{O}\big(\tau_b/\tau_m\big)^{1/2}\ , \tag{4.29}$$

whereas by keeping σ/τ_m finite, we find[4]:

$$\frac{\langle\Delta\overline{\mathbf{x}}_p^2(\sigma)\rangle}{\langle\Delta\mathbf{x}_p^2\rangle} = -\frac{\sigma}{3\tau_m} + \mathcal{O}\big(\tau_b/\tau_m\big)\ . \tag{4.30}$$

It is interesting to note the close resemblance of Eq. (4.16) to Eq. (4.29). This point will be discussed in the next section.

The inertialess regime is a peculiar limit where

$$\langle\Delta\overline{\mathbf{x}}^2(t,\sigma)\rangle = \frac{\langle\Delta\mathbf{x}_p^2\rangle}{\tau_m}\big(t-\sigma/3\big) \tag{4.31}$$

is similar to the purely viscous model, for which $\langle\Delta\overline{\mathbf{x}}^2(t,\sigma)\rangle = 6D\big(t-\sigma/3\big)$ where D is the self-diffusion coefficient of the particle. Note that this result is obtained for any finite value of σ/τ_m, so that the Maxwell relaxation time is not measurable even if $\sigma \ll \tau_m$.

[3] We use $1/\tau_+ + 1/\tau_- = 1/\tau_m$. Note that this approximation returns the inertialess limit for $\sigma = 0$: $\langle\Delta\overline{\mathbf{x}}^2(t,\sigma=0)\rangle/\langle\Delta\mathbf{x}_p^2\rangle \approx t/\tau_m + 1$.

[4] The minus sign in Eq. (4.30) for a mean-squared displacement plateau value indicates an negative intercept at $t = 0$ that is actually never reached for $t \ge \sigma$. This peculiarity is due to the notations and denominations used here but is not a mathematical flaw.

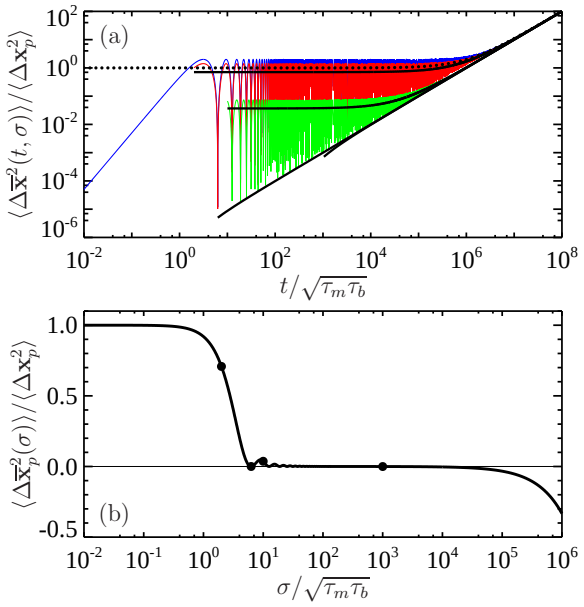

Fig. 4.3: Results for the Maxwell fluid model, with $\tau_m/\tau_b = 10^{12}$ (motivation for this value is given in the Discussion section). (a) gives the true mean-squared displacement (dotted line) and its apparent value (solid lines) for $\sigma/\sqrt{\tau_b\tau_m} = 2$, 2π, 10 and 10^3. The dotted and thick lines are obtained with Eq. (4.27) whereas the thin curves result from exact calculations using Eqs. (4.5) and (4.25). (b) shows the apparent plateau values as given by Eq. (4.26). The filled circles denote the values of σ used in (a).

Figure 4.3 shows the results for the single relaxation time Maxwell model, with $\tau_m/\tau_b = 10^{12}$ as found in experimental studies (see the Discussion section). Note in Fig. 4.3(a) that the mean-squared displacement oscillations, with period $\sim 2\pi\sqrt{\tau_b\tau_m}$, can not be distinguished for $t > \sigma > 2\pi\sqrt{\tau_b\tau_m}$.

4.4 Discussion

Using a relatively simple model for the dynamic error, we can quantify the effect of the acquisition time on the mean-squared displacement of thermally fluctuating particles in a complex medium. Moreover, most of the trends of the Voigt and Maxwell models are captured with the simple power-law relaxation model.

The complex shear modulus spectrum $G^*(\omega)$ can be evaluated using the generalized Stokes-Einstein relation obtained in the inertialess limit [9, 37]:

$$\widetilde{G}(s) = \frac{k_B T}{s\pi a \langle \Delta\widetilde{\mathbf{x}}^2(s)\rangle} \quad \text{with} \quad G^*(\omega) = \widetilde{G}(i\omega)\ , \tag{4.32}$$

where $\widetilde{G}(s)$ and $\langle \Delta \widetilde{\mathbf{x}}^2(s) \rangle$ are the Laplace transform of the shear modulus and of the mean-squared displacement, s being the Laplace frequency.

For the Voigt model, we can use the inertialess limit Eq. (4.18) for the mean-squared displacement to find

$$\overline{G^*}(\omega, \sigma) = \frac{G}{\epsilon_\sigma} \frac{1 + i\omega\tau_v}{1 + i\omega\tau_v(1 - \beta_\sigma)} \ . \tag{4.33}$$

Using approximation of Eq. (4.27) for the Maxwell model, we find

$$\overline{G^*}(\omega, \sigma) = \frac{G}{\epsilon_\sigma} \frac{i\omega\tau_m\epsilon_\sigma}{1 + i\omega\tau_m\epsilon_\sigma} \ . \tag{4.34}$$

These apparent shear modulus spectrum are compared to the exact expressions Eqs. (4.9) and (4.21) in Fig. 4.4.

To evaluate the error ϵ_σ, one must compare the acquisition time σ to the onset time of the plateau. In the Maxwell model and the under-damped Voigt model, the ballistic regime observed before the plateau is extended to an onset time $\sqrt{\tau_b\tau_m}$ and $\sqrt{\tau_b\tau_v}$ respectively. These time scales can be understood with a simple picture. In the elastic regime, the particle moves in a harmonic well $U(x) = kx^2$, with $k = 6\pi aG$ and where G is the elastic modulus of either the Voigt or the Maxwell fluid. Since the particle equilibrium energy is k_BT, it moves in a range $x = \pm\sqrt{k_BT/k}$. The time required to sample this range at the equilibrium velocity $\sqrt{k_BT/m}$ is then $\sqrt{m/k}$, equal to respectively $\sqrt{\tau_b\tau_v}$ or $\sqrt{\tau_b\tau_m}$ in the Voigt or the Maxwell model.

This simple picture of a particle in a harmonic potential well helps to understand the effect of the sampling and the common trends observed for the apparent plateau values as σ increases. In a time interval of length τ, the particle has sampled all possible positions in the potential well. Thus, when averaged over a time interval $\sigma > \tau$, its apparent position remains constant equal to the potential center, and the apparent mean-squared displacement tends to 0.

Few microrheology experiments have been performed on single relaxation time fluid models. In a study by van Zanten and co-workers [57], measurements where performed on CTAB/Kbr wormlike micelle aqueous solution using diffusing wave spectroscopy with $2a \approx 1\,\mu$m diameter polystyrene beads for probe particles. This technique provides a high temporal resolution of $\sigma \approx 10^{-6}\,$s limited by the sampling frequency of the multiple-tau digital correlator as used for lag times larger than $\sim 1\,\mu$s [62]. Under the conditions they used[5], both rheological and microrheological measurements show a single relaxation time Maxwellian behavior of the solution. From their data we find $\sigma/\sqrt{\tau_b\tau_m} \approx 10$ and $\tau_m/\tau_b \approx 10^{12}$. For these values, the use of Eq. (4.26) shows that the apparent plateau is less than 5% of the true values, which corresponds to a factor of 20 for the error in the estimated elastic modulus G (see Fig. 4.4). However, the plateau moduli estimated by van Zanten and co-workers are in good agreement with rheological measurement [57]. Another plateau onset time $\tau_e > \sigma$ is involved in the dynamics. They suggest that for $t < \tau_e$ the particle's dynamics is driven by the Rouse behavior of the wormlike micelles, that is $\langle \Delta\mathbf{x}^2(t) \rangle \propto t^{1/2}$ [63]. We

[5] At the concentration used ([CTAB] $\approx 0.3\,$M and [KBr] $\approx 1\,$M) and at $T \approx 35\,^\circ$C, the solution is Maxwellian in the vicinity of a relaxation time $\tau_m \approx 0.1\,$s with a high frequency elastic plateau at $G \approx 1000\,$Pa. The Brownian time can be calculated with $\tau_b = 2a^2\rho/(9G\tau_m) \approx 10^{-13}\,$s, where $\rho \approx 1000\,$kg/m^3 is the particle density.

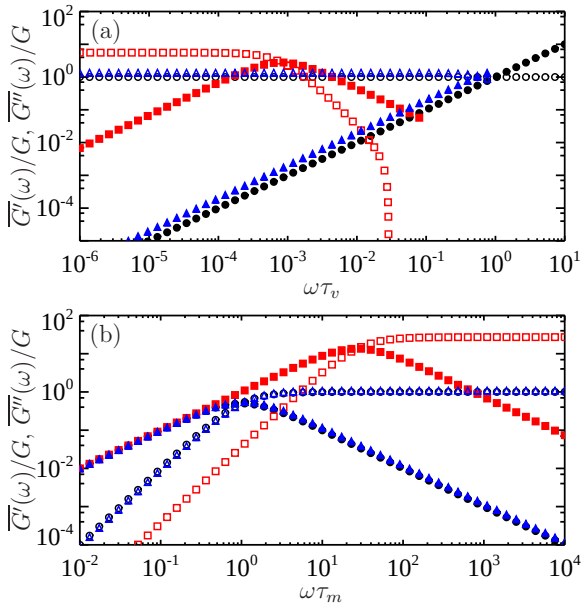

Fig. 4.4: Apparent shear modulus spectrum for the Voigt model (a) and the Maxwell model (b) obtained from Eqs. (4.33) and (4.34) respectively. The open symbols show the apparent storage modulus $\overline{G'}$ (real part of $\overline{G^*}$) and the filled symbols give the loss modulus $\overline{G''}$ (imaginary part of $\overline{G^*}$). Circles are the exact values (from Eqs. (4.9) in (a) and (4.21) in (b)). The triangles and squares are the apparent values with σ being respectively equal to the plateau onset time ($\sigma = \tau_v$ in (a) and $\sigma = \sqrt{\tau_b \tau_m}$ in (b)) and 10 times the plateau onset time ($\sigma = 10\tau_v$ in (a) and $\sigma = 10\sqrt{\tau_b \tau_m}$ in (b)). We took $\tau_m/\tau_b = 10^{12}$ for (b).

can modify our power-law relaxation model to take the Maxwell behavior into account by setting

$$\frac{\langle \Delta \mathbf{x}^2(t) \rangle}{\langle \Delta \mathbf{x}_p^2 \rangle} = \begin{cases} (t/\tau_e)^{1/2} & \text{if } t \leq \tau_e \ , \\ (t-\tau_e)/\tau_m + 1 & \text{if } t > \tau_e \ . \end{cases} \tag{4.35}$$

If we take $\tau_e/\tau_m = 10^{-3}$ and $\sigma/\tau_m = 10^{-5}$, we find that the dynamic error diminishes the plateau value by only 5%.

It is instructive to consider the dynamic error arising in the same experimental system when studied by the commonly employed technique of video microscopy [28, 39]. Standard video microscopy uses an industrial grade CCD camera for signal detection with usually $\sigma \approx 10^{-3}\,\mathrm{s}$. If the experimental Maxwell model fluid described here was studied with video microscopy (then $\sigma/\tau_m \approx 10^{-2}$ and $\sigma/\tau_e \approx 10$), we predict that the dynamic error will lead to a great discrepancy between the microrheology measurements and the bulk rheology (Fig. 4.4). This dramatic comparison reinforces the need to understand the dynamic error when performing microrheology using

different setups.

4.5 Conclusions

We investigated the effect of a finite exposure time on microrheology measurements of fluids in which an embedded particle's mean squared displacement displays a plateau above an onset time τ. Using common viscoelastic models, we find that the sampling rate σ^{-1} has a great effect on the measured shear modulus. In particular, the latter exhibits apparent magnitudes that greatly differ from the expected value when σ is larger then τ and our calculations allow us to quantify these effects. In general, at frequencies $\omega \lesssim \sigma^{-1}$, extracted scalings and analysis should be performed with great care.

CHAPTER 5

Statistics of Multiple Particle Tracking Measurements

In the previous chapter, we have presented an important limitation of the video microscopy particle tracking technique. We have shown that the detector intrinsic noise and acquisition process induce errors in the localization of the particles. These errors propagate on the mean-squared displacement, the classical calculation performed for microrheology measurements, and lead to inaccuracies that are usually greater at short lag times, hence at high frequencies. In chapter 2, we have already mentioned that another limitation was coming from the finiteness of the volume of observation, especially in the z direction. This leads to a certain statistical peculiarity, in particular in heterogeneous materials, that is discussed in this chapter. Here we will characterize in detail the statistical uncertainty (mainly a low frequencies issue), and we will demonstrate a valid measure of material heterogeneity from the output of multiple particle tracking.

5.1 Introduction

The interest in resolving the structure of complex fluids at a micron size length scale has increased with the advent of soft matter sciences. This interest is justified by the implication of the spatial micro organization of the components of a complex material in its transport, rheological, optical properties at equilibrium (see [64] and references therein), as well as in its eventual kinetics of formation [65, 66]. This microscale characterization has also been shown to be particularly important in biological applications. From inter- and intracellular transport phenomena to molecular motors

activity, the driving (or resisting) forces occur on micron and submicron length scales, which can not be inferred from bulk measurements [67, 68]. Also in the biology framework, it has been reported that the fate and behavior of single cells depends on their local level of confinement [69] or the stiffness of their microenvironment [70]. More strikingly, it has been recently pointed out that in general, systems with heterogeneous features can lead to apparent peculiar measurements, themselves leading to incorrect interpretation [71]. Thus, access to some measure of the spatial distribution of a given material property (pore size, visco-elasticity, charges density ...) provides a fundamental information for the understanding of a plethora of phenomena involved in complex fluids science.

Consequently, the range of techniques available to achieve these goals has been broaden over the last decades. Direct observations of the structural elements and their organization are made possible thanks to a wide range of microscopy techniques. Light, fluorescence, electron and atomic force microscopy are able to report a spatial mapping of the complex fluid structure at various length scales, by usually providing with contrasted two-dimensional pictures. Eventually high order measure of the spatial distribution of structures can be made by using image postprocessing techniques from these images [72, 73]. Three dimensional information can be obtained from elaborated versions of the previous techniques (confocal, differential interference contrast, quick freeze/deep etch sample preparation for electron microscopy,...). Scattering techniques such as neutron, x-ray and light scattering however spatially average the structural features in the sample and thus lose some information on the eventual heterogeneity.

Rheology on a complex fluid is intimately related to its network microstructure [74]. Beside the morphological measurements described above, inferring structural information from rheological data is however a complicated inverse problem (see for example [75] for an application of rheological data to extract information on the network heterogeneity). Direct microrheological mapping of material has been addressed recently [11, 12]. Microrheology measures the response of a material to micron-sized probes motions. Under certain conditions, it reports either the local mechanical property or the microstructure of the material in which the probes are embedded (see chapter 1). Video multiple particle tracking is a simple and inexpensive microrheology technique that, to date, provides the highest throughput of spatial microrheological sampling of a material. It is a passive technique where the thermal fluctuations of hundred of particle dispersed in the material can be tracked simultaneously (see chapter 2 for a detailed description of the technique). Measurements are usually fast and the statistical errors are usually considered small because of the large amount of data collected. The spatial resolution of this technique was discussed in previous chapters, and the temporal resolution is essentially determined by the video rate. Its simplicity and availability has made it very popular, and in the last few years, investigation of microenvironment using video multiple particle tracking has been performed on actin systems, agarose gels, cells, DNA solutions [76, 10, 77, 78]. In recent studies, it has been used to extract pore sizes distribution in cross-linked actin networks [79] and to characterize anisotropic gels of aligned DNA [80]. We can also recall at this point that the materials heterogeneity can be a problem for microrheologists trying to calculate bulk properties. A recent method that overcomes such problems has recently been introduced using the cross-correlation of paired probes motion [81, 82].

It remains that a lot of the complex materials investigated with microrheology are known to be heterogeneous, such that depending on where the probe is located in the sample, its motion will exhibit different dynamics. In parallel, due to the finite imaging volume, the amount of data collected from a given particle is limited by the duration of its residence in the volume of observation.

The complexity comes from the fact that the duration of the measured particle trajectory depends also on the local material property. For example a heterogeneous system can let some particles travel throughout a porous structure, but will tightly trap a subpopulation of particles in its smaller pores (such behavior has been recently observed in actin gels [46]). The trapped particle will be tracked for the whole acquisition time, whereas free particles will leave the volume of observation and/or enter -possibly several times- during the same acquisition time. As a result, numerous short trajectories will be extracted in region of loose meshing where particles are free to move, whereas only a few long trajectories will be extracted from the signal of trapped particles, even if the material hypothetically exhibit the same amount of small and large pores. This example gives an immediate sense of the peculiar statistical sampling of a heterogeneous material using this technique. This sampling depends on both the size of the imaging volume and the probed material's structure.

Ultimately, the distribution of material property needs to be characterized independently of the measurement technique. The distribution of property can be quantified by its mean, variance, skewness, kurtosis and other higher order moments or functions of moments such as the non-gaussian parameters [83]. The latter have already been used to quantify dynamical heterogeneity in colloidal systems [84, 85]. Through the dynamics of the probes, the material heterogeneity is indirectly, but almost uniquely, quantified (see subsequent sections). For example, the mean of the probes individual mean-squared displacements, that is the ensemble averaged mean-squared displacement, is usually calculated by dividing in time individual trajectories into displacements and accounting for all displacements the same way, disregarding the trajectory they were extracting from (a simultaneous time and ensemble average is thus performed). But it has also been calculated as the center of individual mean-squared displacement distribution obtained from prior time averaging calculations on the individual trajectories [86]. Similar "naive" calculations based on time-averaged estimation from each probes trajectory were used in [11, 29] to perform qualitative analysis that circumvent the statistical limitations described in the previous paragraph. We only found two methods in the literature. In a first kind of heterogeneity study, bin partitions analysis based on a percentile calculations is used to increase statistics [65, 78, 77, 43, 66]. This analysis remains overall a qualitative perspective since it compares results in complex systems with measurement in homogenous glycerol solutions. It has however the advantage of being able to provide a somewhat quantitative degree of heterogeneity. In a second attempt, hypothesis testing based on the F-ratio of paired mean-squared displacement were performed to classify particles dynamics into statistically undistinguishable groups [12]. Although it is not the more convenient way to quantify the heterogeneity (i.e. with a single number), this classification allowed them to map the locations of given micro environment in an agarose gel sample. Following this idea, it is actually possible to test homogeneity of multiple dynamics with a single statistics (see [87] for a review of available statistical tests), and to eventually conclude on the heterogeneity of a sample.

In this chapter, we develop a way to rigorously calculate the first two moments of the probe particle dynamics in a heterogeneous system. Using a mathematical formulation for the peculiar statistical sampling obtained in multiple particle tracking output, we derive estimators of these two moments (mean and variance) that are independent of the sampling design, up to a certain fundamental limitation of the technique that we called transparency. In the first part, the theoretical approach is exposed and an important factor quantifying the level of transparency of the technique to certain probes dynamic is introduced. From this, estimators for the two first moments of individual mean-squared displacements are derived. The last part provides stringent testing of

these estimators on simulated and experimental systems of increasing complexity, that cover a wide range of actual scenarios.

5.2 Notations

Δt :	sampling time
T_b :	duration of the acquisition
n_b :	duration of the acquisition in Δt units (i.e. $T_\mathrm{b}/\Delta t$)
V_b :	volume of observation
C_b :	density of particle dispersed in the material
$N_\mathrm{b}(t)$:	number of particles in V_b at a time t
t_i :	first time of observation of trajectory i
T_i :	duration of the trajectory i
n_i :	duration of the trajectory i in Δt units (i.e. $T_i/\Delta t$)
τ :	lag time
n :	lag time in Δt units (i.e. $\tau/\Delta t$)
$I(n)$:	set of indices corresponding to trajectories longer than τ (i.e. $\{i : n_i \geq n\}$)
$x_{i,j}$:	j-th time-ordered observed position on the trajectory i
$d_{i,j}(n)$:	j-th time-ordered displacement extracted at time τ from trajectory i
$q_i(n)$:	number of *overlapping* displacements extracted at time τ from trajectory i
$q_i(n)$:	number of *overlapping* displacements extracted at time τ from trajectory i
$D(n)$:	set of overlapping displacements (i.e. $D(n) = \{\{d_{i,j}(n)\}_{1\leq j\leq q_i(n)}\}_{i\in I(n)}$)
$m_i(\tau)$:	ensemble mean squared displacement of trajectory i at lag time τ
s_i :	size of the block on trajectory i used to perform block-average transform
$\underline{d_r}_{i,j}(\tau)$:	j-th time-ordered block-averaged r-th power displacement extracted at time τ from trajectory i
$\underline{q}_i(\tau)$:	number of block-averaged displacement from trajectory i
$\underline{D_r}(n)$:	set of block-averaged displacements (i.e. $\underline{D_r}(n) = \{\{\underline{d_r}_{i,j}(n)\}_{1\leq j\leq \underline{q}_i(n)}\}_{i\in I(n)}$)

5.3 Theory

5.3.1 Sampling Design of Multiple Particle Tracking

Let $\nu(\omega, \mathbf{r})$ be the value of a material property ν at the location $\mathbf{r} \in V$ in the material, evaluated at the frequency ω. We write $P_{\nu(\omega)}(v) = V^{-1}\int_V \delta[v - \nu(\omega, \boldsymbol{\rho})]\mathrm{d}\boldsymbol{\rho}$ the probability density function of this material property in a volume V of medium. A schematic of such a heterogeneous fluid is pictured in figure 5.1. An indicator of heterogeneity of the material in this volume is then given by the mean $\mathbb{E}[\nu(\omega)]$ and the moments about the mean of $P_{\nu(\omega)}$: $\mu_r[\nu(\omega)] = \mathbb{E}\big[(\nu(\omega) - \mathbb{E}[\nu(\omega)])^r\big]$, where $\mathbb{E}[\dots]$ designates the expectation value.

In a passive microrheology experiment such as the multiple particle tracking technique described in chapter 2, a measure of the local material property is made through the thermal motion of a micron-sized particle embedded in the material. A thermally fluctuating particle following the

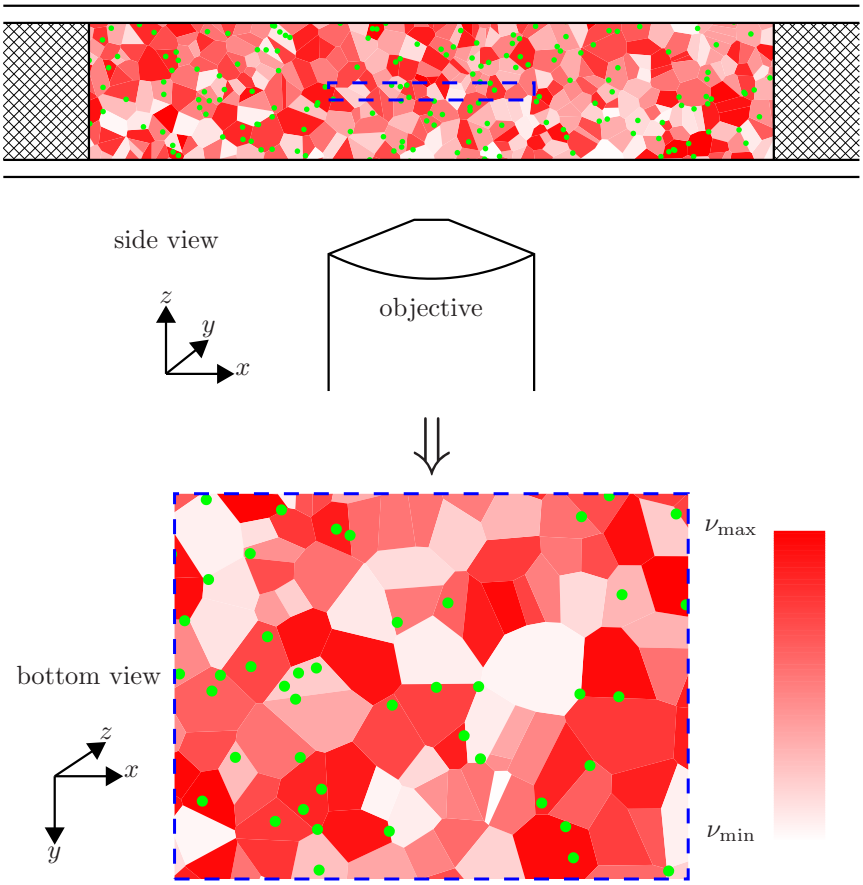

Fig. 5.1: Schematic of an heterogeneous system, as seen through a microscope. Different colors in the material correspond to different values of a certain material property ν. Randomly dispersed particles (green dots) are visible only when moving in a certain volume of observation (blue dotted frame) whose smallest dimension z_b in the z direction determine the limitations in sampling. The bottom view pictures a typical snapshot at a time t within the acquisition time interval.

trajectory $\mathbf{r}(t)$ exhibits a dynamic that, at a time scale $\tau = \omega^{-1}$, can be quantified by the distribution of the displacements $\mathbf{d}_t(\tau) = \mathbf{r}(t+\tau) - \mathbf{r}(t)$. Usually, a measure of the local material property is made by calculating the mean-squared displacement $m_t(\tau, \boldsymbol{\rho}) = \mathbb{E}[\mathbf{d}_t(\tau)^2 \,|\, \mathbf{r}(t) = \boldsymbol{\rho}] = \int_{-\infty}^{+\infty} \boldsymbol{\delta}^2 P_{\mathbf{d}_t(\tau)\,|\,\mathbf{r}(t)}(\boldsymbol{\delta} \,|\, \boldsymbol{\rho}) \mathrm{d}\boldsymbol{\delta}$, where the integral runs over all possible displacements. This material property is defined at a location $\mathbf{r}(t)$, within a minimum length scale given by the extend $\mathbf{d}_t(\tau)$ of the trajectory (i.e. the amplitude of the deformation applied to the material), and over which the material is assumed homogeneous. From the stationary assumption, this property is independent of t, and we will write it $m(\tau, \boldsymbol{\rho})$. Hence the distribution that is accessible with the technique

is $P_{m(\tau)\,|\,\mathbf{r}}(m\,|\,\boldsymbol{\rho}) = \delta[m - m(\tau,\boldsymbol{\rho})]$ and the central moments (or moments about the mean) of $P^{\mathrm{u}}_{m(\tau)}(m) = V^{-1}\int_V P_{m(\tau)\,|\,\mathbf{r}}(m\,|\,\boldsymbol{\rho})\mathrm{d}\boldsymbol{\rho}$, obtained with uniform spatial distribution of positions in the volume V ($P_{\mathbf{r}}(\boldsymbol{\rho}) = V^{-1}$), can be used to quantify the heterogeneity of the material through the probes' dynamics heterogeneity (we will expose some limitations to this idea in the next sections). Such moments can be written in terms of the raw moments:

$$\mathbb{E}[m(\tau)^r] = \int_0^{+\infty} m^r P^{\mathrm{u}}_{m(\tau)}(m)\mathrm{d}m = V^{-1}\int_V \left[\int_{-\infty}^{+\infty} \boldsymbol{\delta}^2 P_{\mathbf{d}(\tau)\,|\,\mathbf{r}}(\boldsymbol{\delta}\,|\,\boldsymbol{\rho})\mathrm{d}\boldsymbol{\delta}\right]^r \mathrm{d}\boldsymbol{\rho} \tag{5.1}$$

We can note at this point that since the quantity to estimate involves two integrations, there will be two levels of sampling when performing the experiments. A first level of sampling is obtained in the spatial integration (outer integral in equation 5.1) since in practice, only a finite number of locations will be investigated. A second level of sampling needs to be characterized, as the number of sample displacements obtained per given sample location will be eventually small, and will thus require a binning of the volume of observation. It is then possible to gather observed displacements by grouping their corresponding location into spatial bins, and then calculate the inner integral of equation 5.1 in each bin.

In the multiple particle tracking technique, trajectories of the probes' Brownian motion are obtained by processing movies acquired with video microscopy. The sampling of the material is limited in space by the volume of observation $V_{\mathrm{b}} \subset V$ (camera field of view in the plane and tracking depth in the direction perpendicular to the plane, see section 2.3) which contains $N_{\mathrm{b}}(t)$ probes particles at a given time t (see figure 5.1). A limitation in time is naturally given by the duration of acquisition $T_{\mathrm{b}} = n_{\mathrm{b}}\Delta t$, where Δt is the time interval between two successive movie frames, and $n_{\mathrm{b}}+1$ is the number of frames. The output of the tracking is a set of N probe trajectories $\{\mathbf{r}_i(t)\}_{1\leq i\leq N}$, each trajectory being sampled every Δt. We will write $\mathbf{R} = \{\{\mathbf{r}_{i,j} = \mathbf{r}_i(j\Delta t + t_i) \in V_{\mathrm{b}}\}_{0\leq j\leq n_i}\}_{1\leq i\leq N}$ the sample of observed positions, where $T_i = n_i\Delta t$ is the duration of the trajectory i and t_i is the time of first observation. Several trajectories can eventually correspond to a single particle that leaves and comes back in the volume of observation, such that in general, $N_{\mathrm{b}}(t) \leq N$ and $T_i \leq T_{\mathrm{b}}$. For a lag time $\tau = n\Delta t$ and for trajectories such that $T_i \geq \tau$ (i.e. $n_i \geq n$), we can extract $q_i(n) = n_i + 1 - n$ overlapping (hence *a priori* non-independent) displacements from the trajectory i and we obtain the sample $\mathbf{D}(n) = \{\{\mathbf{d}_{i,j}(n) = \mathbf{r}_{i,j+n-1} - \mathbf{r}_{i,j-1}\}_{1\leq j\leq q_i(n)}\}_{i\in I(n)}$ of observed displacements, where $I(n) = \{i : n_i \geq n\}$ is the set of indices corresponding to trajectories longer than τ. The corresponding set of positions associated with $\mathbf{D}(n)$ will be written $\mathbf{R}(n) = \{\{\mathbf{r}_{i,j-1}\}_{1\leq j\leq q_i(n)}\}_{i\in I(n)}$.

As noted earlier, in order to estimate equation 5.1 the volume V_{b} must be subdivided into M cells (or bins) of volume $\{V_k\}_{1\leq k\leq M}$, with $V_{\mathrm{b}} = \sum_{k=1}^{M} V_k$. To each bin corresponds a constant (assuming homogeneity on the bin size scale) value of the inner integral which we will call $m_k(\tau) = \mathbb{E}[m(\tau)\,|\,\boldsymbol{\rho} \in V_k] = m(\tau,\boldsymbol{\rho}_k)$, where $\boldsymbol{\rho}_k \in V_k$ is an hypothetical location of V_k. Suppose that it is possible to determine $m_k(\tau)$ using an estimator with arbitrary certainty $\widehat{g}(\mathbf{D}^{\mathrm{v}}_k(n))$ such that $\mathbb{E}[\widehat{g}(\mathbf{D}^{\mathrm{v}}_k(n))] = m_k(\tau)$ from any subset $\mathbf{D}^{\mathrm{v}}_k(n)$ of $\mathbf{D}(n)$ containing only displacements $\{\mathbf{d}_{i,j}(n)\}$ for which corresponding position $\{\mathbf{r}_{i,j-1}\}$ are in V_k. By making such an assumption, we aim at characterizing the first level of sampling only, discarding the second level which will be discussed

later in the text. The estimator of the spatial moments of $m(\tau)$ are then:

$$\begin{aligned}\widehat{\mathbb{E}}[m(\tau)] &= \textstyle\sum_{k=1}^{M} \pi_k \widehat{g}(\mathbf{D}_k^{\mathrm{v}}(n)) \\ \widehat{\mu}_2[m(\tau)] &= \frac{\sum_{k=1}^{M} \pi_k \big[\widehat{g}(\mathbf{D}_k^{\mathrm{v}}(n)) - \sum_{k=1}^{M} \pi_k \widehat{g}(\mathbf{D}_k^{\mathrm{v}}(n))\big]^2}{\sum_{k=1}^{M} \pi_k (1-\pi_k)}\end{aligned} \tag{5.2}$$

where $\pi_k = V_k/V_{\mathrm{b}}$, as obtained from the usual sample estimator of the weighted mean and variance with uncorrelated samples. The difficulty is to build the set $\{V_k\}_{1\leq k\leq M}$ such that, on the one hand the statistical accuracy within each cell is high enough (obtained by increasing V_k, which in turn will decrease M), and on the other hand to have enough bins to calculate moments, and such that the assumption of uniformity within cluster is valid by sampling the space at a fine enough scale (large M). In other word, there is a compromise between gaining accuracy in estimating the inner integral in the equation and accuracy in the outer integral calculation. For generality, it is convenient to have a formula independent of the choice of $\{V_k\}_{1\leq k\leq M}$. This can be achieved under some reasonable assumptions. We first assume that each trajectory is entirely contained in one of the bins $\{V_k\}_{1\leq k\leq M}$. We can then write:

$$\widehat{g}(\mathbf{D}_k(n)) = \big(\textstyle\sum_{i\in I_k} n_i\big)^{-1} \sum_{i\in I_k} n_i \widehat{g}(\mathbf{D}_i(n)) \tag{5.3}$$

where $\mathbf{D}_i(n)$ is the subset of $\mathbf{D}(n)$ corresponding to trajectory i, and I_k is the set of indices corresponding to trajectories contained in V_k. Next we assume $(\sum_{i\in I_k} n_i)/V_k = C_{\mathrm{b}} n_{\mathrm{b}}$ is independent of k, where C_{b} is the uniform density of particle in the material (recall that $\sum_{i\in I_k} n_i$ is the total number of observed positions in V_k). We get:

$$\begin{aligned}\widehat{\mathbb{E}}[m(\tau)] &= \textstyle\sum_{i=1}^{N} p_i \widehat{g}(\mathbf{D}_i(n)) \\ \widehat{\mu}_2[m(\tau)] &= \frac{\sum_{i=1}^{N} p_i \big[\widehat{g}(\mathbf{D}_i(n)) - \sum_{i=1}^{N} p_i \widehat{g}(\mathbf{D}_i(n))\big]^2}{\sum_{k=1}^{M} \pi_k (1-\pi_k)}\end{aligned} \tag{5.4}$$

where $p_i = n_i / \sum_{i=1}^{N} n_i$. The denominator of $\widehat{\mu}_2[m(\tau)]$ is a correcting factor for the bias, and approaches 1 for $M \gg 1$. At this point it is possible to also characterize the uncertainty of these estimators due to only the first level of finite spatial sampling. Using again common formula for the variance of the sample mean and of the sample variance, we have:

$$\begin{aligned}\mu_2[\widehat{\mathbb{E}}[m(\tau)]] &= \mu_2[m(\tau)] \textstyle\sum_{k=1}^{M} \pi_k^2 \\ \mu_2[\widehat{\mu}_2[m(\tau)]] &= (\mu_4[m(\tau)] - \mu_2[m(\tau)]^2) \textstyle\sum_{k=1}^{M} \pi_k^2 + O\big(\sum_{k=1}^{M} \pi_k^2\big)\end{aligned} \tag{5.5}$$

The calculation of the quantity $\sum_{k=1}^{M} \pi_k^2$ requires the knowledge of the individual volume V_k for all $1 \leq k \leq M$. However, at an instant t of the measurement, the number of sample locations observed in the volume is $N_{\mathrm{b}}(t)$. We can then argue for this calculation that the uncertainty in the first level of spatial sampling is $\propto \mathbb{E}[N_{\mathrm{b}}(t)]^{-1} = N_{\mathrm{b}}^{-1}$. Thus we will write $\sum_{k=1}^{M} \pi_k^2 \approx N_{\mathrm{b}}^{-1}$ when estimating the above quantities.

As pointed out earlier in the text, only trajectories for which $T_i \geq \tau$ will be counted in the displacement sample. For a trajectory shorter than τ, the corresponding $\mathbf{D}_i(n)$ is empty and no estimator $\widehat{g}(\mathbf{D}_i(n))$ can be computed. The duration of a trajectory T_i is in fact an observation of

another random variable whose distribution depends, among other factors, on the dynamics of the corresponding particle. Hence, a particle that is likely to travel across the volume of observation (say its smallest dimension) over a lag time τ will not be tracked for a sufficient time to perform any computation from its trajectory. The corresponding material in which probes undergo such dynamics will be *transparent* to the technique. A possible quantitative indicator of this effect is

$$\theta(n) = \frac{\sum_{i\in I(n)} n_i}{\sum_{i=1}^{N} n_i} \ . \tag{5.6}$$

It is the ratio of the number of positions for which a displacement at lag n has been measured over the total number of observed positions (over which the sum runs in the estimators, equation 5.2, where such effect has been discarded by the initial assumption). Limiting behaviors of this indicator are reached when all position are associated with a displacement ($\theta(n) = 1$ and the sampling is at its best), and when no sample displacements could be calculated ($\theta(n) = 0$ and the material is totally transparent to the technique). Furthermore, we will show in the following section that this transparency factor is a good measure to characterize the effect of the volume of observation on the quality of the estimators subsequently derived.

To conclude this section, we notice that this choice of bins $\{V_k\}_{1\leq k\leq M}$ is not unique. For example, bins of identical shape and size could be chosen to divide V_b independently of the sample $\mathbf{R}$. Their size and number would then need to be adjusted for each lag time to reach the best statistical accuracy. The latter might be challenging to evaluate on-the-fly. The bins could also be construct randomly by Voronoi tessellation from a subset of $\mathbf{R}$. The choice made here, relying on the assumption that a particle probes a unique material property along its path, is a more natural procedure in the particle tracking framework.

In the next two sections, we investigate the second level of statistics involved in the evaluation of $\widehat{g}(\mathbf{D}_i(n))$.

5.3.2 Characterization of the Sample of Displacements

For simplicity, we will consider only 1 dimensional random walks in the x direction. The output of a multiple particle tracking experiment is a list of 1 dimensional overlapping displacements as defined earlier, $D(n) = \{\{d_{i,j}(n) = x_{i,j+n-1} - x_{i,j-1}\}_{1\leq j\leq q_i(n)}\}_{i\in I(n)}$. Here we look at the characteristics of this sample. If all processes $x_{i,j}$ are assumed stationary with respect to the time j, as well as *independent* from one another, then we can immediately write the following second order characterization:

$$\begin{aligned} \mathbb{E}\big[d_{i,j}(n)\big] &= 0 \\ \mathbb{E}\big[d_{i,j}^2(n)\big] &= m_i(n) \\ \mathbb{E}\big[d_{i,j}(n)d_{i',j'}(n)\big]/\mathbb{E}\big[d_{i,j}^2(n)\big] &= \delta_{ii'}\rho_{n,i}^{(1)}(j-j') \end{aligned} \tag{5.7}$$

where $\delta_{ii'}$ designates the Kronecker delta and where the correlation coefficient $\rho_{n,i}^{(1)}(h)$ can be expressed in terms of the mean-squared displacement $m_i(n)$:

$$\rho_{n,i}^{(1)}(h) = \frac{[m_i(h+n) - m_i(h)] + [m_i(h-n) - m_i(h)]}{2m_i(n)} \tag{5.8}$$

Under the assumption that all displacements are Gaussian distributed, this second-order characterization is sufficient to know all other moments of the displacement samples. For example, an interesting characteristic when calculating power of the mean-squared displacements is the correlation coefficient of the squared displacements:

$$\frac{\mathbb{E}\big[d^2_{i,j}(n)d^2_{i',j'}(n)\big] - \mathbb{E}\big[d^2_{i,j}(n)\big]\mathbb{E}\big[d^2_{i',j'}(n)\big]}{\mathbb{E}\big[d^4_{i,j}(n)\big] - \mathbb{E}\big[d^2_{i,j}(n)\big]^2} = \delta_{ii'}\rho^{(2)}_{n,i}(j-j') \tag{5.9}$$

where it can be shown that $\rho^{(2)}_{n,i}(h) = [\rho^{(1)}_{n,i}(h)]^2$. We show typical values of $\rho^{(1)}_n(h)$ in Fig. 5.2 for various dynamics $m(n)$. We observe that in general the overlapping displacements are correlated up to a non-universal lag h. More interestingly, we see on this figure that even if the displacements are not overlapping ($h \geq n$), anti-correlation can be observed. To this regard, only the Newtonian dynamics (pure diffusion, $m \propto |n|$ in figure 5.2A) exhibits uncorrelated successive displacements. We can conclude then that the observations of the squared-displacement will also exhibit correlations in a non-universal way.

This will present a problem when applying common estimator formulas involving squared sums of observations. A common way to de-correlate observations is to perform block-average transformation [88]. We define the s-sized block-average of the rth power displacement the following way:

$$\underline{d_r}_{i,j}(n) = \frac{1}{s}\sum_{l=0}^{s-1} d^r_{i,sj-l}(n) \tag{5.10}$$

The characteristic of the these new observations can be also calculated:

$$\begin{aligned} \mathbb{E}\big[\underline{d_r}_{i,j}(n)\big] &= \mathbb{E}[d^r_{i,j}(n)] \\ \frac{\mathbb{E}\big[\underline{d_r}_{i,j}(n)\underline{d_r}_{i',j'}(n)\big] - \mathbb{E}\big[\underline{d_r}_{i,j}(n)\big]\mathbb{E}\big[\underline{d_r}_{i',j'}(n)\big]}{\mathbb{E}\big[\underline{d_r}^2_{i,j}(n)\big] - \mathbb{E}\big[\underline{d_r}_{i,j}(n)\big]^2} &= \delta_{ii'}\underline{\rho_r}_{n,i}(j-j') \end{aligned} \tag{5.11}$$

where we compute the block averaged transform of the displacement auto-correlation coefficient:

$$\underline{\rho_r}_{n,i}(h) = \frac{\sum_{k=-(s-1)}^{s-1}(1-|k|/s)\rho^{(r)}_{n,i}(|h|s+k)}{\sum_{k=-(s-1)}^{s-1}(1-|k|/s)\rho^{(r)}_{n,i}(k)} \tag{5.12}$$

We plot in Fig. 5.2 the correlation $\underline{\rho_1}_{n,i}(1)$ of successive block-averaged displacements as a function of s and we see that the choice $s = n$ de-correlates successive block-averaged displacements. This apparent de-correlation is effectively a smoothing of the raw displacements correlation, that can be observed for higher order correlation coefficient ($\underline{\rho_r}_n(h)$ is also almost zero for $r > 1$ and for $h \geq 1$, even though it is not the case for the corresponding $\rho^{(r)}_n(h)$; data not shown). A more general definition of the block-averaged r-th power displacement is given by:

$$\underline{d_r}_{i,j}(n) = \frac{1}{s_i(n)}\sum_{l=0}^{s_i(n)-1} d^r_{i,s_i(n)j-l} \tag{5.13}$$

where $s_i(n) = n$ if $q_i(n) \geq n$, $s_i(n) = q_i(n)$ otherwise. For each trajectory, we obtain $\underline{q}_i(n)$ block-

averaged displacements with $\underline{q}_i(n)$ equals the the biggest integer smaller than $q_i(n)/s_i(n)$. It forms a sample $\underline{D_r}(n) = \{\{\underline{d_r}_{i,j}(n)\}_{1\leq j\leq \underline{q}_i(n)}\}_{i\in I(n)}$ of mutually uncorrelated observations. Note that this choice of $s_i(n)$ does not lead to a significant loss of statistics as compared with calculation made with non-overlapping displacements. In the latter, approximately n_i/n displacements can be extracted from trajectory i, comparable to $\underline{q}_i(n)$.

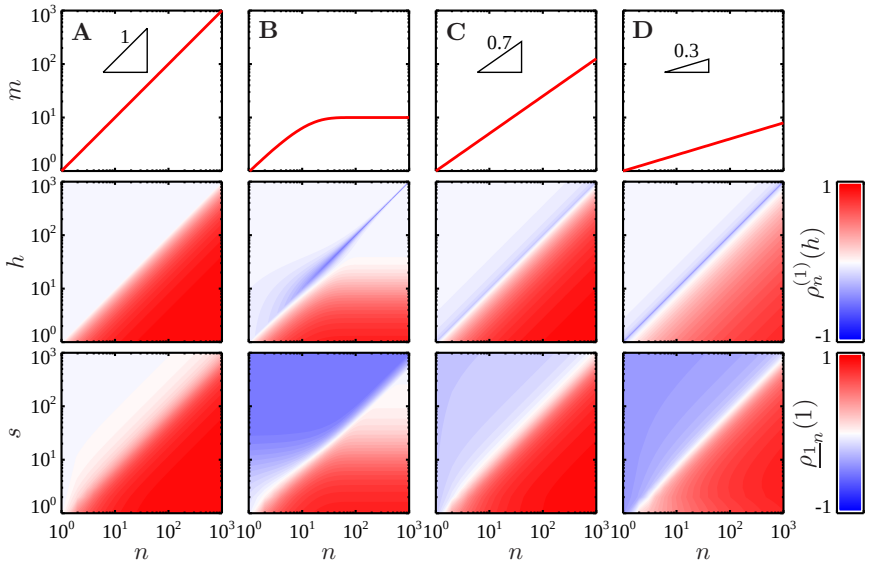

Fig. 5.2: Auto-correlation coefficients of the displacements and of the block-averaged displacements. Different dynamics $m(n)$ are investigated: (A) is a purely Newtonian fluid $m(n) \propto |n|$, (B) is a Voigt fluid model with relaxation time of 10, $m(n) \propto 1 - e^{-|n|/10}$, (C) and (D) are 0.7 and 0.3 power law dynamics, $m(n) \propto |n|^{0.3}$ and $m(n) \propto |n|^{0.7}$ respectively. The plots on the second row give the displacements' auto-correlation coefficient $\rho_n^{(1)}(h)$ as a function of (n, h) for the corresponding dynamics shown in the first row. The third row of plots show the auto-correlation coefficient of two successive boxed averaged displacements $\rho_{\underline{1}_n}(1)$ as a function of (n, s) (see text for notations).

5.3.3 The Estimators

We define the weighted sample mean:

$$\overline{d^p}(n) = \sum_{i\in I(n)} \sum_{1\leq j\leq q_i(n)} w_i(n) d_{i,j}^p(n) \quad \text{with} \quad w_i(n) = [n_i/q_i(n)]/\sum_{i\in I(n)} n_i \tag{5.14}$$

over the sample $D(n)$. Similarly, we will write:

$$\overline{\underline{d_r}^p}(n) = \sum_{i\in I(n)} \sum_{1\leq j\leq \underline{q}_i(n)} \underline{w}_i(n) \underline{d_r}_{i,j}^p(n) \quad \text{with} \quad \underline{w}_i(n) = [n_i/\underline{q}_i(n)]/\sum_{i\in I(n)} n_i \tag{5.15}$$

over the sample $\underline{D_r}(n)$. In general, $\overline{\underline{d_r}^p}(n) \neq \overline{d^{rp}}(n)$ unless $p = 1$, where the two terms differ only by the number of sample displacement lost when taking the integer part of $q_i(n)/s_i(n)$. However we have $\mathbb{E}[\overline{\underline{d_r}}(n)] = \mathbb{E}[\overline{d^r}(n)]$.

We define the estimator $\widehat{M_1}(n)$ of $M_1(n) = \mathbb{E}[m(n)]$ by:

$$\widehat{M_1}(n) = \overline{d^2}(n) = \sum_{i\in I(n)} w_i(n) \sum_{1\leq j\leq q_i(n)} d_{i,j}^2(n) \tag{5.16}$$

The second level expectation is:

$$\mathbb{E}[\widehat{M_1}(n) \,|\, \{V_k\}_{1\leq k\leq M}] = (\sum_{i\in I(n)} n_i)^{-1} \sum_{i\in I(n)} n_i m_i(n) = \sum_{i\in I(n)} p_i m_i(n) \tag{5.17}$$

and is unbiased in the first level for $\theta(n) = 1$ (see equation 5.4). If the system is homogenous however, $\widehat{M_1}(n)$ is unbiased for any values of $\theta(n)$, as it will be shown in the next section.

To calculate the variance of $\widehat{M_1}(n)$, we note that there are two independent contributions in the uncertainty of the estimator, each contribution coming from the two different levels of sampling mentioned earlier in the text. To see this, let us briefly derive a simplified result. We consider a set of N unbiased estimators $\{\widehat{a}_i\}_{1\leq i\leq N}$ of a corresponding set of values $\{\alpha_i\}_{1\leq i\leq N}$, the latter forming a sample of independent observations of a random variable α. Similar to the current study, we have here two levels of statistical uncertainty when estimating some moments of α: one level is affecting the accuracy of estimating each α_i with $\widehat{a}_i$, and the other is coming from the limited number of observation α_i. In the first level, we have $\mathbb{E}[\widehat{a}_i \,|\, \alpha_i] = \alpha_i$ and we define the variance of the estimator $\widehat{a}_i$ by $\mu_2[\widehat{a}_i \,|\, \alpha_i] = \mathbb{E}[\widehat{a}_i^2 \,|\, \alpha_i] - \mathbb{E}[\widehat{a}_i \,|\, \alpha_i]^2 = \beta_i/n_i$ where n_i is the number of sample used to calculate $\widehat{a}_i$. We can calculate the mean and variance of the quantity $\widehat{a} = N^{-1} \sum_{1\leq i\leq N} \widehat{a}_i$ that is an estimator of $\mathbb{E}[\alpha]$. We use iterated expectation to write:

$$\mathbb{E}[\widehat{a}] = \mathbb{E}\big[\mathbb{E}[\widehat{a} \,|\, \{\alpha_i\}_{1\leq i\leq N}]\big] = \mathbb{E}\big[N^{-1} \sum_{1\leq i\leq N} \alpha_i\big] = \mathbb{E}[\alpha] \tag{5.18}$$

which shows that the estimator is unbiased. The same way, we find:

$$\begin{aligned} \mathbb{E}\big[\mathbb{E}[\widehat{a}^2 \,|\, \{\alpha_i\}_{1\leq i\leq N}]\big] &= \mathbb{E}\big[N^{-2} \sum_{1\leq i\leq N} \beta_i/n_i + N^{-2}\big(\sum_{1\leq i\leq N} \alpha_i\big)^2\big] \\ &= \mathbb{E}[\beta/n]/N + \mu_2[\alpha]/N + \mathbb{E}[\alpha]^2 \end{aligned} \tag{5.19}$$

such that finally, the variance of the estimator $\widehat{a}$,

$$\mu_2[\widehat{a}] = \mu_2[\alpha]/N + \mathbb{E}[\beta/n]/N \tag{5.20}$$

is the sum of two terms. The first term comes from the level of sampling the random variable α with the N observations α_i and is $\propto N^{-1}$, and the second term includes the uncertainties from the estimation of each α_i by $\widehat{a}_i$ and is $\propto (Nn)^{-1}$, where Nn is the total number of initial observations. In the current study, the first term corresponds to the expression given given by equation 5.5 for the first level of spatial sampling. The second term can be calculated by assuming the system homogeneous (that is taking $\mu_2[\alpha] = 0$ in the demonstration presented above), which means that all initial observation are taken from the same distribution. Note also that from intermediate calculations in the above demonstration, we get

$$\mu_2[\widehat{a} \,|\, \{\alpha_i\}_{1\leq i\leq N}] = \mathbb{E}[\widehat{a}^2 \,|\, \{\alpha_i\}_{1\leq i\leq N}] - \mathbb{E}[\widehat{a} \,|\, \{\alpha_i\}_{1\leq i\leq N}]^2 = N^{-2} \sum_{1\leq i\leq N} \beta_i/n_i \tag{5.21}$$

of order $(Nn)^{-1}$. This result will be useful in the following derivations.

We follow this idea to calculate the variance of $\widehat{M}_1(n)$. We use the approximation $\overline{d^2}(n) \approx \overline{\underline{d_2}}(n)$, the mean of the sample $\underline{D_2}(n)$ of uncorrelated observations. In that case, it is possible to show that the variance $\mu_2[\widehat{M}_1(n)]_\mathrm{h}$ obtain when all observations in $\underline{D_2}(n)$ are identically distributed (assumption of homogeneity), is estimated by:

$$\widehat{\mu}_2[\widehat{M}_1(n)]_\mathrm{h} = \frac{\left[\overline{\underline{d_2}^2}(n) - \overline{\underline{d_2}}(n)^2\right] \sum_{i\in I(n)} \underline{q}_i(n)\underline{w}_i(n)^2}{\sum_{i\in I(n)} \underline{q}_i(n)\underline{w}_i(n)[1-\underline{w}_i(n)]} \tag{5.22}$$

so that the total expression is:

$$\widehat{\mu}_2[\widehat{M}_1(n)] = \frac{\widehat{M}_2(n)}{N_\mathrm{b}} + \widehat{\mu}_2[\widehat{M}_1(n)]_\mathrm{h} \tag{5.23}$$

where we have used equation 5.5 with $\widehat{M}_2(n)$ an estimator of $M_2(n) = \mu_2[m(n)]$.

To calculate $\widehat{M}_2(n)$, we assume that all displacements are Gaussian distributed. In that case, we find that:

$$\widehat{M}_2(n) = \overline{d^4}(n)/3 - \widehat{M}_1(n)^2 \tag{5.24}$$

is almost unbiased. Indeed, for the first term in $\widehat{M}_2(n)$, we have

$$\mathbb{E}[\overline{d^4}(n) \,|\, \{V_k\}_{1\leq k\leq M}] = 3(\textstyle\sum_{i\in I(n)} n_i)^{-1} \sum_{i\in I(n)} n_i m_i(n)^2 \tag{5.25}$$

since $\mathbb{E}[d^4] = 3\mathbb{E}[d^2]^2$ for a zero-mean Gaussian random variable d. The expectation of the second term can be written:

$$\mathbb{E}[\widehat{M}_1(n)^2 \,|\, \{V_k\}_{1\leq k\leq M}] = \mathbb{E}[\widehat{M}_1(n) \,|\, \{V_k\}_{1\leq k\leq M}]^2 + \mu_2[\widehat{M}_1(n) \,|\, \{V_k\}_{1\leq k\leq M}] \tag{5.26}$$

where the second term is of order $\sum_{i\in I(n)} \underline{q}_i(n)\underline{w}_i(n)^2$ from equation 5.21, that is of the order of the inverse total number of displacement $\sum_{i\in I(n)} n_i$ in $D(n)$. This second term can thus be neglected, and we finally get:

$$\mathbb{E}[\widehat{M}_2(n) \,|\, \{V_k\}_{1\leq k\leq M}] = \textstyle\sum_{i\in I(n)} p_i \big[m_i(n) - \sum_{i\in I(n)} p_i m_i(n)\big]^2 + O\big[\big(\sum_{i\in I(n)} n_i\big)^{-1}\big] \tag{5.27}$$

which is the estimate given in equation 5.4 for the first level of uncertainty. To estimate $\mu_2[\widehat{M}_2(n)]$ we follow the same line of reasoning as for the variance of $\widehat{M}_1(n)$. The variance $\mu_2[\widehat{M}_2(n)]_\mathrm{h}$ under the homogeneity assumption is estimated by:

$$\widehat{\mu}_2[\widehat{M}_2]_\mathrm{h} = \left[\frac{\overline{\underline{d_4}^2} - \overline{\underline{d_4}}^2}{9} + 4\overline{\underline{d_2}}^2\big(\overline{\underline{d_2}^2} - \overline{\underline{d_2}}^2\big) - \frac{4\overline{\underline{d_2}}}{3}\big(\overline{\underline{d_2}}\,\overline{\underline{d_4}} - \overline{\underline{d_2 d_4}}\big)\right]\big(\textstyle\sum_{i\in I(n)} n_i\big)^{-1} + O\big[\big(\sum_{i\in I(n)} n_i\big)^{-2}\big] \tag{5.28}$$

where have dropped the dependency in n for conciseness. The first level term given by equation 5.5 requires the estimation of $\mu_4[m(n)]$ (the other term $\mu_2[m(n)]$ is estimated by $\widehat{M}_2(n)$), which is obtain under the Gaussian assumption:

$$\widehat{\mu}_4[m] = \overline{d^8}/105 - 4\overline{d^2}\,\overline{d^6}/15 + 2\overline{d^2}^2\overline{d^4} - 3\overline{d^2}^4 + O\big[\big(\textstyle\sum_{i\in I(n)} n_i\big)^{-1}\big] \tag{5.29}$$

so that finally:

$$\widehat{\mu}_2[\widehat{M_2}] = \left(\widehat{\mu}_4[m] - \widehat{M_2^2}\right)N_\mathrm{b}^{-1} + \widehat{\mu}_2[\widehat{M_2}]_\mathrm{h} \tag{5.30}$$

We give in the appendix the IDL procedure that allows us to calculate these statistics.

5.3.4 The Assumptions

We remind here the main assumptions that have been used in order to derive the above formula for the estimators.

- The probes' motions are stationary
- Constant number of particles in the box at any given time: $N_\mathrm{b}(t) = N_\mathrm{b} = C_\mathrm{b}V_\mathrm{b}$
- A single trajectory reports the motion of a probe in a locally homogeneous fluid
- The displacements are Gaussian distributed
- Trajectories are independent

5.4 Specific Methods

5.4.1 Brownian Dynamics Simulations

We used Brownian dynamics simulations to test the validity of the estimator. Simulations are convenient as they provide both the freedom of design and a well-defined system. The input parameters are easily changed and well controlled in wide range of values. However we must first ensure the validity of these range as compared with real experimental design.

Scaling and Range of Parameters

The smallest dimension of the volume of observation given in the z direction is called z_b. Its value depends on the depth of field of the multiple particle tracking technique as well as the tracking parameters. But typical values range form $1\,\mu$m to $10\,\mu$m. The concentration of probes particle is chosen such that minimal interaction between particles is expected, and given the magnification, between 10 and 100 particles can be track simultaneously ($10 < N_\mathrm{b} < 100$). The video rate is usually not greater than 100 Hz, thus the time interval between consecutive frames is $\Delta t > 0.01\,\mathrm{s}$. The duration of the movie is limited by the number of frames storable in memory, but typically $T_\mathrm{b} = 1000\Delta t$. The smallest viscosity encountered in typical applications is the one of water $\eta = 10^{-3}\,\mathrm{Pa}\cdot\mathrm{s}$, and at $T = 25°\mathrm{C}$ with smallest trackable particle radius $a = 0.05\,\mu$m, we get that $\xi = 6\pi a\eta > 1\,\mathrm{cP}\cdot\mu\mathrm{m}$. Throughout the following sections, we will use quantities made dimensionless with the distance z_b and the time Δt. Hence, in the following we will designate the dimensionless quantity using $\widetilde{\ldots}$, such that for example $\widetilde{m} = m/z_\mathrm{b}^2$ designates the dimensionless mean-squared displacement. However, to avoid redundancy, the dimensionless lag time and acquisition duration are written $n = \widetilde{\tau} = \tau/\Delta t$ and $n_\mathrm{b} = \widetilde{T}_\mathrm{b} = T_\mathrm{b}/\Delta t$ respectively, as already introduced earlier.

Brownian Dynamics Simulations

A Brownian dynamics simulation was employed to create particle trajectories [52]. An explicit first-order time-stepping algorithm was used to advance the position $\mathbf{r}_j(t)$ of a particle j at time t:

$$\mathbf{r}_j(t+\delta t) = \mathbf{r}_j(t) + \dot{\mathbf{r}}_j(t)\delta t$$

where δt is the time step and $\dot{\mathbf{r}}_j(t)$ satisfies the following stochastic differential equation:

$$\dot{\mathbf{r}}_j(t) \simeq \frac{1}{\xi_j}\mathbf{F}_j(\mathbf{r}_j(t)) + \sqrt{\frac{2k_\mathrm{B}T}{\xi_j \delta t}}\mathrm{d}\mathbf{W}_j$$

obtained by assuming the drag on the particle to be Stokesian and by neglecting any other hydrodynamic interactions. Also, $\mathbf{F}_j(\mathbf{r}) = -k_j[\mathbf{r} - \mathbf{c}_j]$ is the Hookean linear force law applied to the particle by the medium from the fixed center position $\mathbf{c}_j$ ($\mathbf{F}_j(\mathbf{r}) = \mathbf{0}$ when simulating a Newtonian fluid) and $\mathbf{W}_j$ is a Wiener process that satisfies $\langle \mathrm{d}\mathbf{W}_j \rangle = \mathbf{0}$ and $\langle \mathrm{d}\mathbf{W}_j \mathrm{d}\mathbf{W}_j \rangle = \boldsymbol{\delta}$ where $\boldsymbol{\delta}$ is the unit second-order tensor [52]. The model fluid is then characterized by the properties $\nu_j = (\xi_j, k_j)$, and dynamics by $m(\tau) = 2k_\mathrm{B}T(1 - e^{-k_j|\tau|/\xi_j})/k_j$ in each direction. N_b trajectories of duration T_b were simulated. The effect of the finiteness of the volume of observation is taken into account only in the z direction of the motion $\mathbf{r}(t) = (x(t), y(t), z(t))$, where only positions verifying $0 \leq z(t) < z_\mathrm{b}$ can be observed. In practice, the N_b force centers $\{c_j\}_{1 \leq j \leq N_\mathrm{b}}$ are uniformly distributed in an interval $[0, z_\mathrm{b}]$ in the z direction. About these centers, N_b initial positions $\{z_j(0)\}_{1 \leq j \leq N_\mathrm{b}}$ are randomly chosen from the equilibrium distribution, $P_{z_j(0)}(z) \propto e^{-k_j(z-c_j)^2/(2k_\mathrm{B}T)}$. This ensures that the system is at thermal equilibrium at $t = 0$. The trajectories are then simulated starting from these positions. For each trajectory $\mathbf{r}_j(t)$, with $1 \leq j \leq N_\mathrm{b}$, the first z position that lies outside the box interval $[0, z_\mathrm{b})$ is translated by a length z_b to fall back in the observable interval. Accompanying this translation, an index of trajectory is incremented and assigned to the fragment of trajectory starting from this translated point. The process is repeated over time to obtain a fragment of the original $\mathbf{r}_j(t)$ divided by this periodic boundary conditions in the z direction. After performing this transformation to the N_b initially simulated trajectories, all the fragments are re-indexed to obtain the sample $\{\mathbf{r}_i(t)\}_{1 \leq i \leq N}$ of N tracks. By always keeping all successive positions in the volume of observation, the condition of constant particles density, $\sum_{i=1}^{N} T_i = N_\mathrm{b}T_\mathrm{b}$ is verified at all reported time steps. For all sets of simulation, $\delta t = 10^{-1}\Delta t$. We verified that our results did not appreciably change for smaller values of δt. Allowing the density $N_\mathrm{b}(t)$ to fluctuate by observing only a subvolume $[0, z'_\mathrm{b}]$ of the initial box $[0, z_\mathrm{b}]$ is a more detailed model of a real multiple particle particle tracking experiments. But again by doing so, we could not observe significant change in the results, whereas the computation time is increased.

In the following, the friction coefficient and spring constant are made dimensionless by using $\widetilde{\xi} = \xi/(k_\mathrm{B}T\Delta t/z_\mathrm{b}^2)$ and $\widetilde{k} = k/(k_\mathrm{B}T/z_\mathrm{b}^2)$ respectively. From the previous discussion about the range of parameters met in experiments, we conclude that typically $\widetilde{\xi} > 10$.

5.4.2 Experiments

Simple bimodal heterogeneous systems were made by creating gel features in the field of view of the multiple particle tracking technique. We used microscope projection photolithography [89] to create well-defined region of gels with embedded beads, within a region of purely viscous, unpolymerized

material equally populated with the probe particles.

Materials

We used a solution of 10% (v/v) poly(ethylene glycol)(700) diacrylate (PEG-DA, Sigma-Aldrich), 0.5% (v/v) solutions of Darocur 1173 (Sigma Aldrich) initiator, 20% (v/v) ethanol (95% grade, Pharmco) and 20% (v/v) 5×TBE buffer, in which 0.518 μm diameter carboxylate modified yellow-green particles at a volume fraction $\phi = 2.48 \times 10^{-3}\%$ where thoroughly dispersed by 20 minutes sonication. The sample where injected in a 150 μm high chamber sealed with vacuum grease shortly after (see section 2.1.1 for details).

Photopolymerization and Tracking

Four photomasks with unique pinholes of diameter 470, 700, 800 and 900 μm were designed in Autocad 2005 and printed using a high resolution printe at CAD art Services (Poway, CA). The masks were then inserted into the field-stop of the microscope. A 100 W HBO mercury lamp served as the source of UV light. A filter set provides wide UV excitation (11000v2: UV, Chroma) was used to select light of the desired wavelength and a VS25 shutter system (Uniblitz) driven by a computer controlled VMM-D1 shutter driver provided specified pulses of UV light. The oligomer solutions mixed with probed particles where exposed for a time of 1.5 s to photopolymerize poles in the chamber by using the 10× objective. It has been shown that the poles are not cylindrical because of the shape of the light beam [90]. However they can be considered as straight poles over a length scale of 60 μm around the focus point of the beam. At this altitude in the chamber, their diameter are respectively $2R_{\text{gel}} = 110 \pm 4$, 170 ± 2, 200 ± 2 and $230 \pm 3\,\mu$m (this leads to a magnification of approximately 1/4 from the field-stop plan to the objective focal plane). With the 20× objective, we recorded the motion of the particles in a volume of observation placed such within this volumes, the poles are straight cylinders at all altitudes $z \in V_{\text{b}}$. The acquisitions were made at 10 frames per second (i.e. $\Delta t = 0.1\,\text{s}$) and for a duration of 2000 frames. We verified that such exposure time of the solution using the fluorescein matching fluorescent filter does not induce any photopolymerization. For the common tracking parameters used for the processing of the movies (in particular the clipping region for false locations removal were identical for all movies, see section 2.3), we find that we track approximately 250 particles in a field of view of dimensions $300 \times 300\,\mu$m, with a standard deviation of less than 5% of this mean $\langle N_{\text{b}} \rangle$. We can conclude that for these experiments, using the 20× objective, we have $z_{\text{b}} = 8.2 \pm 0.4\,\mu$m. Note that this length scale is smaller than the length scale of curvature of the poles profile in the z direction, ensuring that the polymerized structures are seen as straight cylinders in the experiments.

5.5 Results and Discussion

We investigated the quality of the estimator for two different dynamics. The purely diffusive dynamics in Newtonian liquid allows us to scan the parameter space $(n, \widetilde{m})$ using the relation $\widetilde{m}(n) = 2|n|/\widetilde{\xi}$ for varying $\widetilde{\xi}$. In the single relaxation time Voigt fluid, the space $(n, \widetilde{m})$ is investigated by changing $\widetilde{\xi}$ and $\widetilde{k}$ using the following dynamical relation: $\widetilde{m}(n) = 2(1 - e^{-|n|\widetilde{k}/\widetilde{\xi}})/\widetilde{k}$. These two kinds of dynamics do not cover all possible multi-relaxation time viscoelastic dynamics often encountered in microrheometry measurements on complex systems. However, they are simple models that are easily implemented with Brownian dynamics simulations, and they exhibit sufficiently

different dynamical characteristics to capture the effect of probe dynamics on the quality of the estimators, and more generally on the statistics of the obtained sample.

Before analyzing heterogeneous fluids having these two dynamics, it is instructive to evaluate and characterize the formula in homogeneous fluids.

5.5.1 Homogeneous Fluids

We performed simulations of homogeneous fluids using $\{\widetilde{\xi}_r = 10^{r/2}, \widetilde{k} = 0\}_{0\leq r\leq 11}$ to scan the parameter space $(n, \widetilde{m})$ using Newtonian dynamics $\widetilde{m}(n) = 2|n|/\widetilde{\xi}_r$ with different friction coefficients. Also, we used $\{\widetilde{\xi}_r = 10^{r/2}, \widetilde{k}_r = 10^{r/2}/5\}_{0\leq r\leq 11}$ to sample the parameter space using Voigt dynamics with a dimensionless relaxation time at $n_v = 5$: $\widetilde{m}(n) = 2(1 - e^{-|n|/5})/\widetilde{k}_r$. These parameters allow us to investigate $(n, \widetilde{m})$ around $\widetilde{m} = 1$ where the main effects of the finite volume of observation are expected to occur. But their range also report mean-squared displacements sufficiently low, $\widetilde{m} \ll 1$, so that the limit in which the volume of observation is infinite is approached. In the simulation method, the latter limit has been separately simulated by discarding the last step consisting of the trajectories subdivision.

For each of the 24 types of fluid (12 Newtonian and 12 Voigt), simulations were repeated 100 times to obtain 100 observations of the various random parameters of interest. These include the largest lag time $n_{\max}$ for which it is possible to calculate the estimators (chosen such that there remains at least two indices in the set $I(n_{\max})$), the transparency indicator $\theta(n)$ and the estimators $\widehat{M_1}(n)$ and $\widehat{M_2}(n)$. From the 100 simulations performed under identical conditions, these observations are calculated at common values of lag time from one simulation to another, so that statistics (mean and standard deviation) for each measure are calculated for a given n.

Figure 5.3 gives an overview of the results obtained for homogeneous fluids with $N_{\mathrm{b}} = 100$ and for two acquisition times, $T_{\mathrm{b}} = 1000$ and $T_{\mathrm{b}} = 100$. In particular it shows the mapping of the transparency factor in the parameter space $(n, \widetilde{m})$ for the two kinds of dynamics. In this figure, each solid black line represents the relation $\widetilde{m}(n)$ used in the experiments to map the space ($\widetilde{m}(n) \propto |n|$ for A and $\widetilde{m}(n) \propto 1-e^{-|n|/5}$ for B), and their end points (the maximum n at which they are drawn) is at $\mathbb{E}[n_{\max}]$.

First, we see that for mean-squared displacements above the observation limit 1, the transparency vanishes for both kinds of dynamics. This observation is not surprising, as for such values of mean-squared displacement, the probes are more likely to cross the entire volume of observation over a time less than the lag time. Hence a particle in the box at a given time t is likely to be outside the volume of observation at a time $t + \tau$, and thus its observed trajectory can not be used to extract a displacement at lag time τ.

More strikingly, we see that the transparency of a material at a lag time n and exhibiting a mean-squared displacement $\widetilde{m}$ with this technique depends on the entire dynamics $\widetilde{m}(n)$ and not only on the position $(n, \widetilde{m})$ in the parameter space (compare the different mapping of figure 5.3A and 5.3B). This dependency may seem surprising, in particular for the Voigt fluid for which some values of $(n, \widetilde{m})$ are transparent even though $\widetilde{m} \ll 1$. To provide some insights into this effect, we show in figure 5.4 typical trajectory durations n_i in a selection $\{\widetilde{\xi}_r = 10^{r/2}, \widetilde{k} = 0\}_{r\in\{0,3,6\}}$ of Newtonian dynamics and $\{\widetilde{\xi}_r = 10^{r/2}, \widetilde{k}_r = 10^{r/2}/5\}_{r\in\{0,3,6\}}$ of Voigt dynamics, as well as the resulting variation $\theta(n)$ of the transparency factor with the lag time n, for $N_{\mathrm{b}} = 100$ and $n_{\mathrm{b}} = 100$. In this figure, the middle plots where obtained by gathering together the trajectories coming from the same initial simulation (before taking the effect of a finite volume of observation into account).

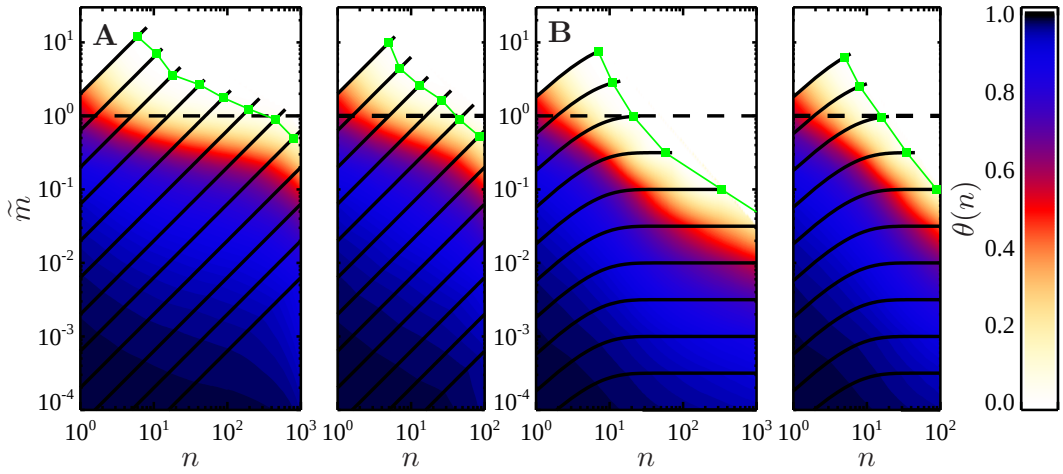

Fig. 5.3: Transparency factor $\theta(n)$ in the parameter space $(n, \widetilde{m})$ scanned by two different kind of dynamics $\widetilde{m}(n)$: (A) is a purely Newtonian fluid, for which $\widetilde{m}(n) \propto |n|$, and (B) is a Voigt fluid with relaxation time 5, that is $\widetilde{m}(n) \propto 1 - e^{-|n|/5}$. For each fluid type, two acquisition times were simulated, $n_\mathrm{b} = 1000$ on the left and $n_\mathrm{b} = 100$ on the right. The dashed line represents the observation limit $\widetilde{m} = 1$ due to the volume of observation. The green points represent the limit above which the relative bias of $\widehat{M_1}$, defined by equation 5.31, is greater than 5%.

Thus in these plots, a line corresponds to one of the N_b simulated particles, and the chopping of this line occurs at the successive absolute times when the corresponding particle crosses the observation volume's z boundaries.

From figure 5.4(A), for which $r = 0$ to figure 5.4(C) with $r = 6$, we see in the middle plots that trajectories are becoming longer, or equivalently, that the particles are leaving the volume of observation less frequently: from a given position in the volume of observation, slower particles (lower $\widetilde{m}$ at constant n) will not be as likely to reach a given boundary than faster particles (higher value of $\widetilde{m}$ for the same n). Consequently, the transparency factor at a given lag time n will increase from faster (higher $\widetilde{m}$) to slower (lower $\widetilde{m}$) dynamics, as seen in figure 5.4, right plots, from (A) to (C) (top to bottom). Also for each value of r (again $r = 0$ in (A), $r = 3$ in (B) and $r = 6$ in (C)), since the Voigt dynamics are "slower" than the corresponding Newtonian dynamics, we also verify that the transparency blue curve (Newtonian) falls below the corresponding red curve (Voigt). The peculiarity of the transparency factor is however visible by comparing the Newtonian dynamics of (C), $\widetilde{m}(n) = 2|n|/10^3$ and the Voigt dynamics of (B), $\widetilde{m}(n) = 2(1 - e^{-|n|/5})/10^{3/2}$. At a lag time $n = 100$, both exhibit similar values of $\widetilde{m}$ whereas the corresponding value of the transparency are remarkably different. Thus the transparency does not depend only on the particular value of $\widetilde{m}$, but rather on the entire dynamics of the probes. The transparency of certain fluids to multiple particle tracking is an important limitation of the technique. But the dynamic dependency of this

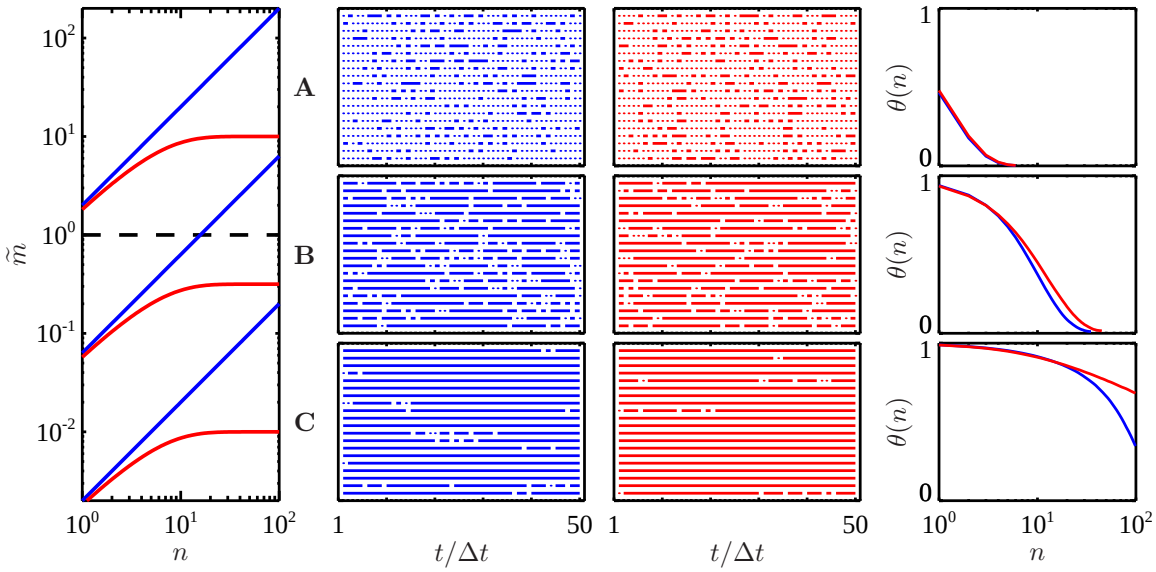

Fig. 5.4: Trajectory statistics. As shown in the left plot, the parameter space $(n, \widetilde{m})$ is sampled using purely viscous dynamics (in blue throughout the figure) with material properties $\{\widetilde{\xi}_r = 10^{r/2}, \widetilde{k} = 0\}_{r\in\{0,3,6\}}$ and Voigt dynamics with relaxation time 5 (in red throughout the figure), $\{\widetilde{\xi}_r = 10^{r/2}, \widetilde{k}_r = 10^{r/2}/5\}_{r\in\{0,3,6\}}$. In this left plot, the dashed line represents the observation limit $\widetilde{m} = 1$ due to the volume of observation. The remaining plots are meant to be read in rows, (A) to (C) from higher to lower values of $\widetilde{m}$ (i.e. from lower to higher values of the index r). The first two columns represent typical trajectory durations in each kind of fluid: a single dot means that the particle was observable for only 1 frame, and lines indicates trajectory of at least Δt long. Each row in these plots refers to the original simulated trajectory that has been fragmented to take limited observation volume into account (see section 5.4.1). The last column of plots on the right represent the corresponding variations of the transparency factor $\theta(n)$ as a function of n.

transparency is a particularly strong weakness that prevents some universality in judging a priori the feasibility of an experiment.

We also reported on figure 5.3 the relative bias of the first estimator $\widehat{M_1}(n)$, defined as follow:

$$b[\widehat{M_1}(n)] = \mathbb{E}[\widehat{M_1}(n)]/M_1(n) - 1 \tag{5.31}$$

where the above expected value is calculated from the 100 experiments repeated for each kind of fluid. For these homogeneous fluids, a bias of less than 5% is measured for almost the entire observed parameter space. In particular, it is not affected by the drop in the transparency of the material. In a wide part where the fluid is almost totally transparent, but where mean-squared

displacement can be reported, the bias is negligible. This is not surprising for the homogeneous fluids, as any observed displacement will report a valid measurement of the entire fluid. However, we will show in the next part how the bias is greatly affected by the non-uniform transparency in heterogeneous fluids.

We also observe that the estimator $\widehat{M_2}(n)$ is unbiased for this kind of fluid. We define, for this section only, the bias of $\widehat{M_2}(n)$ relative to $M_1^2(n)$ by:

$$b'[\widehat{M_2}(n)] = \mathbb{E}[\widehat{M_2}(n)]/M_1^2(n) \tag{5.32}$$

and we saw that the trends followed by this bias are very similar to the one followed by $b[\widehat{M_1}(n)]$ (not reported here), that is that $\widehat{M_2}(n)$ is unbiased for almost all the observable parameter space (the ensemble of points $(n, \widetilde{m})$ for which $\theta > 0$). Finally, we observe that these qualitative behaviors are not significantly changed when decreasing T_b from 1000 to 100 (see figure 5.3) or when decreasing N_b from 100 to 10 (not shown).

5.5.2 Heterogeneous Fluids

We use now the dynamics mentioned in the previous part to build heterogeneous fluids. Rather than trying to cover a wide variety of heterogeneous fluids, we will use a canonical model of heterogeneity to point out the influence of a finite volume of observation on measurements. The study of these simple systems, performed with both simulations and experiments, will be followed by a model fluid with a more complex heterogeneous nature, which will illustrate the power of the formula.

Bimodal Fluids

A canonical model for an heterogeneous fluid is given by a balanced bimodal system, where the fluid is composed for half of one kind, and the other half of another kind. More precisely, we define a set of balanced bimodal Newtonian fluids where half of the volume of observation is occupied with a liquid of friction $\widetilde{\xi}_r^{(1)} = 10^{r/2}$, and the other half exhibits a friction $\widetilde{\xi}_r^{(2)} = 10^{(r+1)/2}$, where $0 \leq r \leq 10$. The resulting probes dynamics are written $\widetilde{m}_r^{(1)}(n) = 2|n|/\widetilde{\xi}_r^{(1)}$ and $\widetilde{m}_r^{(2)}(n) = 2|n|/\widetilde{\xi}_r^{(2)}$. Similarly, a set of balanced bimodal Voigt fluids is built from a balanced mixture of $\{\widetilde{\xi}_r^{(1)} = 10^{r/2}, \widetilde{k}_r^{(1)} = 10^{r/2}/5\}$ on one side, and $\{\widetilde{\xi}_r^{(2)} = 10^{(r+1)/2}, \widetilde{k}_r^{(2)} = 10^{(r+1)/2}/5\}$ with $0 \leq r \leq 10$ and will lead to the two evenly likely dynamics $\widetilde{m}_r^{(1)}(n) = 2(1 - e^{-|n|/5})/\widetilde{k}_r^{(1)}$ and $\widetilde{m}_r^{(2)}(n) = 2(1 - e^{-|n|/5})/\widetilde{k}_r^{(2)}$. Referring to figure 5.3, we see that the described bimodal fluids are made of a balance composite of two successive dynamics represented by the black lines. The estimators $\widehat{M_1}(n)$ and $\widehat{M_2}(n)$ are built to evaluate:

$$\begin{aligned} \widetilde{M_1}(n) &= \frac{\widetilde{m}_r^{(1)}(n) + \widetilde{m}_r^{(2)}(n)}{2} \\ \widetilde{M_2}(n) &= \frac{\left[\widetilde{m}_r^{(1)}(n) - \widetilde{m}_r^{(2)}(n)\right]^2}{4} \end{aligned} \tag{5.33}$$

in these models.

In the simulation method, these fluids are obtained by simply simulating 50 initial trajectories in one homogenous component of the fluid, and then 50 trajectories in the other component.

The effect of the limited volume of observation is taken into account the same way as described in section 5.4.1. Practically, an experiment in such hypothetical fluid should be simulated by assigning random initial positions for each trajectory, uniformly distributed among the heterogeneous fluid. Hence, by exactly splitting the trajectory set in half, we discard in this part the random spatial sampling. It is aimed at isolating a specifically strong limitation of the method: the effect of transparency on the bias of the estimators. In the experiments described in the next section, the spatial sampling is naturally performed.

Referring again to figure 5.3, we observe that in general, along the lines representing the two dynamics involved in the bimodal fluid, the drop in transparency is reached at different values of n and $\widetilde{m}$. At a given lag time, the dynamics exhibiting higher $\widetilde{m}$, that is $\widetilde{m}_r^{(1)}$, will eventually become transparent at smaller lag time, and the tracking technique will then only probe the remaining observable side of the heterogeneous fluid at larger lag time. Consequently, the estimators of the mean and variance of the probes' dynamics will be biased for these large lag times.

To be more quantitative, we want to compare the transparency map as scanned by dynamics in the fluid of type (1), for which the mean-squared displacement is $\widetilde{m}_r^{(1)}(n)$, with a map of the estimators bias as scanned by the composite dynamics described by $\widetilde{M_1}(n)$. To perform this comparison quantitatively, we correlate in figure 5.5 the behavior of the levels at constant value of transparency, with constant levels of bias of $\widehat{M_1}(n)$ and $\widehat{M_2}(n)$ in the $(n, \widetilde{m})$ space. The bias is defined here for both estimators using equation 5.31:

$$b[\widehat{M_i}(n)] = \mathbb{E}[\widehat{M_i}(n)]/M_i(n) - 1 \quad \text{for } i = 1, 2 \tag{5.34}$$

Specifically, we used the transparency result obtained in homogenous fluid of kind (1) of the mixture to read the coordinates $(n_\theta, \widetilde{m}_\theta)$ on the corresponding curve $\widetilde{m}_\theta = \widetilde{m}_r^{(1)}(n_\theta)$, that reaches a given value θ of transparency. Then, at the same lag time n_θ, we read the bias of the estimators at the point $(n_\theta, \widetilde{M_1}(n_\theta))$. Then, by varying r, we obtain a curve of constant transparency (the red solid lines in figure 5.5 are for $\theta = 0.5$ and are extracted from the contour plots given in figure 5.3) for the fluid of kind (1), and a corresponding set of bias values (read at the blue squares in the left plots of figure 5.5) on the corresponding composite dynamics $\widehat{M_1}(n)$ (blue dashed line). The mean of this set of bias values for a given transparency is reported in the middle plots of figure 5.5 as a function of the transparency, the errors bars being given by the standard deviation of the same set. If these error bars are small, it means that to a given value of transparency of fluid (1) corresponds a well defined value of bias in the estimator.

To compare with other methods of calculation of the moments of dynamics, we also reported in figure 5.5 a "naive" calculation of the mean and variance of prior time averaged individual mean-squared displacements extracted from each trajectories [11, 29, 86]. The latter methods completely disregard eventual differences in trajectory durations (hence an apparent statistical heterogeneity in the accuracy of the individual mean-square displacement estimation). For these estimates, we repeated the study described in the previous paragraph: the results are given by the open symbols in the middle plots of figure 5.5.

In this figure, we see that as θ increases the bias of each estimator derived in this study vanishes. This is not the case for the "naive" calculations. Also, we remark that the error bars on each point are small compared with the ones on the open symbols, indicating that the transparency defined in the first section of this chapter is well correlated with the bias in the estimators. Note finally that the variation of the biases with the transparency is fairly independent of the nature of

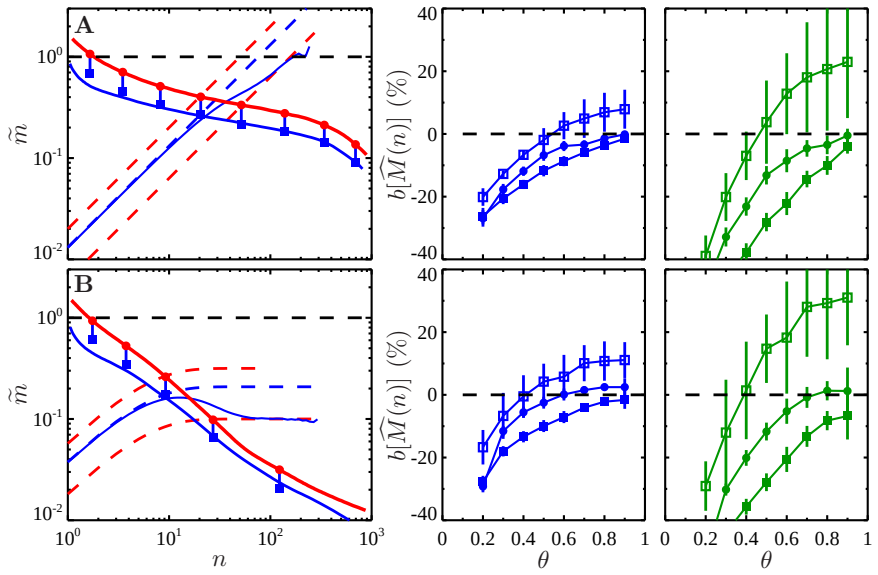

Fig. 5.5: Bias as a function of the transparency factor θ. The first row of plots corresponds to a mapping of the parameter space $(n, \widetilde{m})$ using Newtonian dynamics and the second row is for a Voigt dynamics mapping. On each row, the left plots shows the relation between the transparency factor (the red line corresponds to a constant $\theta = 0.5$) of the homogeneous fluid with the bias (the blue thick line is a constant relative bias of $\widehat{M}_1(n)$, the latter is plotted with the thin blue line) in an bimodal mixture. The composite fluid (dashed blue line) is made of a balanced mixture of two successive dashed red lines. The two right plots in each row shows the bias in $\widehat{M}_1$ (square) and $\widehat{M}_2$ (circles) as a function of θ. In blue is the variation of bias versus θ for the bimodal fluid described in the left plot. In green is the variation of the bias for bimodal fluid with greater difference in the dynamics. The open symbols of obtained using a naive approach for the corresponding estimators. Note that the open circles lie above 100%, outside the range of bias shown here.

the dynamics involved, Newtonian or Voigt. The right green plots in figure 5.5 show the results corresponding to balanced bimodal fluids with greater differences in the dynamics: $\widetilde{\xi}_r^{(1)} = 10^{r/2}$ mixed with $\widetilde{\xi}_r^{(1)} = 10^{r/2+1}$ for Newtonian dynamics, and $\{\widetilde{\xi}_r^{(1)} = 10^{r/2}, \widetilde{k}_r^{(1)} = 10^{r/2}/5\}$ with $\{\widetilde{\xi}_r^{(1)} = 10^{r/2+1}, \widetilde{k}_r^{(1)} = 10^{r/2+1}/5\}$ for the Voigt dynamics. We observe that the same conclusions still hold.

In the remaining, we will use an experimental unbalanced bimodal system and also simulate a complex and random heterogeneous fluid. To show the strength of the estimators, we will place the study in conditions where transparency of the fluid has negligible influence.

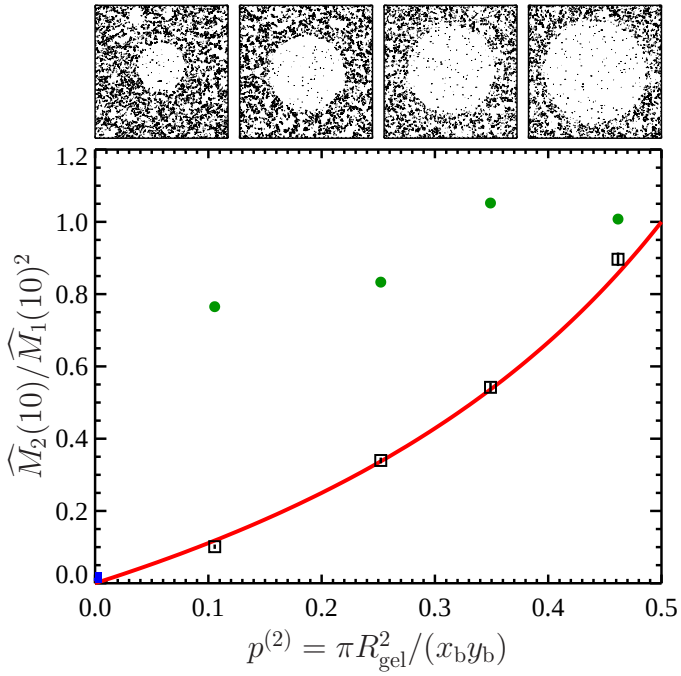

Fig. 5.6: Coefficient of variation of the probes dynamics in an heterogeneous unbalanced bimodal model experimental fluid. The black squares are estimation of the measure $\mu_2[\widetilde{m}(n)]/\mathbb{E}[\widetilde{m}(n)]^2$ using $\widehat{M}_2(n)/\widehat{M}_1(n)^2$ for the four bimodal fluids created by photopolymerization at $n = 10$. The four top windows are the corresponding measured trajectories in these model systems. Each image has dimensions $x_{\text{b}} = y_{\text{b}} = 300\mu$m. The centered circular gelled region, where the particles are trapped, have radii $R_{\text{gel}} = 55, 85, 100$ and $115\,\mu$m respectively from left to right. The solid blue square was obtain in the homogenous system $R_{\text{gel}} = 0$. The red line is the theoretical equation 5.35. The green points are the results of a naive calculation of the coefficient of variation as explained in the previous section about the simulated bimodal fluids (see also figure 5.5).

Experimental bimodal fluid

As explained in section 5.4, the experimental bimodal fluid is composed of a region of viscous uncrosslinked oligomer solution, and a circular region of known radius where the material is a stiff gels. By performing multiple particle tracking on homogenous system made of each kind, we observed that the motion of the beads in the gel is below spatial resolution, such that the effective mean-squared displacement are constant and measured at $m = 5 \times 10^{-4}\,\mu\text{m}^2$. In the other kind, particles are freely diffusing and we found a diffusion coefficient $D = 0.25 \pm 0.005\,\mu\text{m}^2.\text{s}^{-1}$. In unit distance $z_{\text{b}} = 8.2\,\mu$m and unit time $\Delta t = 0.1\,$s (see section 5.4), we have an unbalanced bimodal fluid with $\widetilde{m}^{(1)}(n) = 2|n|/10^{3.44} \gg \widetilde{m}^{(2)}(n) = 2/10^{5.43}$. Each fluid is observed with respective

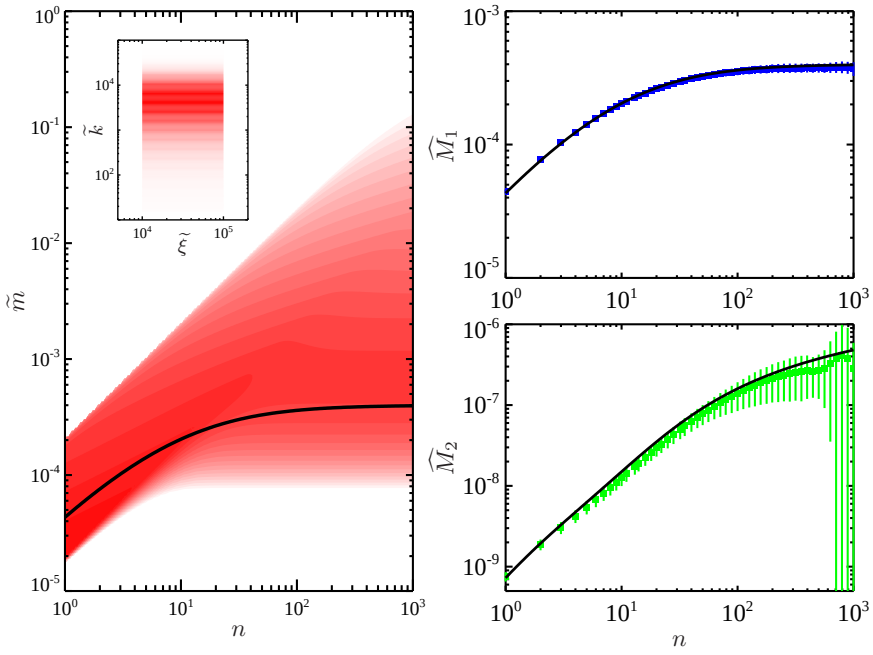

Fig. 5.7: Estimators $\widehat{M}_1$ and $\widehat{M}_2$ calculated for a random fluid. The parameter space $(n, \widetilde{m})$ is sampled with purely Voigt dynamics for which the drag coefficient $\widetilde{\xi}$ is uniformly distributed between 10^4 and 10^5, and the spring constant $\widetilde{k}$ is Gamma distributed with mean 10^4 and a shape parameter of 2 ($\widetilde{\xi}$ and $\widetilde{k}$ are statistically independent). The resulting probability density of $(n, \widetilde{m})$ is given on the left plot, where the black solid line indicates the mean $\mathbb{E}[\widetilde{m}(n)]$. The two right plots compares the results of $\widehat{M}_1$ (top) $\widehat{M}_2$ (top) obtained by the simulations (symbols) with the theoretical values M_1 and M_2 (solid lines).

probability $p^{(1)} = 1 - p^{(2)}$ and $p^{(2)} = \pi R^2_{\text{mask}}/(x_\text{b} y_\text{b})$. In that case, we can show that the coefficient of variation is given by:

$$\frac{\mu_2[m(\tau)]}{\mathbb{E}[m(\tau)]^2} = \frac{\widetilde{M}_2(n)}{\widetilde{M}_1(n)^2} = \frac{p^{(2)}}{1 - p^{(2)}} + O\left[\frac{\widetilde{m}^{(2)}}{\widetilde{m}^{(1)}}\right] \tag{5.35}$$

We estimate the above coefficient of variation using $\widehat{M}_2(n)/\widehat{M}_1(n)^2$. The lag time n is chosen such that the transparency of fluid (1) is closer to one. From the figure 5.3, we evaluate that θ significantly drops at about $n = 100$, in accordance to what we observed in the experiments on the homogenous fluid of kind (1) (data not shown). So we evaluated in figure 5.6 the ratio $\widehat{M}_2(n)/\widehat{M}_1(n)^2$ at $n = 10$ to discard any bias from the transparency. At this lag time, we found an excellent agreement between the estimator of the coefficient of variation and the theoretical value

given by equation 5.35 for the whole range of reported $p^{(2)}$.

Random Fluid

To conclude the characterization of the estimators, we simulated a random heterogeneous fluid the following way. Each probe undergoes a purely Voigt dynamic, $\widetilde{m}(n) = 2(1 - e^{-|n|\widetilde{k}/\widetilde{\xi}})/\widetilde{k}$, where the parameters $\widetilde{\xi}$ and $\widetilde{k}$ are independently distributed according to the following uniform and Gamma probability density function:

$$\begin{aligned} P_{\widetilde{\xi}}(x) &= (10^5 - 10^4)^{-1} \quad \text{for } 10^4 \leq x \leq 10^5 \text{ and 0 otherwise} \\ P_{\widetilde{k}}(x) &= 4xe^{-2x/10^4}/10^8 \quad \text{for } 0 \leq x \text{ and 0 otherwise} \end{aligned} \tag{5.36}$$

As seen in figure 5.7, we again find good agreement between the estimators $\widehat{M}_1$ and $\widehat{M}_2$, and the theoretical result for $\widetilde{M}_1$ and $\widetilde{M}_1$ respectively. Small deviations are visible at high lag times where eventually transparency of the faster dynamics in the fluid, for which the mean-squared displacement appraches the volume size limit, can alter the bias of the estimators.

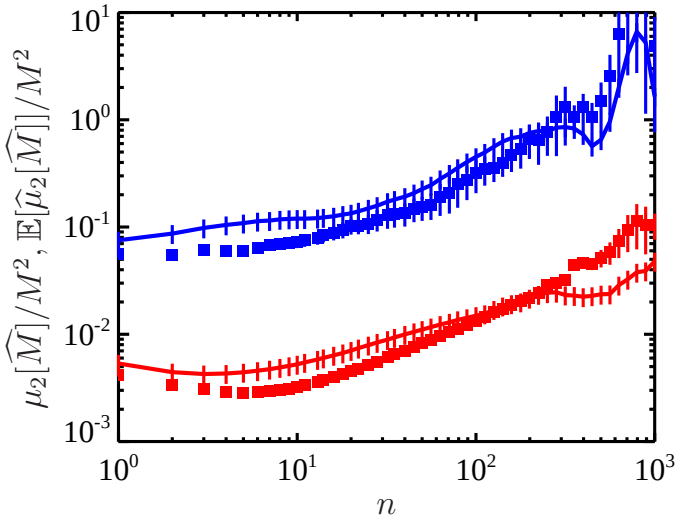

Fig. 5.8: Estimators $\widehat{\mu}_2[\widehat{M}_1]$ (red squares) and $\widehat{\mu}_2[\widehat{M}_2]$ (blue squares) calculated for the random fluid of figure 5.7 and scaled by the squared mean $M_1^2 = \mathbb{E}[m]^2$ and the squared variance $M_2^2 = \mu_2[m]^2$ respectively. The solid lines are the correspondingly scaled estimates of $\mu_2[\widehat{M}_1]$ and $\mu_2[\widehat{M}_2]$ obtained from repeating the simulation 100 times (that is, calculated directly from the histograms of $\widehat{M}_1$ and $\widehat{M}_2$ respectively).

For this advanced example, we plot in figure 5.8 the estimators $\widehat{\mu}_2[\widehat{M}_1]$ (equation 5.23) and $\widehat{\mu}_2[\widehat{M}_2]$ (equation 5.30) for the variances $\widehat{M}_1$ and $\widehat{M}_2$ respectively. In this figure, we also report the

results for these two estimators with the corresponding estimates of $\mu_2[\widehat{M}_1]$ and $\mu_2[\widehat{M}_2]$ obtained from the 100 simulation performed for the same random fluid. We see on this figure a good agreement between the two estimates, ensuring the validity of the expressions of $\widehat{\mu}_2[\widehat{M}_1]$ and $\widehat{\mu}_2[\widehat{M}_2]$ derived in section 5.3.3. These estimators should be used to indicate error bars on $\widehat{M}_1$ and $\widehat{M}_2$. Note finally that such agreement between $\widehat{\mu}_2[\widehat{M}]$ and $\mu_2[\widehat{M}]$ has been observed for all simulation results reported throughout this chapter.

5.6 Conclusions

We have presented here a study of the sampling design in the output of a multiple particle tracking experiment. This specific sampling of measured displacements at random locations in a material is made peculiar because, on one hand the displacements are connected into trajectories, and on the other hand because the volume of observation is finite. After having modeled the sampling design, we derived estimators for the mean and variance of the probes dynamics that are independent of the peculiar statistical characteristics. In particular, we compared the performance of our formula with other "naive" methods previously employed, and we showed that the precise assessment of the statistics in the multiple particle tracking output was essential in order to provide accurate unbiased measurements. Up to a certain extend that we also characterized through a transparency factor, these estimators can be applied to quantify the heterogeneity of a material, providing with a novel kind of information on a complex fluid property.

CHAPTER 6

Multiple Particle Tracking to Monitor the Kinetics of Peptides Self-Assembly

In the previous chapters we have presented in great detail the multiple particle tracking technique. In particular, we have shown some intrinsic limitations in the technique, but we have also presented methods to overcome these limits and to extract efficiently a great amount of information from the measurements. In this chapter we applied the multiple tracking measurements to a complex biomaterial called self-assembling peptides. This gelling system is of high importance for biomedical application, where it currently serves as a medium for 3D cell culture. However, it has not been fully characterized at the colloid length scale yet. This is due to the many challenges it presents, one of which is the time-depence of its structural and mechanical state. To this regard, multiple particle tracking is a well-suited and novel approach to study these self-assembling biomaterials. In this chapter, we study the kinetics of the gel formation.

6.1 Introduction

6.1.1 Self-Assembling Peptides

General Overview

Molecular self-assembly is, by definition, the spontaneous organization of molecules into well-defined, ordered and rather stable arrangements through a number of weak non-covalent interactions

[91]. These interactions typically include hydrogen bonds, ionic bonds and van der Waals' forces to assemble these molecules. There are numerous examples of molecular self-assembly in nature (a non-exhaustive list can be found in [92]) and it has been used as a powerful approach for fabricating novel biomaterials (see [92, 93] for a review). A new class of peptide-based biological materials has been discovered a decade ago, from the molecular self-assembly of ionic self-complementary oligomeric peptides [94]. These peptides are short, simple to design, extremely versatile and easy to synthesize. Moreover, this class of biological materials has considerable potential for a number of applications, including scaffolding for tissue repair and tissue engineering [95, 96], drug delivery of molecular medicine, as well as biological surface engineering. Consequently, a number of peptide molecular self-assembly systems have been designed and developed (see [97] and references therein). Among the numerous designs that have been and currently are investigated, a class of peptide self-assemble into nanoscale fibers [94, 95, 98, 99, 100, 101] and fiber network scaffolds [102, 95, 103, 96].

Inspired by the repetitive pattern found in the sequence of natural fibrous protein, short peptide have been designed containing two distinct side, one hydrophilic, the other hydrophobic (the molecule is thus amphiphilic), and forming complementary ionic bond with regular repeats of polar amino acids on the hydrophilic surface (see figure 6.1 for an example of such β-strand). It has been shown that these designs tend to form β-sheet structures [94, 104, 99, 98, 105]. One example of such systems is described in detail in the next section. When dissolved in water, self-assembly of these peptides occurs to form a network of filaments that macroscopically behaves like a gelatinous material, even at concentration of peptides as low as 0.5wt%.

KFE8 as Model System

The peptide called KFE8, consisting of two repeats of the sequence FKFE and whose molecular model is given in Figure 6.1, is one of the shortest peptides that forms a well-defined β-sheet structure. This design, or very similar ones, has been extensively studied as a model system for this class of peptide forming fibrous matrices [106, 99, 107, 98, 105, 108]. Besides the use of these matrices for the biomedical applications mentioned earlier in the text, the fibers share many features with the amyloid fibrils found in protein conformational diseases. They are thus used as model systems to study the formation and structure of amyloids [109].

As shown in [98, 105], the self-assembly of KFE8 forms a bilayer of β-sheet tapes, with hydrophobic side chains between the tapes, that take the form of left-handed helical ribbons intermediates. The geometry of the latter, shown on Figure 6.2, was experimentally resolved through the atomic force and transmission electron micrograph [98] reproduced in figure 6.3.

Several factors promote the self-assembly, although the mechanism by which these peptides coalesce to form a network is not clearly understood. It is known however that self-assembly of KFE8 is sensitive to pH and ionic strength of the solution due to ionizable side chains. Caplan et al. explained this dependence in terms of the Derjaguin-Landau-Verwey-Overbeek (DLVO) theory [99]. They hypothesized that self-assembly of KFE12 (three repeats of FKFE) is promoted by the hydrophobic effect [1], but hindered by electrostatic repulsion of the charge-like faces of the molecule. When the molecule carries zero net charge, or when the charges are screened, self-assembly of fibers occurs extremely rapidly. In order to slow down the process and to observe the intermediates, the peptide is usually dissolved in deionized micro-filtered water, which gives a pH of approximately 3 due to residual trifluoroacetic acid (TFA) from peptide synthesis (see [99, 107, 98]

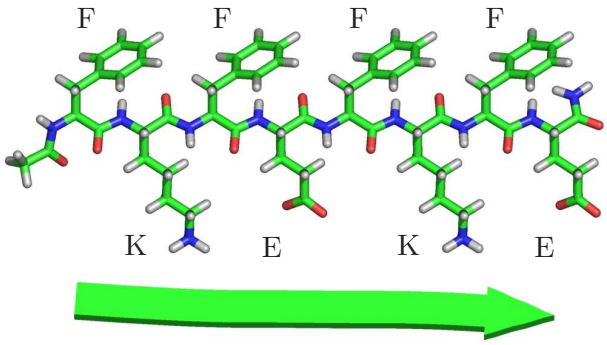

Fig. 6.1: Molecular model of KFE8. Lysine (K) and glutamic acid (E) are hydrophilic, while phenylalanine (F) is hydrophobic. The arrow symbolizes the peptide in β-strand conformation (see Figure 6.2). The N- and C-termini are respectively acetylated and amidated. The size of one KFE8 molecule is approximately 3.1 nm × 1.2 nm × 0.4 nm (reproduced from [105]).

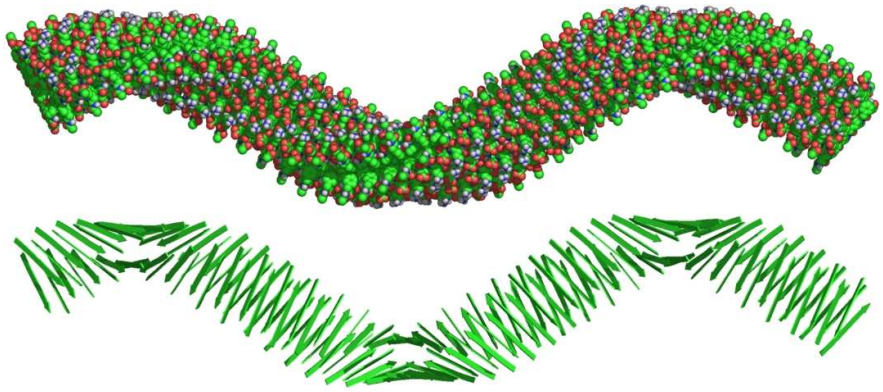

Fig. 6.2: Molecular modeling of a left-handed helical ribbons formed by self-assembly of KFE8. The ribbon is formed of a double helical β-sheet, and hydrophobic side chains are buried between the two helices. One helical turn is 20 nm and the diameter is 7 nm (reproduced from [105]).

and later in the text). At this pH, the molecules carry a net positive charge and self-assembly is slower (the time series of the micrographs shown in figure 6.3 suggest a kinetic of assembly of a few hours at pH=3.3).

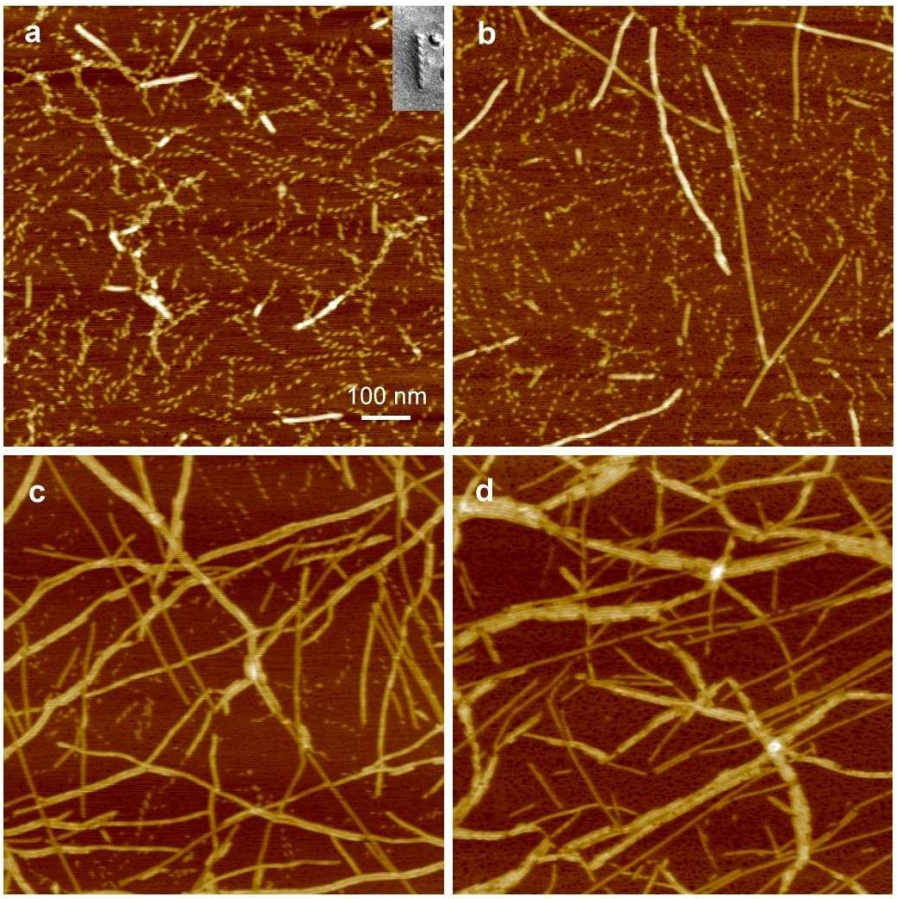

Fig. 6.3: AFM scans of the intermediate structures in the self-asssembly of KFE8, taken at different times after preparation of the solution: a) after 8 min (inset is a TEM micrograph); b) after 35 min; c) 2 h and d) 30 h (reproduced from [98]).

However studies in references [98, 105, 108] were focused on early time intermediate structures. In particular, molecular dynamics simulations have shown that the hydrophobic contacts precede the backbone hydrogen bonds growth [108], and have investigated the stability of the helical intermediate supramolecular structures [105]. The studies by Caplan et al. relate the effect of relieving electrostatic molecular repulsion in the peptide to the late equilibrium states mechanics of the formed hydrogel [99, 107, 110]. The kinetics of the network formation can be partly resolved using circular dichroism (CD) spectroscopy [98]. These measurements reported a steady increase in β-sheet structures and a concurrent decrease in the presence of coils. However, the knowledge of how these fibers interact (e.g. crosslink or intertwine) and contribute progressively to the formation of a solid network cannot be assessed with CD spectroscopy. On the other hand, rheological

characteristics of the material dramatically change during the transition from a viscous, liquid-like solution to a viscoelastic gel state of the material.

6.1.2 Multiple Particle Tracking in Time-Evolving Systems

Here we use multiple particle tracking microrheology to follow the hydrogel formation of the KFE8 self-assembling peptide system. In chapter 1 we have seen the advantages offered by microrheology techniques over traditional bulk rheology measurement. For example, the initial state of the evolving system might contain fragile structures, that will be either disrupt by bulk rheology, or eventually have effects that fall below the detection limit of the rheometer. To this regard, microrheomoetry is well suited to report accurate measurements in weak gel, without breaking their structural components. Another advantage of multiple particle tracking microrheology is that measurements are fast and the state of the sample, contained in a closed chamber, is not effected by external factor (e.g. evaporation). This quality is in dramatic contrast with bulk rheology, where measurements are usually longer, and advanced sample preparation technique had to be elaborated to circumvent evaporation [99].

Consequently, microrheology has been used to study time-evolving systems such as a gelling actin network [65, 66], the sol-gel transition of starch [111], solvent-responsive complex fluids [32] and photopolymerizing photosensitive acrylate resins [112] similar to the one used in chapter 5. In these gelling systems, great care has to be applied to the system's chemistry and to the eventual influence of the probes, through their surface chemistry or simply their fluctuating motion, on the solid network formation mechanism. In this chapter, we evaluate the influence of the pH of the solution of peptide KFE8 on the kinetics of self-assembly, by using multiple particle tracking microrheology.

6.1.3 Overview

The balance of this chapter is organized as follows. The first part explains in detail how the sampled are prepared in order to obtain consistently reproducible results. The next part validate the methods of multiple particle tracking to extract a characteristic time of gelation. Next we show our results on the kinetics dependency on pH, that we interpret in the last section in terms of a simple DLVO model for the peptides' interaction.

6.2 Specific Methods

The peptide KFE8, of sequence $[COCH_3] - FKFEFKFE - [CONH_2]$ was custom-synthesized from Synpep Corporation (Dublin, CA), and the lyophilized powder was stored at 4°C. Solutions of 3 mg/ml were obtained by thoroughly mixing the powder with deionized filtered water for 18 min using cycles of 1 min vortexing and 5 min sonicating to obtain a homogeneous solution. Immediately after mixing, the concentration of powder was reduced to 1 mg/ml in a solution of fluorescent particles. The beads we used were amine-modified 1 μm diameter particle (Molecular Probes, Eugene, OR), and carboxylate-modified with diameters of 0.518 and 0.925 μm (Polysciences, Warrington, PA). The final volume fraction of fluorescent beads was such that $\phi \leq 0.05\%$. Also, this concentration of powder was chosen to match other previous studies [98, 105]. Vortexing for 1 min ensured the beads to be well dispersed in the solution. Finally, NaOH was added at the target concentration to increase the pH of the solution. When kinetics studies were performed, the initial

time ($t_{\text{gel}} = 0$) was chosen at the moment of the addition of NaOH, that was followed by a final step of short vortexing of 30 s. This mixing protocol was carefully followed for all multiple particle tracking measurement and ensured a great level of reproducibility (see later in the text).

The sample was then rapidly loaded into a chamber for observation (see section 2.1.1) that was mounted on the microscope to perform immediate measurements. The particles' motion was observed with a 40× objective for the 1 and 0.925 μm diamter particle, and a 63× water immersion objective for the 0.518 μm particle. Movies of 1000 frames were recorded at a rate of 30 frames per seconds. The image processing algorithm where applied to the de-interlaced movie to obtain a temporal resolution of 60 Hz (see chapter 2 for a full description of the multiple particle tracking technique).

The ensemble averaged mean-squared displacements were calculated from the multiple trajectories following the formula 5.16 given in chapter 5, and corrections for the static errors were applied using methods described in chapter 3.

6.3 Results

6.3.1 Peptide Solution Titration

Titration was performed on a sample of KFE8 solution prepared the same way as described above. However, after reducing the concentration of powder from 3 mg/ml to 1 mg/ml, small volumes of NaOH were added to perform the titration, such that the final concentration of powder is not modified by more than 2%. Moreover, we observed that the pH is independent of the time of measurement during the self-assembly. Also, we verified that the addition of beads does not affect the titration result, whether their surface chemistry is amine or carboxylate.

The solid squares in figure 6.4 give the result of the titration of the powder. We observe that the pH of the solution with no addition of NaOH is very low at 3.2, consistent with other reported values [98, 99]. This low pH is due to the presence of residual trifluoroacetic acid (TFA) from peptide synthesis. The pH variation of the solution as the concentration of NaOH resembles a classic titration curve with a sharp jump of pH at a concentration [NaOH] = 1.4 mM.

We can use a simple titration model to evaluate the concentration of TFA in the original powder. The dissociation constants for the glutamic acid EH and for the Lysine KH^+ present in the peptide are written:

$$K_{\text{E}} = \frac{[\text{E}^-][\text{H}^+]}{[\text{EH}]} = 10^{-\text{pK}_{\text{E}}} \quad \text{and} \quad K_{\text{K}} = \frac{[\text{K}][\text{H}^+]}{[\text{KH}^+]} = 10^{-\text{pK}_{\text{K}}} \tag{6.1}$$

where pK_{E} and pK_{K} are the pK values of EH and KH^+ respectively. The standard value for these constant, $\text{pK}_{\text{E}} = 4.3$ and $\text{pK}_{\text{K}} = 10.8$ [113], are modified by the surrounding peptide chain and the electrostatic interaction, and we use the "apparent" pK values, $\text{pK}_{\text{E}} = 3.6$ and $\text{pK}_{\text{K}} = 11.2$ for the individual titratable groups [114, 105]. The same way, for the trifluoroacetic acid TH we write:

$$K_{\text{T}} = \frac{[\text{T}^-][\text{H}^+]}{[\text{TH}]} = 10^{-\text{pK}_{\text{T}}} \tag{6.2}$$

with $\text{pK}_{\text{T}} = 0.52$. If we call $[\text{KFE8}]_0$ and $[\text{T}]_0$ the initial concentration of peptides and TFA in the powder solution, we write the conservation of species by $[\text{E}^-]+[\text{EH}] = [\text{K}]+[\text{KH}^+] = 2[\text{KFE8}]_0$ and $[\text{T}^-]+[\text{TH}] = [\text{T}]_0$. The neutrality of the solution gives $[\text{Na}^+]+[\text{KH}^+]+[\text{H}^+] = [\text{E}^-]+[\text{T}^-]+[\text{OH}^-]$

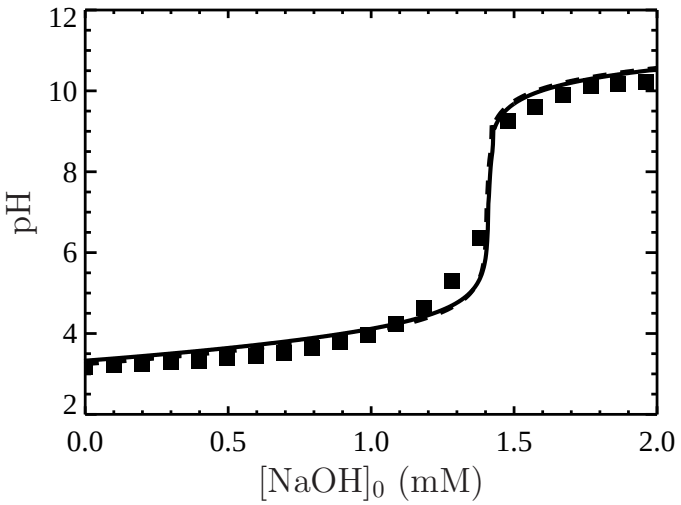

Fig. 6.4: Titration curve of the KFE8 solution at 1 mg/ml of powder. The squares are experimental results, whereas the lines are from the model described by equation 6.3. The solid line is the best match with the experimental jump in pH, assuming the powder contains only KFE8 and TFA complexes (that is the purity in peptide is exactly given by $1162.5/(1162.5 + n \times 114)$). We find $n = 1.95$ and $p = 84\%$. The dotted line is obtained for 70% purity in peptide, and the corresponding number of TFA per peptide is $n = 2.3$.

so that finally, the pH variations are described by

$$[\mathrm{NaOH}]_0 + \frac{2[\mathrm{KFE8}]_0}{1 + 10^{\mathrm{pH}-\mathrm{pK_K}}} + 10^{-\mathrm{pH}} = \frac{2[\mathrm{KFE8}]_0}{1 + 10^{\mathrm{pK_E}-\mathrm{pH}}} + \frac{[\mathrm{T}]_0}{1 + 10^{\mathrm{pK_T}-\mathrm{pH}}} + 10^{\mathrm{pH}-14} \tag{6.3}$$

which can be numerically solved for the pH at each value of $[\mathrm{NaOH}]_0$ reached in the titration, and knowing the initial concentrations $[\mathrm{KFE8}]_0$ and $[\mathrm{T}]_0$. The molecular weight of the peptide molecule is $1162.5\,\mathrm{g.mol^{-1}}$ and the one of TFA is $114\,\mathrm{g.mol^{-1}}$. Assuming both species, peptide and TFA, form a complex during the synthesis, this complex has a mass $1162.5 + n \times 114\,\mathrm{g.mol^{-1}}$ where n is the number of TFA molecule per molecule of peptide. When mixing 1 mg of powder in 1 ml of water, we obtain the concentrations $[\mathrm{KFE8}]_0 = p/1162.5\,\mathrm{M}$ and $[\mathrm{T}]_0 = pn/1162.5\,\mathrm{M}$, where p is a purity level of peptide in the powder which is less than $1162.5/(1162.5 + n \times 114)$. We plot in figure 6.4 the pH variation from this model by assuming that the non-purity of the powder comes only from the residual TFA. The best match for the pH jump is obtained when 1.95 molecules of TFA are attached to each peptide molecule (this leads to a purity of 84%, meaning that 0.84 mg of actual peptide is found in 1 mg of powder). However, the peptides were ordered crude and purity in that case are usually advertised between 60% and 80% by the fabricant. In addition to TFA traces, the crude powder is likely to contain solvents, other counter ions and salts from the

synthesis. In figure 6.4, we also reported the titration curve from our model that best matches the experimental data with a purity of 70%. This leads to a value of $n = 2.3$. In both case we see an excellent agreement between the model and the experimental data. This suggest that the eventual impurities are inert for the titration, as assumed in our model.

The value of $n \approx 2$ is also in agreement with the intuition that there is initially one TFA anion on each of the two lysine in the peptide [99]. The corresponding concentration of TFA is then $[\mathrm{T}]_0 \approx [\mathrm{T}^-] \approx 1\,\mathrm{mM}$, in agreement with what was used by Hwang et al. in [105] to develop their model. In section 6.4, we borrowed their model with the same value for $[\mathrm{T}]_0$. We show in figure 6.10 the surface charge density as a function of the pH, as obtained from the model described in section 6.4 and observe that the charge vanishes at pH of about 4. In the following experiments, we will use concentration $[\mathrm{NaOH}]_0$ between 0.65 and 1 mM to obtain pH between 3.5 and 4.

6.3.2 Kinetics

Resolving Kinetics Using Multiple Particle Tracking

We performed a time series of multiple tracking measurements as the self-assembly was occurring in the observed sample of KFE8 solution. For each time point during the gelation, we calculated the ensemble averaged mean-squared displacement $\langle \Delta x^2(\tau) \rangle$ as a function of the lag time τ to quantify the dynamics of the embedded Brownian probes. We report the results of this computation in figure 6.5 corresponding to amine coated beads of 1 μm diameter, in a solution of 0.1 wt% (1 mg/ml) KFE8 crude powder at pH=3.5 ($[\mathrm{NaOH}]_0 = 0.65\,\mathrm{mM}$). The times of gelation explored range from 2 min to 48 h. We observe in figure 6.5A that the dynamics of the particles is the one obtain in a purely viscous fluid ($\langle \Delta x^2(\tau) \rangle \propto \tau$, as indicated by the solid line in figure 6.5A) at the beginning of the gelation, when no solid network has been formed in the sample. This initial viscosity can be evaluated from the slope of $\langle \Delta x^2(\tau) \rangle = 2D\tau$ with $D = k_\mathrm{B}T/(6\pi a\eta)$, where k_B is the Boltzmann's constant, T the absolute temperature, η the viscosity of the fluid and a the particle radius. We find $\eta = 1.9\,\mathrm{mPa \cdot s}$, that is about twice the viscosity of water, at this early time of gelation. As the gelation occurs, the mean-squared displacement continuously decreases since the motion of the probes is progressively more constrained by the formation of fibers in their surrounding. At long time of gelation when the equilibrium state of the peptide system is reached (see later in the text), the mean-squared displacement is almost a constant plateau indicating that the fluid behaves as an elastic material at the frequencies presented here, from 0.1 to 10 Hz. At this point, the elastic modulus G is evaluated using $\langle \Delta x^2(\tau) \rangle = 2k_\mathrm{B}T/(6\pi aG)$. We find $G = 1\,\mathrm{Pa}$ indicating the presence of a weak gel, similar to what has been found using bulk rheology on similar system at comparable concentration [102].

To follow the kinetics, it is convenient to represent the evolution of the mean-squared displacement evaluated at a given lag time. In figure 6.5B we plotted the quantity $\langle \Delta x^2(\tau_i) \rangle$, evaluated at three lag times $\tau_1 = 0.1\,\mathrm{s}$, $\tau_2 = 0.5\,\mathrm{s}$ and $\tau_3 = 0.5\,\mathrm{s}$, as a function of the time of gelation t_gel. Also, in figure 6.5C we show the variation of the local power-law $\alpha(\tau_i)$ calculated at the same three lag times as a function of t_gel. The local power-law, or diffusive exponent, is defined by:

$$\alpha(\tau) = \frac{\mathrm{d}\big(\log\langle \Delta x^2(\tau) \rangle\big)}{\mathrm{d}\big(\log \tau\big)} \,. \tag{6.4}$$

We observe on these plots that both the mean-squared displacement and the diffusive exponent

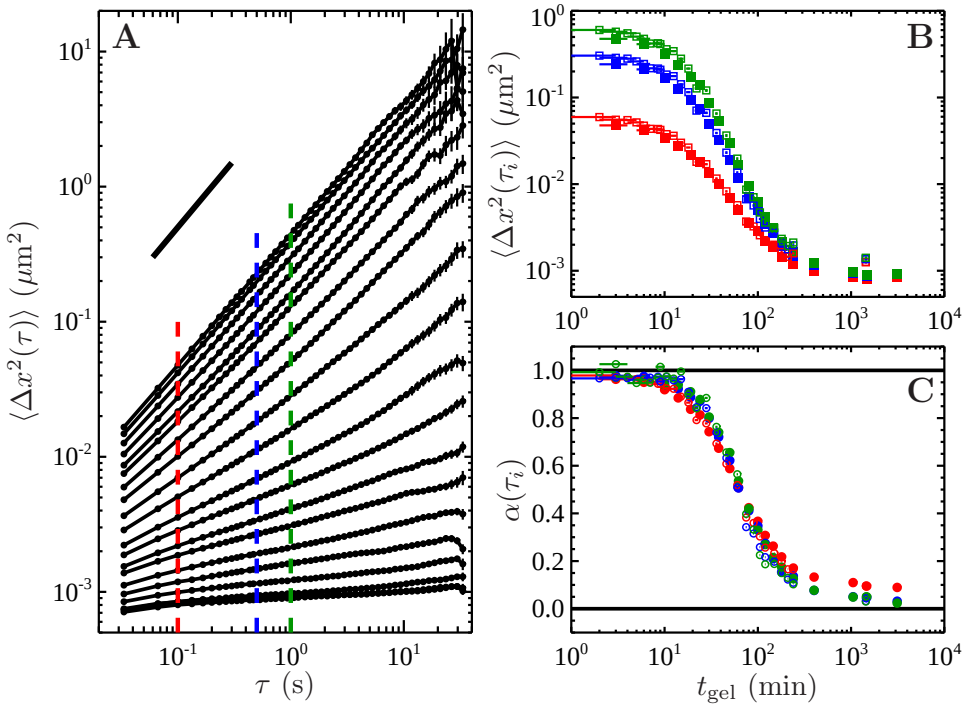

Fig. 6.5: Ensemble averaged mean-squared displacement $\langle \Delta x^2(\tau) \rangle$ of probes embedded in the self-assembling KFE8 system, reported at different time during gelation, from 2 min to 48 h. The concentration of powder is 0.1 wt% and the pH of the solution was set to 3.5. Particles are 1 μm diameter, amine coated, and carry a net positive charge at this pH. A) are the variation of $\langle \Delta x^2(\tau) \rangle$ versus τ for different times of gelation t_{gel}, with diminishing values for increasing t_{gel}. The solid black line indicates the scaling $\langle \Delta x^2(\tau) \rangle \propto \tau$. B) is the value $\langle \Delta x^2(\tau_i) \rangle$ at three lag times $\tau_i = 0.1$ (red), 0.5 (blue) and 1 s (green), versus t_{gel}. The solid symbols are extracted from A (as represented by the dashed lines of corresponding colors) and the open symbols are a reproducibility check. C) is the value of the local power-law $\alpha(\tau)$ of $\langle \Delta x^2(\tau) \rangle$ at the same lag times than B), with the same corresponding color coding. The solid black lines in C) indicate the limiting values 0 and 1 for $\alpha(\tau)$.

stagnate for gelation time greater than 4 h = 240 min, suggesting that the system has reached an equilibrium state. This characteristic time can be directly related to a characteristic time of structure formation apparent on the micrographs in figure 6.3. These experiments were performed at a lower pH (3.3), meaning that the gel formation kinetics is expected to be slower (see next section). However, we can presume from these figures that the gel has reached an equilibrium state at a time lying between 2 and 30 h.

Also, we observe on the curve presented in figure 6.5C that the local power-law values are

independent of the lag time at which it is calculated, for any time of gelation. By looking at the mean-squared displacement in figure 6.5A, we notice indeed that $\langle \Delta x^2(\tau) \rangle$ exhibit almost a pure power law dependence with τ over almost the entire range of accessible lag times. As noticed earlier, this power-law varies from 1 at the beginning of the self-assembly, indicating a purely viscous behavior, and reaches 0 at the equilibrium state of the gel indicating an purely elastic behavior on the accessible range of frequencies.

Finally, we validated our experimental protocol by reproducing under identical conditions these kinetics data in a separate experiment. In figures 6.5B and 6.5C, we have reported the result of this supplementary measurement with open symbols. We observe a good agreement between the two results, in terms of both the amplitude of $\langle \Delta x^2(\tau) \rangle$ and $\alpha(\tau)$ at various lag times, but also in their evolution with t_{gel}. However, we note that the last point of $\langle \Delta x^2(\tau) \rangle$ at $t_{\text{gel}} = 1500\,\text{min}$, characterizing the equilibrium state, differs by about 40% between the two experiments, indicating the sensitivity of this final state of the system to small variations, beyond control, in the experimental conditions.

Probes' Surface Chemistry and Size

Ideally, the measurement technique should not interfere with the self-assemby mechanism of gelation. Here, the probes particles could exhibit unwanted interaction with the assembly process. To characterize the effect of surface chemistry and size of the probe particles, we performed the experiment described above with another surface coating of the probes and a different size. First, we applied multiple particle tracking on $0.925\,\mu\text{m}$ diameter carboxylate probes in a solution of KFE8 powder at a concentration 0.1 wt% with a pH set at 3.5 (same as above). At this pH, carboxilate-modified probes are negatively charged whereas the amine-modified particles are positively charged. The peptide in solution at this pH being itself positively charged (see figure 6.10), we evaluate here the influence of an eventual interaction between the bead and the peptide. Moreover, this comparison is performed with similar particle size, so we truly isolate the effect of surface chemistry.

We present in figure 6.6 the kinetics results using these two different surface chemistries (red for amine and blue for carboxylate). Note that the mean-squared displacement values reported in figure 6.6A are scaled by the probes' radius a. We observe in this plot that the mean-squared displacement of the carboxylated particles (negatively charged) is in general smaller than the one exhibited by the amine-coated. This trend is consistent with other microrheological studies comparing the response of probes strongly and weakly attracted to their surrounding network [40, 41, 42]. We can hypothesize for example that the carboxylated beads are attached to the fibers through electrostatic attraction, connecting meshes and limiting locally the network fluctuations and hence their own motion. At the beginning of self assembly however, the scaled values are identical in the absence of a formed network. The amplitude of the difference between the mean-squared displacements obtained with these two chemistry is nevertheless small (the equilibrium values for t_{gel} are about 50% off, comparable to the discrepancy obtained in the reproducibility test), and the local power-law are almost identical at all time of gelation.

We also performed a kinetics study using $0.518\,\mu\text{m}$ diameter carboxylate modified probes which results are presented with the green points on figure 6.6. We observed that the scaled mean-squared displacements for these smaller beads, as well as the local power-law they exhibit, are collapsing with the ones exhibited by the bigger beads with the same carboxylate surface chemistry

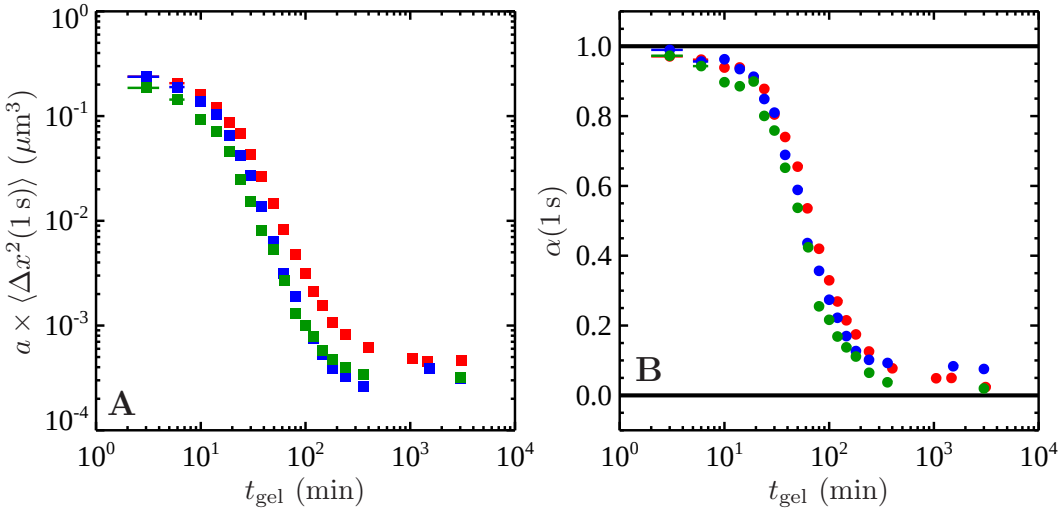

Fig. 6.6: Scaled mean-squared displacement $\langle \Delta x^2(\tau) \rangle$ (A) and local power-law $\alpha(\tau)$ (B) for particles embedded in the self-assembling KFE8 system as a function of self-assembly time t_{gel}. The lag time is $\tau = 1\,\mathrm{s}$. The points in red correspond to $1\,\mu$m diameter amine coated probes, the blue points are for $0.925\,\mu$m diameter carboxylate modified probes and the green points are for $0.518\,\mu$m diameter carboxylate modified particles. The solid black lines in B) indicates the limiting values 0 and 1 for $\alpha(\tau)$

(blue points). The independence of the quantity $a \times \langle \Delta x^2(\tau) \rangle$ with the probes radius suggests that the particles are probing a continuum environment at the lengths scale of their diameter (at least for $a > 0.5\,\mu$m). It is possible to apply the generalized Stokes-Einstein relation 1.4 to perform rheological measurements. Note that this is not in contradiction with some estimates of the averaged mesh size of a KFE8 system at similar concentration, calculated from AFM micrographs (see figure 6.3 for example) or electron micrographs of similar systems at comparable concentrations [95]. Also the similitude in the dynamics of probes bound and non-bound to the fiber matrix corroborate with the idea of a continuous network at the length scale of the probe.

We show in figure 6.7 the resulting rheological data obtain from the mean-squared displacements of the $0.925\,\mu$m diameter carboxylate modified particles. The storage and loss modulus were calculated using methods described in [37] and recalled by equation 3.35. We observed the qualitative behavior described in the previous section, that is the material is almost purely viscous at the beginning of the self-assembly, and its storage modulus progressively increase to become larger than the loss modulus, with a cross over at $t_{\mathrm{gel}} \approx 1\,\mathrm{h}$, meaning that the material is elastic. At time $t_{\mathrm{gel}} > 2\,\mathrm{h}$, the gels rheological properties remain steady.

We finally notice that for this section, all results were only presented at $\tau = 1\,\mathrm{s}$ and $\omega = 1\,\mathrm{Hz}$. However, we observe the same collapse of the kinetics data at other lag times, when changing the probes surface chemistry or diameter (data not shown).

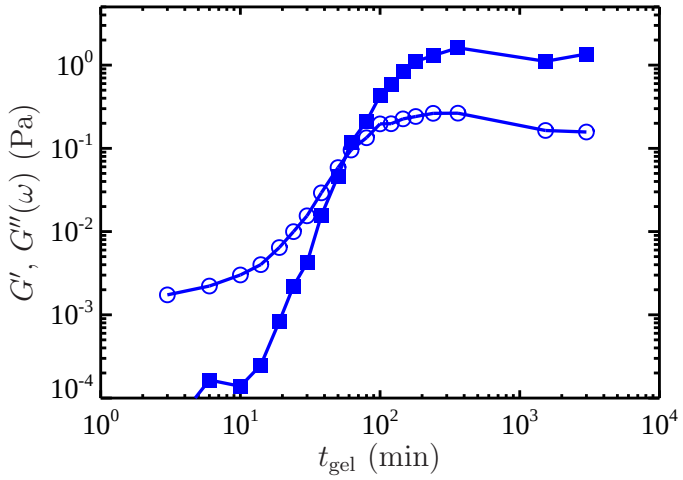

Fig. 6.7: Evolution of the storage modulus $G'(\omega)$ (solid squares) and of the loss modulus $G''(\omega)$ (open circles) as a function of the self-assembly time for a KFE8 powder solution with concentration 0.1 wt% and at a pH of 3.5. The values $G'(\omega)$ and $G''(\omega)$ were calculated the ensemble averaged mean-squared displacement of 0.925 μm diameter carboxylate modified particles at a frequency $\omega = 1$ Hz. Changing the size and the surface chemistry of the probes particle does not affect significantly these results.

6.3.3 Gelation Time and Gel Point

In this section we want to quantify the influence of the pH on the kinetics of gelation. Thus we must define a characteristic time of self-assembly that we can evaluate from the multiple particle tracking measurement. The critical gel point t^0_{gel} of the sol-gel transition of a gelling system is the first instant at which the connectivity of the network extend over the entire sample. The time at which G' and G'' crosses each other has been suggested to evaluate a characteristic time of gelation (see in figure 6.7). However in general, this crossover time depends on the frequency of excitation, preventing the definition of a single material parameter. A preferred way to detect the gel point is to use the time at which both $G'(\omega) \propto \omega^{\alpha_0}$ and $G''(\omega) \propto \omega^{\alpha_0}$ is observed over a wide range of frequencies [115, 116]. This power-law dependency is presumably related to the fractal scaling properties of the network clusters.

In our study we have access to a frequency range spanning two decades, $10\,\mathrm{Hz} < \omega < 0.1\,\mathrm{Hz}$, with a good statistical accuracy (see figure 6.5A). Over this range we observe that the mean-squared displacement exhibit a power-law behavior $\langle \Delta x^2(\tau) \rangle \propto \tau^{\alpha}$ at all time of gelation. Application of the generalized Stokes-Einstein relation 1.4 shows that in this case, both $G'(\omega) \propto \omega^{\alpha}$ and $G''(\omega) \propto \omega^{\alpha}$ over the corresponding range of frequencies. It is likely however that the system exhibit some relaxation dynamics which characteristic times lie outside this range at certain time of self-assembly, before and/or after the gel point. However, given the frequency window available

here, the gel point can not be determined using solely the criteria mentioned above. However we can postulate a characteristic value for α_0 to determine the critical gelation time. Using dynamic scaling based on percolation theory with the Rouse limit of hydrodynamic interactions, ones find $0.5 < \alpha_0 < 0.66$ [117]. The latter Rouse dynamics model with $\alpha_0 = 0.5$ has been very successful in describing rheology near the gel point [117, 118, 119, 120]. Such criteria allows the definition of the gel point $(t^0_{\rm gel}, G'_0 = G''_0)$ which in that case corresponds to the coordinates of the cross-over for $G'(\omega)$ and $G''(\omega)$ as seen in figure 6.7.

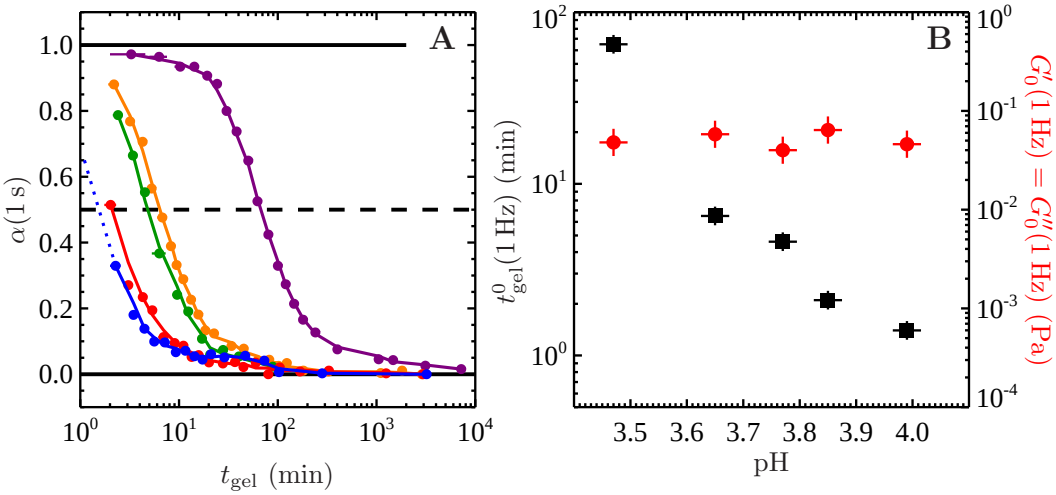

Fig. 6.8: Gelation kinetics of KFE8 powder solution with concentration 0.1 wt% as a function of the pH. A) is the local power-law of the mean-squared displacement at a lag time $\tau = 1\,\mathrm{s}$, plotted as a function of the gelation time $t_{\rm gel}$ for pH=3.5 (purple), 3.65 (orange), 3.75 (green), 3.85 (red) and 4 (blue). The critical gel point $t^0_{\rm gel}$ is uniquely obtained at $\alpha = \alpha_0 = 0.5$ as represented by the dashed line. B) gives the resulting $t^0_{\rm gel}$ (black squares) and $G'_0 = G''_0$ (red circles) as a function of the pH. All the quantities are evaluated at $\tau = 1\,\mathrm{s}$ and $\omega = 1\,\mathrm{Hz}$.

In figure 6.8 we present the results for the critical gel point time as a function of the pH for a KFE8 powder solution with concentration 0.1 wt%. We performed this multiple particle tracking measurements using $1\,\mu$m diameter amine coated probes, and with concentration of $[\mathrm{NaOH}]_0$ between 0.65 and 1 mM. The values of $t^0_{\rm gel}$ for each pH were extracted from the evolution of the local power-law α with the gelation process, as presented in figure 6.8A, and using the criteria $\alpha = \alpha_0 = 0.5$ to define the gel point. We observe that the self-assembly is faster as the pH increases. For an elevation of pH from 3.5 to 4, the gel time is increased by almost two fold, from $\sim 1\,\mathrm{min}$ to $\sim 70\,\mathrm{min}$. The two fold amplitude of variation is fairly independent of the choice of α_0 for the gel point criteria in the viscoelastic region $0.2 < \alpha_0 < 0.8$, meaning that another choice of α_0 (say $\alpha_0 = 0.66$) would lead to values of $t^0_{\rm gel}$ scaled by a constant factor as compared to the one in figure 6.8B.

We also report in figure 6.8B the evolution of the characteristic elastic modulus $G'_0 = G''_0$ at the gel point characterized by cross-over between the elastic and viscous behavior. We observe that, even though the kinetics is dramatically changed by the raise of pH, the mechanical properties are not significantly affected by the pH at the gel point. Note that the range of modulus reported on figure 6.8B, from 10^{-4} to 1 Pa is the same as the range observed from the beginning to the final equilibrium state of gelation (see figure 6.7).

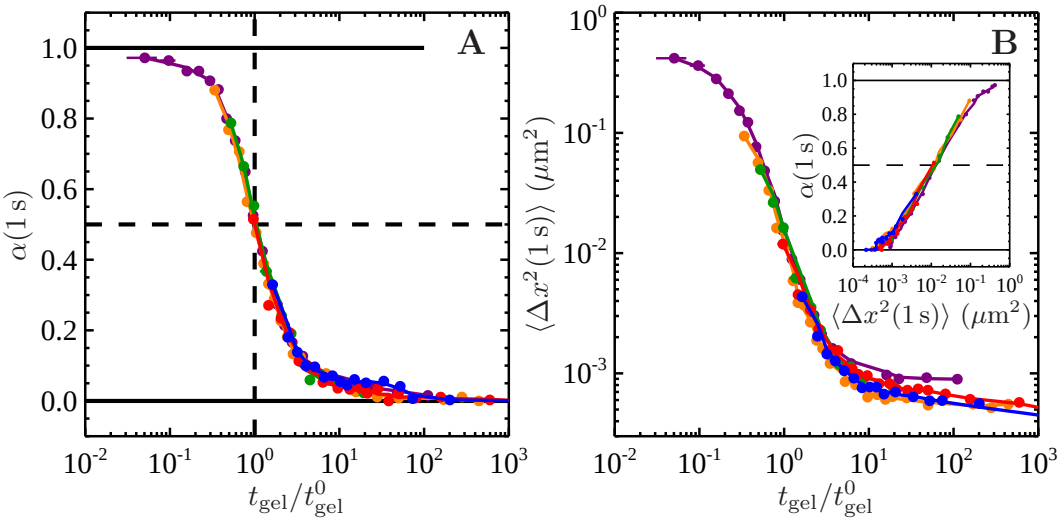

Fig. 6.9: Evolution of the mean-squared displacement's local power law and magnitude as a function of the scaled gelation time. A) are the same results as presented in figure 6.8A (the same colors are used to distinguish the pH of the experiments), but the gelation time t_{gel} has been scaled by the gel point time t^0_{gel} obtained at the corresponding pH for each curve. B) is the value of the mean-squared displacement as a function of the gelation time scaled the same way as in A). The inset in B) shows the evolution of the local power-law versus the magnitude of the mean-squared displacement.All the quantities presented here are evaluated at $\tau = 1\,\mathrm{s}$.

This observation suggests that in this range of pH, the self-assembly as probed by particle tracking undergoes an identical state, independent of the pH, at the gel point. We can extend this observation by presenting the kinetics measurements scaled by the characteristic gel time t^0_{gel} extracted from figure 6.8. In figure 6.9 we present the evolution of $\alpha(1\,\mathrm{s})$ and $\langle\Delta x^2(1\,\mathrm{s})\rangle$ as a function of $t_{\mathrm{gel}}/t^0_{\mathrm{gel}}$ for each value of pH. We observe a remarkable overlap of the various curve obtained for these two quantities, $\alpha(1\,\mathrm{s})$ and $\langle\Delta x^2(1\,\mathrm{s})\rangle$. The scatter of the points at late gelation time, $t_{\mathrm{gel}}/t^0_{\mathrm{gel}} > 10^1$ is within the reproducibility control presented in figure 6.5 for the equilibrium state. This time self-similarity strongly suggest that the increase of the pH from 3.5 to 4.0 does not affect the mechanism followed by the self-assembling peptide to form the hydrogel. This observation will be the basis of the gelation model presented in the next section. The inset of figure 6.9B resumes

this self-similarity in the observable parameter space $(\alpha, \langle \Delta x^2 \rangle)$ at a lag time $\tau = 1\,\mathrm{s}$, but the same results holds for other lag times investigated in this study (data not shown).

6.4 Discussion

Using the mean-squared displacement measurements from the multiple particle tracking of Brownian probes, we have calculated the ensemble averaged mean-squared displacement of the probes as an observable quantity to follow the gelation of KFE8 self-assembling peptide system. Using a rheological criteria to define a characteristic time of gelation, it is possible to evaluate the influence of pH of the solution on the kinetics of self-assembly of KFE8. This unique new insight should be brought into context by comparing to the work of Caplan et al. [99] and extending their analysis.

6.4.1 New Insight in the Self-Assembly

In their study of KFE8, or of very similar self-assembling peptides consisting of a few repeat of the sequence FKFE, Caplan et al. assessed the influence of the pH and salt concentration on the state of the system [99, 107]. Presumably, this state was an equilibrium or a pseudo-equilibrium state of the system. Using bulk rheological measurements to classify the self-assembling peptides as a viscous solution or as an elastic gel, they found the region of pH where the transition sol-gel of the system occur. They also investigated the influence of salt concentration by measuring the critical coagulation concentration (CCC) of NaCl, above which the transition sol-gel takes place [121].

Here we perform a thorough characterization of the kinetics of self-assembly. The multiple-particle tracking microrheology technique provides a 2 min temporal resolution in characterizing the fluid's state, limited by the movie acquisition time. The method is non-invasive and weakly influences the self-assembly process. We have been able to resolve fine variation in the rheological properties of the weak gel. In particular, we show that a finite time of gelation can be extracted for a pH at which the peptide is believed to be positively charged. This does not however contradict the bulk rheology measurements performed by Caplan et al., who assumed a binary state of the system (solution or gel) limited by the poor detection level offered by the bulk rheology technique, as well as the experimental challenges encountered when trying to characterize intermediate states.

In a subsequent section we develop a quantitative model of peptide interaction to tentatively explain the variation of the kinetics of gelation with the pH, as resolved using multiple particle tracking microrheology. We use a model of interaction given in terms of the Derjaguin-Landau-Verwey-Overbeek (DLVO) theory, as suggested in a previous study by Caplan et al. [99].

6.4.2 Peptides' Structure at Early State of Self-Assembly

In section 6.3.2 we calculated the viscosity of the peptide KFE8 solution at the beginning of gelation for a pH of 3.5. Moreover, we have seen in figure 6.6 that the mean-squared displacements of probes with sizes and chemistries were overlapping when scaled by the particles' radius, indicating that the medium is seen as a continuum at the various length scales investigated. The viscosity has been found to be twice the viscosity of the aqueous solvent in which the peptide powder is mixed.

From the figure 6.3a and 6.3b, we assume that the earlier state of the peptide mixture is a monodisperse solution of peptide ribbons that we model as a cylinder with radius $R = 4\,\mathrm{nm}$ (see figure 6.2), and which length L can be related to the number n of peptide molecules per ribbons segment. One turn of the helix contains about 100 KFE8 molecules and is about 20 nm long

[105]. That is we have $L = n \times 0.2\,\mathrm{nm}$. The zero-shear reduced viscosity of a dilute monodisperse dispersion of Brownian rigid cylindrical rods is given by [122]:

$$\frac{\eta - \eta_0}{\eta_0} = \frac{2\phi\lambda^2}{45 \ln \lambda}\left[\frac{\ln\lambda + 0.64}{\ln\lambda - 1.5} + \frac{1.659}{(\ln\lambda)^2}\right] \tag{6.5}$$

where η and η_0 are the dispersion and solvent viscosity respectively, ϕ is the volume fraction of rods and $\lambda = L/R$ is the cylinder's aspect ratio. With $\phi = \pi R^2 L c_0$, where $c_0 = n^{-1} \times 4 \times 10^{23}\,\mathrm{m}^{-3}$ is the concentration of rods as obtained with 80% purity of a 0.1wt% KFE8 powder disolved in the solvent, we get $\phi = 4 \times 10^{-3}$. Solving equation 6.5 for n with $(\eta - \eta_0)/\eta_0 = 1$, we find $n \approx 2000$, corresponding to earlier ribbons of about 20 helical turns long (i.e. $L \approx 400\,\mathrm{nm}$). Note that we can count about 10 helical turns per precursor ribbon on the AFM micrograph of figure 6.3a, obtained with the same concentration of peptides powder, after 8 min of self-assembly (although the peptide powder mixing protocol was significantly shorter), and at a pH$\sim$3.3 [98].

6.4.3 Derjaguin-Landau-Verwey-Overbeek (DLVO) theory

To model the interaction driving the self-assembly of the peptide KFE8, we must assume a geometry for the elementary coalescing blocks. In a simplified model, we assume that the β-sheet formed by the peptides is a semi-infinite block with a given surface s of interaction by which two identical blocks could eventually connect. This geometry has already been used on the same system by Hwang et al. [105] to develop their model of peptide surface charge in term of the electrostatic double layer theory. By looking at the AFM micrographs in figure 6.3, we assume that the early short β-sheet fibers are somewhat represented by these blocks of material. As this choice might not be the most advanced, the resulting theory remains however fairly simple, and allows us to calculate reasonable orders of magnitude for the interaction. Another choice of geometry investigated here is to model the building blocks as infinitely long cylinder with radius R. The geometry presumably describes the building blocks more accurately when comparing with AFM micrographs of figure 6.3 obtained at early times of gelation.

Electrostatic Double Layer Model

In the electrostatic double layer model, the charged blocks are bathed in a solution of ions. To express the electrostatic potential ψ, we write the Poisson-Boltzmann equation [1, 121]:

$$\nabla^2\psi = -\rho/\epsilon = -\epsilon^{-1}\textstyle\sum_{i=1}^{N} z_i e n_i^0 e^{-ez_i\psi/(k_\mathrm{B}T)} \tag{6.6}$$

where ρ is the charge density in the system (expressed in $\mathrm{C}\cdot\mathrm{m}^{-3}$), $\epsilon = \epsilon_r\epsilon_0$ with ϵ_r and ϵ_0 the dielectric constant of water ($\sim$ 80) and the permittivity of vacuum respectively, and n_i and z_i are respectively the concentrations (in m^{-3}) and valencies of the n different ions in the solution. Returning to the model of titration presented in section 6.3.1, we consider the following relevant concentration in the bulk solution: $[\mathrm{Na}^+]$, $[\mathrm{H}^+]$, $[\mathrm{T}^-]$ and $[\mathrm{OH}^-]$. By using the charge neutrality in the bath, $[\mathrm{Na}^+] + [\mathrm{H}^+] = [\mathrm{T}^-] + [\mathrm{OH}^-]$, we can rewrite the Poisson-Boltzmann equation:

$$\nabla^2\psi = 2\epsilon^{-1}e\big([\mathrm{OH}^-] + [\mathrm{T}^-]\big)\sinh\big[e\psi/(k_\mathrm{B}T)\big] = 2\epsilon^{-1}ec\sinh\big[e\psi/(k_\mathrm{B}T)\big] \tag{6.7}$$

as obtained in a symmetrical 1:1 electrolyte with ions concentration $c = [\mathrm{OH}^-] + [\mathrm{T}^-]$ (expressed in m^{-3}). In our case c depends on the pH through $c = 10^{\mathrm{pH}-14} + [\mathrm{T}^-]$ where $[\mathrm{T}^-] = [\mathrm{T}]_0\big(1 + 10^{\mathrm{pK_T}-\mathrm{pH}}\big)^{-1}$ (see section 6.3.1). The equation 6.7 can be written:

$$\nabla^2\tilde{\psi} = \kappa^2 \sinh\tilde{\psi} \tag{6.8}$$

where $\tilde{\psi} = e\psi/(k_\mathrm{B}T)$ is the scaled potential and $\kappa = \sqrt{2e^2c\epsilon^{-1}/(k_\mathrm{B}T)}$ is the Debye-Huckel parameter.

To calculate the boundary condition ψ_s of the electrostatic potential at the surface, Hwang et al. [105] used the chemical equilibrium condition at the surface of the β-sheet [1]. They expressed the dissociation constant of the glutamic acid EH and of the Lysine KH^+ by:

$$K_\mathrm{E} = \frac{[\mathrm{E}^-]_s[\mathrm{H}^+]_s}{[\mathrm{EH}]_s} = 10^{-\mathrm{pK_E}} \quad \text{and} \quad K_\mathrm{K} = \frac{[\mathrm{K}]_s[\mathrm{H}^+]_s}{[\mathrm{KH}^+]_s} = 10^{-\mathrm{pK_K}} \tag{6.9}$$

where the subscript s indicates surface concentrations. Comparing to the bulk model presented in section 6.3.1, we recall here that the surface model presented now is a local model. To this regard, the pK values corresponding to these surface dissociation constants are now the standard value, $\mathrm{pK_E} = 4.3$ and $\mathrm{pK_K} = 10.8$ [113] of the isolated amino acids [114]. Also, the surface concentration $[\mathrm{H}^+]_s$ is related to the bulk concentration $[\mathrm{H}^+]$ using the Boltzmann relation expressed at the surface $[\mathrm{H}^+]_s = [\mathrm{H}^+]e^{-e\psi_s/(k_\mathrm{B}T)}$. The total surface charge density is then calculated the following way:

$$\sigma = \frac{\sigma_\mathrm{E}^\mathrm{max}[\mathrm{E}^-]_s}{[\mathrm{EH}]_s + [\mathrm{E}^-]_s} + \frac{\sigma_\mathrm{K}^\mathrm{max}[\mathrm{KH}^+]_s}{[\mathrm{KH}^+]_s + [\mathrm{K}]_s} \tag{6.10}$$

where $-\sigma_\mathrm{E}^\mathrm{max} = \sigma_\mathrm{K}^\mathrm{max} = \sigma^\mathrm{max} = 0.26\,\mathrm{C/m^2}$ are the maximum possible surface charge of the glutamic acid and lysine calculated from the dimensions of the KFE8 molecule. Namely, there are two negative groups from the molecules E that are exposed to the side face of the molecule, with area $3.1 \times 0.4\,\mathrm{nm}^2$ (see figure 6.1). Combining the equations 6.9 and 6.10 we can write:

$$\frac{\tilde{\sigma}}{\tilde{\sigma}^\mathrm{max}} = -\frac{10^{\mathrm{pH}-\mathrm{pK_E}}}{e^{-\tilde{\psi}_s} + 10^{\mathrm{pH}-\mathrm{pK_E}}} + \frac{e^{-\tilde{\psi}_s}}{e^{-\tilde{\psi}_s} + 10^{\mathrm{pH}-\mathrm{pK_K}}} \tag{6.11}$$

where $\tilde{\sigma} = e\sigma/(\epsilon\kappa k_\mathrm{B}T)$ is the scaled surface charge density. The latter can be related to the electrostatic potential at the surface by solving equation 6.8. For the planar geometry, we have [1, 121]:

$$\tilde{\sigma} = 2\sinh(\tilde{\psi}_s/2) \tag{6.12}$$

whereas for the cylindrical geometry we have [123]:

$$\tilde{\sigma} = 2\sinh(\tilde{\psi}_s/2)\left[1 + \frac{K_1^2(\kappa R)/K_0^2(\kappa R) - 1}{\cosh^2(\tilde{\psi}_s/4)}\right]^{1/2} \tag{6.13}$$

where K_n is the modified Bessel function of the second kind of order n. For this cylindrical geometry that represents the initial ribbons represented in figure 6.2, we suppose that the surface charge is uniformly distributed over the entire cylinder area. In that case 100 molecules constitutes a cylinder of radius 3.5 nm and of length 20 nm (see figure 6.2) and we find that σ^max is reduced

to $0.26 \times 100 \times 0.4 \times 3.1/(\pi \times 20 \times 3.5) 0.15\,\mathrm{C/m^2}$. Note also that equations 6.12 and 6.13 are *not* obtained from a linearized Poisson-Boltzmann (obtained for $\tilde{\psi} \ll 1$). Although equation 6.13 is strictly valid for $\kappa R \gg 1$, it has been shown that it returns precise results even when $\kappa R \sim 1$ [123]. Notably, we will see that these remarks are important for the model used here, as we find that both $\tilde{\psi} > 1$ and $\kappa R \sim 1$ at the pH investigated.

Equations 6.12 and 6.13, in conjunction with equation 6.11, can be used to calculate σ and ψ_s at every pH value for both geometries. The result for the surface charge density as a function of the pH are given in figure 6.10 with a TFA concentration $[\mathrm{T}]_0 = 10^{-3}\mathrm{M}$ (see section 6.3.1).

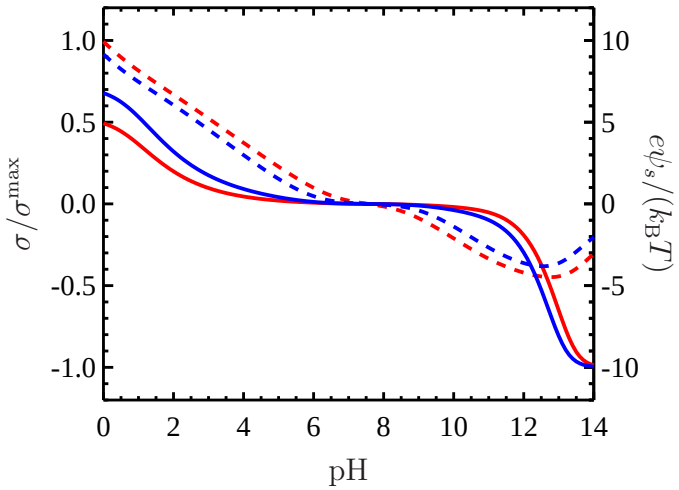

Fig. 6.10: Surface charge density σ of the peptides for $[\mathrm{T}]_0 = 10^{-3}\mathrm{M}$ as a function of the pH of the bath solution for both plane and cylindrical geometries. The red curves describe the plane geometry with $\sigma^{\max} = 0.26\,\mathrm{C/m^2}$ whereas the blue curves describe a cylindrical geometry with radius $R = 3.5\,\mathrm{nm}$ and $\sigma^{\max} = 0.15\,\mathrm{C/m^2}$ (see text). The solid lines represent the surface charge density $\sigma/\sigma^{\max}$ and the dashed lines are for the surface potential $\tilde{\psi}_s = e\psi_s/(k_\mathrm{B}T)$. The window of pH observed in this study is $3.5 < \mathrm{pH} < 4$.

We see on figure 6.10 that the peptide is positively charged for $pH \lesssim 4$ and negatively charged for $\mathrm{pH} \gtrsim 11$. In these domains of pH, we expect that the electrostatic repulsion between the peptides slows down the self-assembly process. The bulk rheology measurements would conclude to a non-elastic state of the material, even at limiting values $\mathrm{pH} \sim 4$ and pH 11, unless the sample is assessed after a prohibitively long equilibration time. This observation is in agreement with the rheology results obtained by Caplan et al. with the peptide KFE12 [107], that would share the same theoretical curve as the one presented on figure 6.10 (for KFE12, we would find $[\mathrm{T}]_0 \approx 1.5 \times 10^{-3}\mathrm{M}$, but this difference with figure 6.10 does not affect significantly the curve). To gain more insight into the kinetics of self-assembly experimentally observed here around a pH of 4, we need to compare the electrostatic repulsion force describe here with the attractive interaction between peptides.

Interaction Potential

From the previous section we have a description of the electrostatic repulsion between two identical blocks. We will use a van der Waals interaction potential to describe the attractive component of the blocks' interaction. It is certain that many forces are driving the self assembly. The hydrophobic bond is usually the dominant one, and it has been shown through simulation that they contribute to the short time association of peptides in the initial β-sheet [108]. The hydrogen bonds are likely to ensure the cohesion of the blocks and are responsible for the peculiar helical shape of the β-sheet. The van der Waals dispersion forces are long range and are usually the ones responsible for bringing the molecules together [1, 124]. Such a model has been used by Girgsby et al. [125] for poly-L-lysine peptide, in which they also included short range specific interaction (e.g. hydrophobic bonds), that are discarded here.

The potential of net interaction of two blocks of material separated by a distance d and with a characteristic surface s of interaction is given by [1, 121]:

$$\frac{U_{\mathrm{DLVO}}(d)}{k_{\mathrm{B}}T} = \frac{4sc}{\kappa}\Psi_s^2 e^{-\kappa d} - \frac{sA}{12\pi d^2} \tag{6.14}$$

where A is the Hamaker constant, taken to be $A = 5k_{\mathrm{B}}T$ for proteins in aqueous solutions [126, 127, 128], and $\kappa^{-1} = 10\,\mathrm{nm}$ is the Debye length characterizing the range of the electrostatic repulsion. Here the effective potential Ψ_s is given by $\Psi_s = 4\tanh(\tilde{\psi}_s/4)$.

For the other geometry considered in the previous section, we write the interaction between two crossed cylinders with perpendicular axis [123]:

$$\frac{U_{\mathrm{DLVO}}(d)}{k_{\mathrm{B}}T} = \frac{4\pi^2 ce^{-2\kappa R}}{\kappa^3 K_0^2(\kappa R)}\Psi_s^2 e^{-\kappa d} - \frac{AR}{6d} \tag{6.15}$$

with the following expression for the effective potential at the surface:

$$\Psi_s = \frac{8\tanh(\tilde{\psi}_s/4)}{1 + \left[1 - (1 - K_0^2(\kappa R)/K_1^2(\kappa R))\tanh^2(\tilde{\psi}_s/4)\right]^{1/2}} \tag{6.16}$$

The Debye length is bigger than the typical radius (3.5 nm) of the cross-section of the KFE8 double-layer ribbon (see figure 6.2). In figure 6.11 we plot the interaction potential given by equation 6.14 in the planar geometry at various pH, and for $s = 10\,\mathrm{nm}^2$ and $s = 100\,\mathrm{nm}^2$ corresponding respectively to dimensions of $\sim 3 \times 3\,\mathrm{nm}$ and $\sim 10 \times 10\,\mathrm{nm}$ for the surface of blocks' interaction. This last characteristic size of 10 nm is intended to include the electrostatic layer on the side of the β-sheet and thus to account for edge effects in a admittedly ad hoc, but analytically tractable manner.

We observe on this figure that the potential barrier value is decreasing as the pH increases from 3 to 7, as expected from the corresponding decrease of the surface charge density σ on the interacting blocks (see figure 6.10). At pH > 6, we observe that $U_{\mathrm{DLVO}}^{\max} < k_{\mathrm{B}}T$, meaning that the potential barrier is not significant and that the block monomers can easily assemble. In that case, the system is expected to quickly flocculate and form a stable network, as seen experimentally [99]. We need however to gain some more insights on the gelation kinetics by building some time scales from this model interaction potential of the blocks.

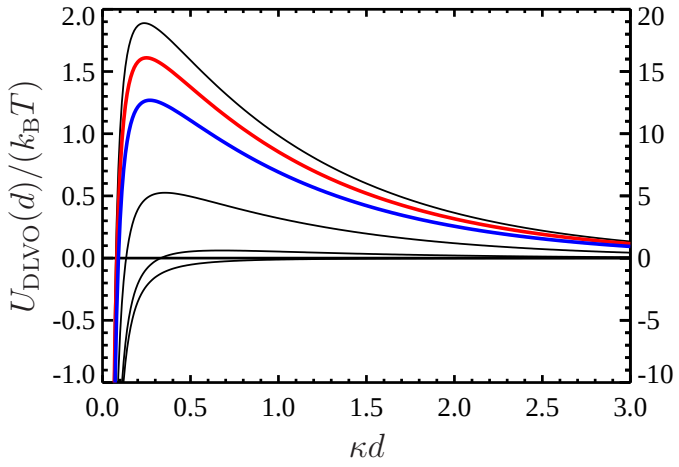

Fig. 6.11: DLVO interaction potential for pH=3.5 (red) and pH=4 (blue) in the planar geometry. The thin black lines are for pH=3, 4, 5, 6 and 7, from the top to the bottom line. The left axis is for a characteristic surface of interaction $s = 10\,\mathrm{nm}^2$, whereas the right axis is for $s = 100\,\mathrm{nm}^2$.

Figure 6.12 shows the DLVO interaction potential given by equation 6.15 for two charge cylinders. On the figure, we observe the same qualitative behavior as in the other DLVO plots obtained in the planar geometry (figure 6.11). Although the drop of the potential barrier is more drastic then in the plane interaction when increasing the pH from 3.5 to 4 (and note that the potential is purely attractive at pH=6), the magnitude of this barrier is significantly higher. This indicates that the model is highly sensitive to the geometry considered for the building blocks. We can connect the drop in the potential barrier with the decrease of time scales of gelation using a Kramers' type relation, $t \propto e^{E/(k_{\mathrm{B}}T}$ where t is the characteristic time of reaction and E is the potential barrier. To obtain a decrease of a factor ~ 50 in t (as observed on figure 6.8), a drop of $\sim 4k_{\mathrm{B}}T$ should be observe for the barrier potential when increasing the pH from 3.5 to 4. In our case, the planar geometry provides more realistic magnitudes for the decrease in the potential barrier when increasing the pH from 3.5 to 4, and we will consider only this choice in the following discussion where we provide a more detailed analysis of the time scales of gelation.

Time Scales

From the interaction potential given above it is possible to extract some time scale of network growth using colloidal aggregation theories. The characteristic Brownian aggregation time when considering a diffusion limited aggregation of non-interacting (except at contact) monomers is given by [2]:

$$t_{\mathrm{B}} = \frac{3\eta}{4k_{\mathrm{B}}Tc_0} \tag{6.17}$$

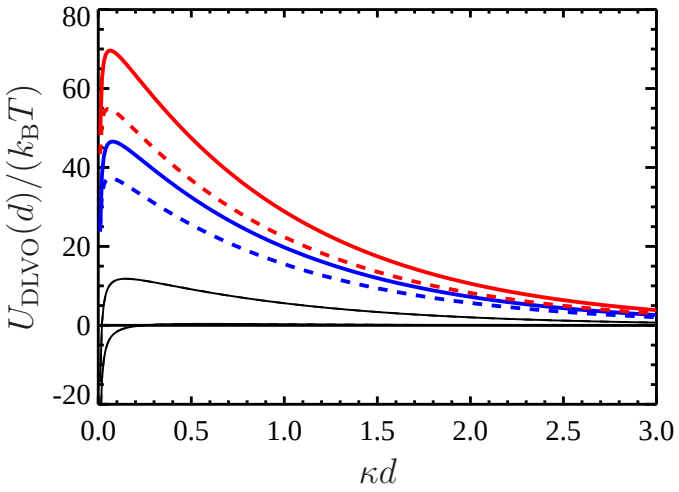

Fig. 6.12: DLVO interaction potential and for pH=3.5 (red) and pH=4 (blue) in the cylindrical geometry. The thin black lines are for pH=5 and 6. The solid lines are for a cylinder with radius $R = 3.5\,\mathrm{nm}$ corresponding to the model of KFE8 helical ribbon presented in figure 6.2, and the dashed lines is for a radius $R = 2\,\mathrm{nm}$. Solid and dashed black lines overlap to be indistinguishable.

where η is the viscosity of the solvent, and c_0 is the initial concentration of monomer. By using $\eta = 1\,\mathrm{mPa}\cdot\mathrm{s}$ the viscosity and $c_0 = n^{-1} \times 4 \times 10^{23}\,\mathrm{m}^{-3}$ as obtained with 80% purity of a 0.1wt% KFE8 powder disolved in water, where n is the number of peptide per initial β-sheet structure modeled by the block monomer, we obtain $t_{\mathrm{B}} \approx n \times 10^{-7}\,\mathrm{s}$. This time is interpreted as the characteristic time to form dimer from non-interacting monomer. We note at this point that our model includes now two parameters, s and n characterizing the geometry of the block monomer to model the β-sheets.

To account for the potential of interaction between monomer, we can use the Fuchs stability factor W to write [2]

$$t_{\mathrm{DLVO}} = t_{\mathrm{B}} \times W \quad \text{with} \quad W = 2d_{\max} \int_{d_{\max}}^{\infty} e^{U_{\mathrm{DLVO}}(x)/(k_{\mathrm{B}}T)} \frac{\mathrm{d}x}{x^2} \tag{6.18}$$

where $d_{\max}$ is the distance between monomer at which the interaction potential is maximum. With our model, t_{DLVO} is a characteristic time of fiber growth. Equation 6.18 was derived for a spherical geometry of the interaction between monomer, whereas our model assumes interactions between edges of the blocks to obtain a linear fiber growth. However as a first approximation, we expect this time to be correlated to the critical gel point time, t^0_{gel} measured experimentally in this study, and defined as the characteristic time at which the self-assembly first percolates the entire sample, and thus tightly related to the dynamics of growth of the structuring element. Moreover, the growth

of fibers of a similar self-assembling system has already been paralleled to the bulk rheological properties of the system in a recent study [129].

As observed on figure 6.8, t^0_{gel} undergoes a two fold increase as the pH is reduced from 4 to 3.5. The amplitude of this variation is fairly independent of the choice of α_0 for the gel point criteria in the viscoelastic region $0.2 < \alpha_0 < 0.8$. By assuming $t_{\text{DLVO}} \propto t^0_{\text{gel}}$, we thus expect to have $W_{\text{pH=3.5}}/W_{\text{pH=4}} \sim 100$. The integral in equation 6.18 can be numerically evaluated using the expression of $U_{\text{DLVO}}(d)$ from equation 6.14. We find $W_{\text{pH=3.5}}/W_{\text{pH=4}} = 1.3$ for $s = 10\,\text{nm}^2$ and $W_{\text{pH=3.5}}/W_{\text{pH=4}} = 30$ for $s = 100\,\text{nm}^2$. This suggests that the geometry of the block for the model should include the Debye-Huckel side layer when considering the surface section connecting the blocks.

For this surface of interaction $s = 100\,\text{nm}^2$, we calculate $W(\text{pH} = 3.5) = 6 \times 10^6$, which leads to $t_{\text{DLVO}} \approx n \times 1\,\text{s}$. One turn of the helix contains about 100 KFE8 molecules [105], that is we take $n \approx 100$. This leads to $t_{\text{DLVO}} \sim 1\,\text{min}$ which is the right order of magnitude for the system's gelation at this pH, assuming the concentration of monomer is negligible after $100 \times t_{\text{DLVO}}$, and that the gel point is reached at this instant.

The geometry factors s and n used in this model have the following effects: increasing s tends to sharpen the drop of t_{DLVO} when increasing the pH, by increasing more the time t_{DLVO} at small pH than the one at large pH; increasing n, the initial size of the block induces a uniform increase of t_{DLVO} over the whole range of pH. The order of magnitudes obtained here for s and n are however realistic.

6.5 Conclusion

We have used multiple particle tracking to assess the kinetics of formation of a self-assembling peptide system. The temporal resolution, as well as the high sensitivity of the technique to variation of the mechanical properties of weak gels allowed us to follow the system's characteristic time of gelation as a function of the pH of the peptide solution. This assessment is impossible to reach with classical bulk rheology technique. However it has important consequences on the understanding of amyloid fibrils formation [109]. We also presented a quantitative simple model of self-assembly formation that yields realistic estimations of time of gelation.

CHAPTER 7

Conclusions and Outlook

7.1 Conclusions

In this thesis we have characterized, improved and used an experimental technique that assess the micromechanics of biopolymer solutions. The method consists of measuring the thermal motion of micron-sized probe particles embedded in the biomaterials. Multiple particle tracking measurements are performed using a standard fluorescent video microscopy setup. Many of the advantages of this passive technique has been outlined in chapter 1 and 2: weak stresses are applied on the material, preventing the fragile microstructures from being disrupted; small sample volumes are used so that the environment (temperature, pH, concentration of chemicals) of the sample can be quickly and easily changed; measurements are fast and non-invasive so that temporal evolution of the material can be followed in real-time. Moreover, multiple particle tracking offers access to a wide range of time scales to follow out-of-equilibrium systems that exhibit kinetics ranging from a few seconds to several days.

In chapters 3 and 4 we have developed general models to account for localization errors in the tracking. We classified the cause of these errors into two different sources. Because of the inherent noise in the fluorescent video microscopy setup, multiple particle tracking suffers a low spatial resolution in the probes position estimation as compared to other single particle tracking technique, leading to significant inaccuracy in the mechanical measurements. We have proved that this apparent constraint can be successfully corrected on the average properties extracted with this technique, such as the mean-squared displacement and the rheological properties. Another source of errors arising in multiple particle tracking measurements comes from the finite exposure time required during the video acquisition of the particle motion. We developed a novel theoretical

model to quantify for this second type of errors and we investigated the effect of these errors on microrheology measurements of fluids in which an embedded particle's mean squared displacement displays a plateau above a certain onset time. Using common viscoelastic models, we find that the exposure time has a great effect on the measured mean squared displacement.

The correction methods and the theoretical predictions mentioned above are general results that apply to the averaged quantities extracted from any kind of particle tracking experiment. These groundwork studies should widen the range of possible applications of particle tracking, and to help interpreting particle tracking measurements.

A unique feature of the tracking technique we used here is its ability to track simultaneously hundreds of particle dispersed at different locations in the sampled medium. Each particle probes its local environment that is reported by the individual mean-squared displacement of the particles. Thus, systems that are heterogeneous at length scales larger than the probe size will be characterized by the different values of the mean-squared displacement as reported by each particles at each of their location. Calculating the moments of the distribution of these individual mean-squared displacement provide a quantification of the related property (local viscosity, pore size, local elastic modulus, ...) distribution in the material. However, when a mean-squared displacement is experimentally extracted from a single trajectory, statistical accuracy is degraded by the finite duration of the tracking that can differ from one particle to the other. Thus different measured mean-squared displacements can also be obtained in strictly homogeneous system because of poor statistics. In chapter 5 we developed and experimentally verified a theoretical way to decouple this statistical inaccuracy from an actual medium heterogeneity, by fully characterizing the peculiar statistical sampling design of the technique. In particular, the ability of the technique to efficiently probe a certain fluid has been quantified in terms of a transparency factor, characterizing the degree of possible assessment of the given fluid by the technique. Estimates for mean and variance of the probes dynamics in a heterogeneous material were derived, and we showed how these measurements are irremediably biased if some part of the probed fluid are transparent to particle tracking. We noted that this is a strong weakness of this technique. Further theoretical studies should be performed to establish a criteria of statistical validity of a given measurement in an heterogeneous system. Nevertheless, these new statistical tools allow the extraction of a maximum information from multiple particle tracking measurements, that will serve the assessment of heterogeneity in a complex material. This is expected to be particularly important for the study of biomaterials properties and functions.

Overall, this technique is well suited to studying sensitive, expensive and time-evolving complex biomaterials, for which micrometer scale properties can play a central role in biological mechanisms. An interesting class of biomaterials is called self-assembling peptides. These systems have been recently developed from the self-assembly of custom designed oligo-peptides that form a polymeric network. The latter serves as a scaffold for 3D cell culture. Also, these peptides serve as a model system for biological self-assembly that share important similarities with processes involved in protein conformational diseases. These observations constitute the framework that motivates the study presented in chapter 6. We have used multiple particle tracking to assess the kinetics of formation of a self-assembling peptide system. The temporal resolution, as well as the high sensitivity of the technique to variation of the mechanical properties of weak gels allowed us to follow the system's characteristic time of gelation as a function of the pH of the peptide solution. This assessment is impossible to reach with classical bulk rheology technique. However it has important consequences on the applications mentioned above. Moreover, it allowed us to develop

a refined quantitative model of self-assembly formation in terms of the Derjaguin-Landau-Verwey-Overbeek (DLVO). This theory reports realistic estimations of time of gelation, and could be used to predict the behavior of the self-assembling peptides under different conditions.

7.2 Future Work

We believe that the results and methods presented in this thesis will open new doors for future works. The understanding of the limitations of the video microscopy particle tracking technique that we presented in chapters 3 and 4 allowed us to improve the resolution of the measurement, and surely to extend the range of applicability of this assessment method. In particular, it is now possible to study stiffer materials with greater confidence. To this regard, corrections for the dynamic errors, that we predict to be a challenging issue, would require more investigations. The statistical sampling design of the measurement, thoroughly described in chapter 5, is a novel study in the field of multiple particle tracking. It allowed us to extract deeper information from the output data of the technique, by deriving almost unbiased estimators for the first two moments of the mean-squared displacement distribution. We expect that a generalization to estimators for higher order moments of this distribution is possible.

The methods developed in this study to confirm the validity of the characterizations presented in chapters 3 to 5 could also be sources of inspiration for future directions. They rely on theoretical models describing the techniques, that are verified through both Brownian dynamics simulations and experiments on well-defined systems. Such experimental systems should be found useful in the demonstration of future theoretical predictions.

Chapter 6 describes how particle tracking can be used to follow gelling systems. This novel approach could be apply to a wide variety of time-evolving systems. We have shown that particle tracking provides with an original, meso-scale view of the mechanism. Our results on self-assembling peptides should be correlated with direct observations of the microstructure, using atomic force microscopy or quick-freeze electronic microscopy of the gel at different time points during its self-assembly.

Appendix A

Noise Characterization and Spatial Resolution

A.1 Noise Characterization

To characterize the noise in our system we used the CCD transfer method described by [130]. This technique provides a robust estimation of the different sources of noise. We observed a sample of fluorescein to evaluate the camera response at similar wavelengths as the beads. Regions of interest that exhibit uniform illumination were chosen on the camera field. For a given illumination, we found that the sources of noise characterized here are independent of the shutter time (see Fig. A.1).

The random pattern-independent noise, that includes the photon shot noise and the signal independent readout noise, is estimated by half the variance of the brightness distribution obtained on the image resulting from the difference between two successive frames taken at the same illumination [131]. When estimated over the whole dynamic range of the camera, we found that this noise contribution is Gaussian distributed (as expected at high-light-level detection), with a variance linearly dependent on the illumination S_{tot} that we estimated by the average brightness value in the sample. Note that S_{tot} is expressed in ADU. We designate this noise contribution by N_{rn} and we write:

$$N_{\text{rn}}^2 = N_{\text{ro}}^2 + \beta_{\text{ps}} \times S_{\text{tot}} \tag{A.1}$$

where we found experimentally $N_{\text{ro}}^2 = 0.05\,\text{ADU}^2$ for our camera readout noise and $\beta_{\text{ps}} = 0.009\,\text{ADU}$ for the photon shot noise coefficient of our setup (Fig. A.1).

The fixed pattern noise, and the photo-response non-uniformity noise estimation are evaluated

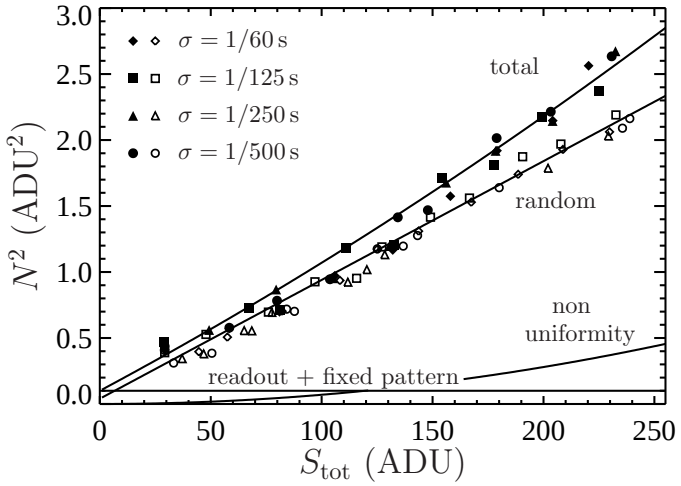

Fig. A.1: Photon transfer curve for our setup. The open symbols designate pattern independent noise estimation, the filled symbols are the total noise measurements. The readout and fixed pattern noise contributions are signal independent, $N_{\rm fp}^2 + N_{\rm ro}^2 = 0.1\,{\rm ADU}^2$, the photon shot noise is $0.009 \times S_{\rm tot}$ and the photo response non-uniformity noise follows $7 \times 10^{-6} \times S_{\rm tot}^2$. The total noise curve is the sum of the four noise contributions and compares well with its experimental estimation, thus proving negligible effects of non-linearity. Note that the photon transfer curve is independent of the shutter time.

in the following manner: the photo response of individual pixel is evaluated independently for 10 different illuminations with 100 frame-long movies being acquired for each illumination. A linear fit of response versus signal is produced for each pixel. The fixed pattern noise is obtain as the variance of the intercept distribution over all the pixels. The photo-response non-uniformity noise coefficient is given by the variance of the slope distribution [131]. The pattern dependent noise $N_{\rm pdn}$ is then written:

$$N_{\rm pd}^2 = N_{\rm fp}^2 + \gamma_{\rm nu} \times S_{\rm tot}^2 \tag{A.2}$$

where we found experimentally $N_{\rm fp}^2 = 0.05\,{\rm ADU}^2$ for the fixed pattern noise and $\gamma_{\rm nu} = 7 \times 10^{-6}$ for the photo response non-uniformity noise coefficient of our camera (see Fig. A.1).

The total noise is the variance of the raw image brightness distribution. Estimated at different illuminations, we found that the total noise compares well with the sum of the random noise with the pattern dependent noise in the whole dynamic range of the camera, indicating that non-linear contributions are negligible (see Fig. A.1).

Another contribution to the total noise in an image can arise from uneven autofluorescence in the sample (in cells for example) or signal from out of focus particles. We call this contribution "background noise" $N_{\rm bg}$. It is negligible in the static experiments we performed in this study, but becomes important in dynamic studies. Finally the total noise is written:

$$N_{\rm tot}^2 = N_{\rm bg}^2 + N_{\rm ro}^2 + N_{\rm fp}^2 + \beta_{\rm ps} \times S_{\rm tot} + \gamma_{\rm nu} \times S_{\rm tot}^2 \ . \tag{A.3}$$

The noise contributions considered here are by nature spatially white, except for the pattern dependent noise and the background noise which might exhibit correlation lengths larger than 1 pxl. The 2D autocorrelation function calculated for regions of an image that are selected by our noise extraction procedure gives information on the distribution of noise correlation lengths. In movie frames obtained from both static and dynamic experiments, we found that the autocorrelation function is sharply peaked at 0 pxl with negligible occurrence at larger lag distances (data not shown). This suggests that a spatially white noise model, as used in the next section of this Appendix, is a reasonable assumption. It is expected that this assumption will hold for many microrheology experiments where a low concentration of probes is usually used in signal-free (e.g., non fluorescent) medium. However, a different conclusion can be reached in other experimental scenarios, where for example out-of-focus autofluorescence of the sample might exhibit large patterns covering several pixels.

In the time domain, we characterized the CCD noise by calculating the power spectral density of the temporal variation of the noise intensity in a movie. We found in both static and dynamic experiments that the noise is temporally white from the frame rate frequency for the upper limit of our spectrum, and at least down to a frequency of 0.1 Hz.

A.2 Relation Between Noise and Spatial Resolution

The multiple particle tracking algorithms we use in this study have been explained in detail elsewhere [16]. In this Appendix we develop a model to relate the spatial resolution of the technique to the noise-to-signal ratio of the data. In the method, movies of particles are acquired using a CCD camera. Usual CCD chips contain 640×480 pxl, and typical trackable particle size have an apparent radius $\hat{a}$ greater than ~ 2 pxl which is usually different from the actual radius a of the bead. The particle position is determined by a brightness weighted average over a circular mask of radius $w > \hat{a}$ applied on the filtered image of the particle. As noticed by [16], if $w < \hat{a}$, clipping of the particle image by the mask deteriorates the resolution. For $w > \hat{a}$, this clipping effect is negligible as compared to the noise contribution, which will be the only consideration retained in the following model. Our aim is to evaluate the position of the particle that is determined from its filtered image. We define $S_{\mathrm{tot}}(\boldsymbol{\rho}, \mathbf{r}) = S_{\mathrm{tot}}(\boldsymbol{\rho} - \mathbf{r})$ the ideal brightness value at a location $\boldsymbol{\rho}$ on the particle image centered at the true position $\mathbf{r} = (x, y)$ ($\mathbf{r} = \mathbf{0}$ in the following). A convenient way to account for noise is to add a spatially white offset $\delta S_{\boldsymbol{\rho}}$ to the ideal brightness profile:

$$\langle \delta S_{\boldsymbol{\rho}} \rangle = 0 \ , \tag{A.4}$$

$$\langle \delta S_{\boldsymbol{\rho}} \, \delta S_{\boldsymbol{\rho}'} \rangle = N_{\mathrm{tot}}^2(\boldsymbol{\rho}) l_{\mathrm{n}}^2 \, \delta(\boldsymbol{\rho} - \boldsymbol{\rho}') \ , \tag{A.5}$$

where l_{n} is the correlation length of the noise, and $N_{\mathrm{tot}}(\boldsymbol{\rho})$ is the noise level. We know from the noise characterization, Eq. A.3, that the noise level depends on the brightness distribution through:

$$N_{\mathrm{tot}}^2(\boldsymbol{\rho}) = N_{\mathrm{bg}}^2 + N_{\mathrm{ro}}^2 + N_{\mathrm{fp}}^2 + \beta_{\mathrm{ps}} \times S_{\mathrm{tot}}(\boldsymbol{\rho}) + \gamma_{\mathrm{nu}} \times S_{\mathrm{tot}}^2(\boldsymbol{\rho}) \ , \tag{A.6}$$

with N_{bg}^2 the background noise, N_{ro}^2 the readout noise, N_{fp}^2 the fixed pattern noise, $\beta_{\mathrm{ps}} \times S_{\mathrm{tot}}(\boldsymbol{\rho})$ the photon shot noise and $\gamma_{\mathrm{nu}} \times S_{\mathrm{tot}}^2(\boldsymbol{\rho})$ the photo-response non-uniformity noise. Also, usual mask sizes satisfy $\pi w^2 \gg l_{\mathrm{n}}^2$ which justifies the use of continuous integrals rather than finite summations. However, we find slight differences between our measurements on pixelized images and the following

model, as discussed in the Results section. Under the continuous assumption, we can infer

$$\int_0^{2\pi}\int_0^{w} \delta S_{\boldsymbol{\rho}} \rho \mathrm{d}\rho\mathrm{d}\theta = 0 \ . \tag{A.7}$$

Depending on the spatial repartition of the noise on the particle image, the brightness-weighted centroid $\hat{x}$ of the filtered image will suffer a shift that we can estimate by the following:

$$\widehat{\overline{x}} - \overline{x} = \frac{\displaystyle\int_0^{2\pi}\int_0^{w} \delta S_{\boldsymbol{\rho}} \ \rho\cos\theta \ \rho\mathrm{d}\rho\mathrm{d}\theta}{\displaystyle\int_0^{2\pi}\int_0^{w} \big[S_{\mathrm{tot}}(\boldsymbol{\rho}) - B\big]\rho\mathrm{d}\rho\mathrm{d}\theta} \ , \tag{A.8}$$

where B designates the background brightness value assumed uniform at the scale of one particle. We then write

$$\overline{\varepsilon}^2 = \Big\langle \big(\widehat{\overline{x}} - \overline{x}\big)^2 \Big\rangle = \frac{l_{\mathrm{n}}^2 \displaystyle\int_0^{2\pi}\int_0^{w} N_{\mathrm{tot}}^2(\boldsymbol{\rho})\rho^2\cos^2\theta \ \rho\mathrm{d}\rho\mathrm{d}\theta}{\left(\displaystyle\int_0^{2\pi}\int_0^{w} \big[S_{\mathrm{tot}}(\boldsymbol{\rho}) - B\big]\rho\mathrm{d}\rho\mathrm{d}\theta\right)^2} \ . \tag{A.9}$$

By assuming a Gaussian brightness distribution for the particle image,

$$S_{\mathrm{tot}}(\boldsymbol{\rho}) = B + S\, e^{-2\boldsymbol{\rho}^2/\hat{a}^2} \ , \tag{A.10}$$

where S is the signal level and $\hat{a}$ is the apparent radius of the particle image, we find

$$\frac{\overline{\varepsilon}^2}{l_{\mathrm{n}}^2} = f_1\big(w/\hat{a}\big) \times \left(\frac{N}{S}\right)^2 + f_2\big(w/\hat{a}\big) \times \frac{\beta_{\mathrm{ps}} + 2\gamma_{\mathrm{nu}} \times B}{S} + f_3\big(w/\hat{a}\big) \times \gamma_{\mathrm{nu}} \ , \tag{A.11}$$

where

$$N^2 = N_{\mathrm{bg}}^2 + N_{\mathrm{ro}}^2 + N_{\mathrm{fp}}^2 + \beta_{\mathrm{ps}} \times B + \gamma_{\mathrm{nu}} \times B^2 \tag{A.12}$$

is the noise amplitude evaluated at the background level and we have introduced the following functional forms:

$$f_1(x) = \frac{1}{4\pi}\left(\frac{2x^2}{1 - e^{-2x^2}}\right)^2 \ , \tag{A.13}$$

$$f_2(x) = \frac{1}{2\pi}\left[\frac{1 - (1 + 2x^2)e^{-2x^2}}{\big(1 - e^{-2x^2}\big)^2}\right] \ , \tag{A.14}$$

$$f_3(x) = \frac{1}{8\pi}\left[\frac{1 - (1 + 4x^2)e^{-4x^2}}{\big(1 - e^{-2x^2}\big)^2}\right] \ . \tag{A.15}$$

Note that Eq. A.11 is formally equivalent, in terms of scaling, to theoretical results obtained by [20]. We can evaluate the order of magnitude of each term for a typical mask size $w = 7\,\mathrm{pxl}$, with typical apparent radius $\hat{a}$ from 4 to 5 pxl; then $f_1 \gtrsim 1.25$, $f_2 \sim 0.15$ and $f_3 \sim 0.04$. Also, in most cases the background level is around $B \sim 50\,\mathrm{ADU}$. Typical values obtained for our camera are: $N_{\mathrm{ro}}^2 = 0.05\,\mathrm{ADU}^2$, $N_{\mathrm{fp}}^2 = 0.05\,\mathrm{ADU}^2$, $\beta_{\mathrm{ps}} = 0.009\,\mathrm{ADU}$, $\gamma_{\mathrm{nu}} = 7 \times 10^{-6}$, and N_{bg}^2 ranging from

$\sim 0\,\mathrm{ADU}^2$ for static experiments to $\sim 2\,\mathrm{ADU}^2$ for dynamic experiments. We find that the first term in Eq. A.11 always dominates in the range S between 10-200 ADU. This justifies both our method for estimating noise in regions without particles as well as our simulations which include only signal independent noise. Furthermore, we will use the following formula obtained by keeping only the first term (in which noise is S independent) of Eq. A.11:

$$\overline{\varepsilon} \sim \frac{N}{S}\frac{l_\mathrm{n}}{2\pi^{1/2}}\left(\frac{2w^2/\hat{a}^2}{1-e^{-2w^2/\hat{a}^2}}\right) , \tag{A.16}$$

as obtained by [16]. A Gaussian profile is usually a good approximation for a typical particle image. However in some cases when the particle is close to the focal plane of the setup, its image presents a flatter peak and sharper edges (see Fig. 3.1*D*). It is thus interesting to consider a flat brightness distribution,

$$S_\mathrm{tot}(\boldsymbol{\rho}) = B + S\mathcal{H}(\hat{a} - |\boldsymbol{\rho}|) , \tag{A.17}$$

where $\mathcal{H}$ is the Heaviside step function. In that case we find the same form to Eq. A.11 with:

$$f_1(x) = \frac{x^4}{4\pi} , \tag{A.18}$$

$$f_2(x) = \frac{1}{4\pi} , \tag{A.19}$$

$$f_3(x) = \frac{1}{4\pi} , \tag{A.20}$$

for which we verify that the first term in Eq. A.11 also dominates. Thus we will write for the hat-like spot:

$$\overline{\varepsilon} \sim \frac{N}{S}\frac{l_\mathrm{n}}{2\pi^{1/2}}\frac{w^2}{\hat{a}^2} . \tag{A.21}$$

Overall, we proved that even though the noise level increases at the particles location due to its signal dependency, this has negligible effect on the spatial resolution. In both cases (Eq. A.16 and Eq. A.21), we find that the spatial resolution is proportional to the noise-to-signal ratio, and the slope depends only on the ratio of the mask area over the particle image area. It is essential at this point to notice that this slope is sensitive to the value of $\hat{a}$: for a typical mask size $2w+1 = 15\,\mathrm{pxl}$, the slope increases more than 30% as the apparent radius of the particle increases from 4 to 5 pxl. Often video particle tracking is performed on half-frames, as single frames are usually composed of two interlaced fields. In that case, both the image and the mask are shrunk by a factor 2 in the direction perpendicular to the interlacing. It is easy to verify that the same result is found for such elliptical masks and particles. However, we explain in the Results section how this de-interlacing of pixelized images affects the measured trajectory.

Appendix B

IDL procedure to calculate statistics

B.1 Usage

At the IDL prompt,

```
Im = MSD_MOMENTS(t [, TimeStep = value] [, MicPerPix = value] [, Mydts = array] $
        [, N_Lag = integer] [, Dim = integer])
```

where

- t is the output array of trajectories from the tracking algorithms.
- TimeStep is the time interval between two consecutive movie frames, in seconds.
- MicPerPix is the on-screen magnification, in microns per pixel.
- Mydts is an array of integers giving the lag times in TimeStep units.
- N_Lag is the number of lag time to make the calculation; an array of N_lag lag times is created for a log scale plot.
- Dim is the dimensionality of the trajectories.

The output array contains the following information (see chapter 5 for notations):

dim=2	dim=1
m[0,*]= τ	m[0,*]= τ
m[1,*]= $\overline{d}_x$	m[1,*]= $\overline{d}_x$
m[2,*]= $\overline{d}_y$	
m[3,*]= $\widehat{M}_{1x}$	m[2,*]= $\widehat{M}_{1x}$
m[4,*]= $\widehat{M}_{1y}$	
m[5,*]= $\widehat{M}_{2x}$	m[3,*]= $\widehat{M}_{2x}$
m[6,*]= $\widehat{M}_{2y}$	
m[7,*]= $\widehat{\mu}_2[\widehat{M}_{1x}]$	m[4,*]= $\widehat{\mu}_2[\widehat{M}_{1x}]$
m[8,*]= $\widehat{\mu}_2[\widehat{M}_{1y}]$	
m[9,*]= $\widehat{\mu}_2[\widehat{M}_{2x}]$	m[5,*]= $\widehat{\mu}_2[\widehat{M}_{2x}]$
m[10,*]= $\widehat{\mu}_2[\widehat{M}_{2y}]$	
m[11,*]= θ	m[6,*]= θ

B.2 IDL code

```
FUNCTION MSD_MOMENTS, t, TimeStep = TimeStep, MicPerPix = MicPerPix, Mydts = Mydts, $
  N_Lag = N_Lag, Dim = Dim, FileName = FileName

IF NOT KEYWORD_SET(TimeStep) THEN TimeStep = 1d ELSE TimeStep = DOUBLE(TimeStep)
IF NOT KEYWORD_SET(MicPerPix) THEN MicPerPix = 1d ELSE MicPerPix = DOUBLE(MicPerPix)
IF NOT KEYWORD_SET(Dim) THEN Dim = 2
IF NOT KEYWORD_SET(Filename) THEN Filename = 0

Dim_t = N_ELEMENTS(t[*,0])
Ind_Id = Dim_t - 1
Ind_Time = Dim_t - 2

; Characteristics of the trajectories
Id_Pos = UNIQ( t[Ind_Id,*] )      ; Subscript of the end
N_Id = N_ELEMENTS( Id_Pos )       ; Number
Id = t[Ind_Id,Id_Pos]             ; Identities
Id_Length = Id_Pos - SHIFT(Id_Pos,1) - 1 & $
  Id_Length[0] = Id_Pos[0]        ; Number of displacement at lag=1

; Create the list of Lag
Max_Lag = (N_Id GE 2) ? Id_Length[ (SORT(Id_Length))[N_Id-2] ] : MAX(Id_Length) - 1
IF KEYWORD_SET(Mydts) THEN BEGIN
    Lag = LONG(Mydts[WHERE(Mydts LE Max_Lag)])
ENDIF ELSE BEGIN
    IF NOT KEYWORD_SET(N_Lag) THEN N_Lag = 50
    IF (Max_Lag LE N_Lag) THEN Lag = LINDGEN(Max_Lag)+1 ELSE BEGIN
        N_Ind = N_Lag-1
        REPEAT BEGIN
            N_Ind++
            Index = DINDGEN(N_Ind)/(N_Ind-1)
            Lag = ROUND(Max_Lag^Index)
            Lag = Lag[UNIQ(Lag)]
```

```
        ENDREP UNTIL N_ELEMENTS(Lag) EQ N_Lag
    ENDELSE
ENDELSE
N_Lag = N_ELEMENTS(Lag)

; Calculate N_box
Time = t[Ind_Time,SORT(t[Ind_Time,*])]
Time_Pos = UNIQ(Time)
N_box = Time_Pos - SHIFT(Time_Pos,1) & N_box[0] = Time_Pos[0] + 1
N_box = TOTAL( N_box, /DOUBLE ) / N_ELEMENTS( N_Box )

; Pos, Time, Id
xy_Id = TRANSPOSE( [ t[0:Dim-1,*] * $
                     REBIN([MicPerPix],Dim,N_ELEMENTS(t[0,*]),/SAMPLE), $
                     t[ [Ind_Time,Ind_Id], * ] ] )

Result = DBLARR(7*Dim+3,N_Lag,/NOZERO) + !VALUES.D_NAN
Result[0,*] = Lag * TimeStep


FOR j=0, N_Lag - 1 DO BEGIN

   ; List of Displacements
    dx = xy_Id - SHIFT( xy_Id, Lag[j], 0 )
    dx = dx[ WHERE( (dx[*,Dim] EQ Lag[j]) AND (dx[*,Dim+1] EQ 0), N_dx), 0:Dim-1]

    ; Individual particle positions
    W_Good = WHERE(Id_Length GE Lag[j], N_Id)
    Norm = TOTAL(Id_Length[W_Good]+0)
    Id_Length = Id_Length[W_Good]
    N_dx_I = Id_Length + 1 - Lag[j]
    Pos_Low = (N_Id EQ 1) ? 0 : $
              [0, TOTAL(N_dx_I[0:N_Id-2], /CUMULATIVE, /PRESERVE_TYPE)]

    ; Weights
    Weight = DBLARR(N_dx, /NOZERO)
    FOR i = 0, N_Id - 1 DO Weight[Pos_Low[i]] = $
      DBLARR(N_dx_I[i]) + ( Id_Length[i] + 0 )/ DOUBLE( N_dx_I[i] )
    Weight = REBIN(TEMPORARY(Weight), N_dx, Dim) / Norm

    dxb = TOTAL(dx,1) / N_dx
    dx = dx - ( dx[*,0]*0 + 1 ) # dxb
    dx2b = TOTAL( Weight * dx^2, 1 )
    dx4b = TOTAL( Weight * dx^4, 1 )
    dx6b = TOTAL( Weight * dx^6, 1 )
    dx8b = TOTAL( Weight * dx^8, 1 )

    N_Seg = Lag[j]
    ; First the one for which N_dx_I ge N_Seg
    W_Good = WHERE(N_dx_I GE N_Seg, N_Good, COMPLEMENT = W_Bad, NCOMPLEMENT = N_Bad)
    IF N_Good GE 1 THEN BEGIN
        N_dx_I_Good = N_dx_I[W_Good] - (N_dx_I[W_Good] MOD N_Seg)
        Pos_Good = [0, TOTAL(N_dx_I_Good, /CUMULATIVE, /PRESERVE_TYPE)]
        Good = LONARR(Pos_Good[N_Good], /NOZERO)
        Weight = Good * 0D
```

```
        FOR i = 0, N_Good - 1 DO BEGIN
            Good[Pos_Good[i]] = Pos_Low[ W_Good[i] ] + LINDGEN( N_dx_I_Good[i] )
            Weight[Pos_Good[i]] = DBLARR(N_dx_I_Good[i])+ $
              ( Id_Length[ W_Good[i] ] + 0 ) / DOUBLE( N_dx_I_Good[i] / N_Seg )
        ENDFOR
        n = Pos_Good[N_Good] / N_seg
        Weight = REBIN(TEMPORARY(Weight), n, Dim)
        dx_2 = REBIN(dx[Good,*]^2, n, Dim)
        dx_4 = REBIN(dx[Good,*]^4, n, Dim)
        dx_6 = REBIN(dx[Good,*]^6, n, Dim)
    ENDIF

    ; Then the rest that bring only one
    IF N_Bad GE 1 THEN BEGIN
        FOR i = 0, N_Bad - 1 DO BEGIN
            dx_I = dx[Pos_Low[W_Bad[i]]:Pos_Low[W_Bad[i]]+N_dx_I[W_Bad[i]]-1]
            Weight =( (N_Good EQ 0) && (i EQ 0) ) ? $
              REBIN([Id_Length[W_Bad[i]]], 1, Dim) : $
              [Weight, REBIN([Id_Length[W_Bad[i]]], 1, Dim)]
            dx_2 = ( (N_Good EQ 0) && (i EQ 0) ) ? $
              REBIN(dx_I^2, 1, Dim) : [dx_2, REBIN(dx_I^2, 1, Dim)]
            dx_4 = ( (N_Good EQ 0) && (i EQ 0) ) ? $
              REBIN(dx_I^4, 1, Dim) : [dx_4, REBIN(dx_I^4, 1, Dim)]
            dx_6 = ( (N_Good EQ 0) && (i EQ 0) ) ? $
              REBIN(dx_I^6, 1, Dim) : [dx_6, REBIN(dx_I^6, 1, Dim)]
        ENDFOR
    ENDIF

    n = (N_Good EQ 0) ? N_Bad : ( n + N_Bad )

    Weight = TEMPORARY(Weight) / Norm

    dx_22b = TOTAL(Weight * dx_2^2,1)
    dx_42b = TOTAL(Weight * dx_4^2,1)
    dx_2dx_4b = TOTAL(Weight * dx_2*dx_4,1)

    M_4 = dx8b/105 - 4*dx2b*dx6b/15 + 2*dx2b^2*dx4b - 3*dx2b^4

    Result[0*Dim+1,j] = dxb
    Result[1*Dim+1,j] = dx2b
    Result[2*Dim+1,j] = dx4b/3-dx2b^2+(dx_22b-dx2b^2) * $
                        TOTAL(Weight^2)/ TOTAL(Weight*(1-Weight))
    Result[3*Dim+1,j] = (dx_22b-dx2b^2)* TOTAL(Weight^2)/ TOTAL(Weight*(1-Weight)) + $
                        (dx4b/3-dx2b^2+(dx_22b-dx2b^2) * $
                         TOTAL(Weight^2)/ TOTAL(Weight*(1-Weight)))/N_box
    Result[4*Dim+1,j] = ((dx_42b-dx4b^2)/9+4*dx2b^2*(dx_22b-dx2b^2)+ $
                         4*dx2b*(dx2b*dx4b-dx_2dx_4b)/3) * $
                        TOTAL(Weight^2)/ TOTAL(Weight) + $
                        (dx8b/105 - 4*dx2b*dx6b/15 + 2*dx2b^2*dx4b - $
                         3*dx2b^4 - (dx4b/3-dx2b^2)^2)/N_box
    Result[5*Dim+1,j] = N_dx / $
                        (N_box * ( MAX(t[Ind_Time,*])-MIN(t[Ind_Time,*]) + 1 - Lag[j] ))
    Result[6*Dim+1,j] = TOTAL(Id_Length + 1) / $
                        (N_box * ( MAX(t[Ind_Time,*])-MIN(t[Ind_Time,*]) + 1 ))
ENDFOR
```

```
RETURN, Result

END
```

Bibliography

[1] J. N. Israelachvili, *Intermolecular and Surface Forces;* Academic Press, London, UK, 1985.

[2] W. B. Russel, D. A. Saville, and W. R. Schowalter, *Colloidal Dispersions;* Cambridge University Press, Cambridge, UK, 1989.

[3] M. D. Haw, *J. Phys.: Condens. Matter*, **2002**, *14*, 7769–7779.

[4] M. J. Nye, *Molecular Reality;* Macdonald, London, UK, 1972.

[5] J. Gelles, B. J. Schnapp, and M. P. Sheetz, *Nature*, **1988**, *331*, 450–453.

[6] A. Yildiz, J. N. Forkey, S. A. McKinney, T. Ha, Y. E. Goldman, and P. R. Selvin, *Science*, **2003**, *300*, 2061–2065.

[7] G. Seisenberger, M. U. Ried, T. Endress, H. Buning, M. Hallek, and C. Brauchle, *Science*, **2001**, *294*, 1929–1932.

[8] M. J. Saxton and K. Jacobson, *Annu. Rev. Biophys. Biomolec. Struct.*, **1997**, *26*, 373–399.

[9] T. G. Mason and D. A. Weitz, *Phys. Rev. Lett*, **1995**, *74*, 1250–1253.

[10] D. T. Chen, E. R. Weeks, J. C. Crocker, M. F. Islam, R. Verma, J. Gruber, A. J. Levine, T. C. Lubensky, and A. G. Yodh, *Phys. Rev. Lett.*, **2003**, *90*, 108301.

[11] J. Apgar, Y. Tseng, E. Fedorov, M. B. Herwig, S. C. Almo, and D. Wirtz, *Biophys. J.*, **2000**, *79*, 1095–1106.

[12] M. T. Valentine, P. D. Kaplan, D. Thota, J. C. Crocker, T. Gisler, R. K. Prud'homme, M. Beck, and D. A. Weitz, *Phys. Rev. E*, **2001**, *64*, 061506.

[13] C. A. Murray, W. O. Sprenger, and R. A. Wenk, *Phys. Rev. B*, **1990**, *42*, 688–703.

[14] J. C. Crocker and D. G. Grier, *Phys. Rev. Lett.*, **1994**, *73*, 352–355.

[15] M. K. Cheezum, W. F. Walker, and W. H. Guilford, *Biophys. J.*, **2001**, *81*, 2378–2388.

[16] J. C. Crocker and D. G. Grier, *J. Colloid Interface Sci.*, **1996**, *179*, 298–310.

[17] S. Inoué and K. R. Spring, *Video Microscopy: The Fundamentals;* Plenum Press, New York, NY, 2nd ed., 1997.

[18] U. Kubitscheck, O. Kuckmann, T. Kues, and R. Peters, *Biophys. J.*, **2000**, *78*, 2170–2179.

[19] M. Goulian and S. M. Simon, *Biophys. J.*, **2000**, *79*, 2188–2198.

[20] R. E. Thompson, D. R. Larson, and W. W. Webb, *Biophys. J.*, **2002**, *82*, 2775–2783.

[21] W. Denk and W. W. Webb, *Appl. Optics*, **1990**, *29*, 2382–2391.

[22] T. G. Mason, K. Ganesan, J. H. van Zanten, D. Wirtz, and S. C. Kuo, *Phys. Rev. Lett.*, **1997**, *79*, 3282–3285.

[23] S. Yamada, D. Wirtz, and S. C. Kuo, *Biophys. J.*, **2000**, *78*, 1736–1747.

[24] R. G. Larson, *The Structure and Rheology of Complex Fluids;* Oxford University Press, Oxford, UK, 1999.

[25] R. B. Bird, R. C. Armstrong, and O. Hassager, *Dynamics of Polymeric Liquids;* John Wiley & Sons, New York, NY, 1987.

[26] F. C. MacKintosh and C. F. Schmidt, *Curr. Opin. Colloid Interface Sci.*, **1999**, *4*, 300.

[27] T. A. Waigh, *Rep. Prog. Phys.*, **2005**, *68*, 685–742.

[28] M. L. Gardel, M. T. Valentine, and D. A. Weitz; Microrheology; In K. Breuer, Eds., *Microscale Diagnostic Techniques*. Springer-Verlag, New York, NY, 2005.

[29] Y. Tseng and D. Wirtz, *Biophys. J.*, **2001**, *81*, 1643–1656.

[30] Q. Lu and M. J. Solomon, *Phys. Rev. E*, **2002**, *66*, 061504.

[31] V. Breedveld and D. J. Pine, *J. Mater. Sci.*, **2003**, *38*, 4461–4470.

[32] J. Sato and V. Breedveld, *J. Rheol.*, **2006**, *50*, 1–19.

[33] B. R. Dasgupta, S.-Y. Tee, J. C. Crocker, B. J. Frisken, and D. A. Weitz, *Phys. Rev. E*, **2002**, *65*, 051505.

[34] B. Schnurr, F. Gittes, F. C. MacKintosh, and C. F. Schmidt, *Macromolecules*, **1997**, *30*, 7781–7792.

[35] F. Gittes, B. Schnurr, P. D. Olmsted, F. C. MacKintosh, and C. F. Schmidt, *Phys. Rev. Lett.*, **1997**, *79*, 3286–3289.

[36] T. G. Mason, K. Ganesan, J. H. van Zanten, D. Wirtz, and S. C. Kuo, *J. Opt. Soc. Am. A*, **1997**, *14*, 139–149.

[37] T. G. Mason, *Rheol. Acta*, **2000**, *39*, 371–378.

[38] A. J. Levine and T. C. Lubensky, *Phys. Rev. E*, **2001**, *63*, 041510.

[39] M. J. Solomon and Q. Lu, *Curr. Opin. Colloid Interface Sci.*, **2001**, *6*, 430.

[40] J. L. McGrath, J. H. Hartwig, and S. C. Kuo, *Biophys. J.*, **2000**, *79*, 3258–3266.

[41] M. T. Valentine, Z. E. Perlman, M. L. Gardel, J. H. Shin, P. Matsudaira, T. J. Mitchison, and D. A. Weitz, *Biophys. J.*, **2004**, *86*, 4004–4014.

[42] B. S. Chae and E. M. Furst, *Langmuir*, **2005**, *21*, 3084–3089.

[43] P. Panorchan, D. Wirtz, and Y. Tseng, *Phys. Rev. E*, **2004**, *70*, 041906.

[44] M. Speidel, A. Jonáš, and E. L. Florin, *Opt. Lett.*, **2003**, *28*, 69–71.

[45] S. Hell, G. Reiner, C. Cremer, and E. H. K. Stelzer, *J. Microsc.*, **1993**, *169*, 391–405.

[46] I. Y. Wong, M. L. Gardel, D. R. Reichman, E. R. Weeks, M. T. Valentine, A. R. Bausch, and D. A. Weitz, *Phys. Rev. Lett.*, **2004**, *92*, 178101.

[47] S. Redner, *A Guide to First-Passage Processes;* Cambridge University Press, Cambridge, UK, 2001.

[48] D. S. Martin, M. B. Forstner, and J. A. Kas, *Biophys. J.*, **2002**, *83*, 2109–2117.

[49] N. Bobroff, *Rev. Sci. Instrum.*, **1986**, *57*, 1152–1157.

[50] A. Papoulis, *Probability, Random Variables, and Stochastic Processes;* McGraw-Hill, New York, NY, 3rd ed., 1991.

[51] M. Keller, J. Schilling, and E. Sackmann, *Rev. Sci. Instrum.*, **2001**, *72*, 3626.

[52] H. C. Öttinger, *Stochastic Processes in Polymeric Fluids: Tools and Examples for Developing Simulation Algorithms;* Springer-Verlag, New York, NY, 1996.

[53] W. K. Pratt, *Digital Image Processing;* John Wiley & Sons, New York, NY, 2nd ed., 1991.

[54] Y. C. Fung, *Biomechanics: Mechanical Properties of Living Tissues;* Springer-Verlag, New York, NY, 2nd ed., 1993.

[55] A. R. Bausch, F. Ziemann, A. A. Boulbitch, K. Jacobson, and E. Sackmann, *Biophys. J.*, **1998**, *75*, 2038–2049.

[56] B. Fabry, G. N. Maksym, J. P. Butler, M. Glogauer, D. Navajas, and J. J. Fredberg, *Phys. Rev. Lett.*, **2001**, *87*, 148102.

[57] J. H. van Zanten and K. P. Rufener, *Phys. Rev. E*, **2000**, *62*, 5389–5396.

[58] M. J. Lang and S. M. Block, *Am. J. Phys.*, **2003**, *71*, 201–215.

[59] R. Yasuda, H. Miyata, and K. Kinosita, *J. Mol. Biol.*, **1996**, *263*, 227–236.

[60] P. M. Chaikin and T. C. Lubensky, *Principles of Condensed Matter Physics;* Cambridge University Press, Cambridge, UK, 1995.

[61] V. S. Volkov and A. I. Leonov, *J. Chem. Phys.*, **1996**, *104*, 5922.

[62] K. Schätzel, M. Drewel, and S. Stimac, *J. Mod. Opt.*, **1988**, *35*, 711.

[63] M. Doi and S. F. Edwards, *The Theory of Polymer Dynamics;* Oxford University Press, Oxford, UK, 1986.

[64] J. Quintanilla, *Polym. Eng. Sci.*, **1999**, *39*, 559–585.

[65] Y. Tseng, K. M. An, and D. Wirtz, *J. Biol. Chem.*, **2002**, *277*, 18143–18150.

[66] Y. Tseng and D. Wirtz, *Phys. Rev. Lett.*, **2004**, *93*, 258104.

[67] K. Luby-Phelps, P. E. Castle, D. L. Taylor, and F. Lanni, *Proc. Natl. Acad. Sci. U.S.A.*, **1987**, *84*, 4910–4913.

[68] K. Luby-Phelps, F. Lanni, and D. L. Taylor, *Annu. Rev. Biophys. Biophys. Chem.*, **1988**, *17*, 369–396.

[69] C. S. Chen, M. Mrksich, S. Huang, G. M. Whitesides, and D. E. Ingber, *Science*, **1997**, *276*, 1425–1428.

[70] C.-M. Lo, H.-B. Wang, M. Dembo, and Y.-l. Wang, *Biophys. J.*, **2000**, *79*, 144–152.

[71] S. Gheorghiu and M.-O. Coppens, *Proc. Natl. Acad. Sci. U.S.A.*, **2004**, *101*, 15852–15856.

[72] N. D. Gershon, K. R. Porter, and B. L. Trus, *Proc. Natl. Acad. Sci. U.S.A.*, **1985**, *82*, 5030–5034.

[73] N. Pernodet, M. Maaloum, and B. Tinland, *Electrophoresis*, **1997**, *18*, 55–58.

[74] W. W. Graessley, *Polymeric Liquids & Networks: Structure and Properties;* Garland Science, New-York, NY, 2003.

[75] A. R. Kannurpatti, K. J. Anderson, J. W. Anseth, and C. N. Bowman, *J. Polym. Sci. Part B: Polym. Phys.*, **1997**, *35*, 2297 – 2307.

[76] I. M. Tolić-Nørrelykke, E.-L. Munteanu, G. Thon, L. Oddershede, and K. Berg-Sørensen, *Phys. Rev. Lett.*, **2004**, *93*, 078102.

[77] Y. Tseng, T. P. Kole, and D. Wirtz, *Biophys. J.*, **2002**, *83*, 3162–3176.

[78] A. Goodman, Y. Tseng, and D. Wirtz, *J. Mol. Biol.*, **2002**, *323*, 199–215.

[79] J. H. Shin, M. L. Gardel, L. Mahadevan, P. Matsudaira, and D. A. Weitz, *Proc. Natl. Acad. Sci. U.S.A.*, **2004**, *101*, 9636–9641.

[80] I. A. Hasnain and A. M. Donald, *Phys. Rev. E*, **2006**, *73*, 031901.

[81] J. C. Crocker, M. T. Valentine, E. R. Weeks, T. Gisler, P. D. Kaplan, A. G. Yodh, and D. A. Weitz, *Phys. Rev. Lett.*, **2000**, *85*, 888–891.

[82] A. J. Levine and T. C. Lubensky, *Phys. Rev. Lett.*, **2000**, *85*, 1774–1777.

[83] A. Rahman, *Phys. Rev.*, **1964**, *136*, A405–A411.

[84] W. K. Kegel and A. van Blaaderen, *Science*, **2000**, *287*, 290–293.

[85] E. R. Weeks, J. C. Crocker, A. C. Levitt, A. Schofield, and D. A. Weitz, *Science*, **2000**, *287*, 627–631.

[86] R. Tharmann, M. M. A. E. Claessens, and A. R. Bausch, *Biophys. J.*, **2006**, *90*, 2622–2627.

[87] D. D. Boos and C. Brownie, *Statist. Sci.*, **2004**, *19*, 571578.

[88] H. Flyvbjerg and H. G. Petersen, *J. Chem. Phys.*, **1989**, *91*, 461–466.

[89] J. C. Love, D. B. Wolfe, H. O. Jacobs, and G. M. Whitesides, *Langmuir*, **2001**, *17*, 6005–6012.

[90] D. Dendukuri, D. C. Pregibon, J. Collins, T. A. Hatton, and P. S. Doyle, *Nature Mat.*, **2006**, *5*, 365369.

[91] G. M. Whitesides, J. P. Mathias, and C. T. Seto, *Science*, **1991**, *254*, 1312–1319.

[92] S. Zhang, *Biotech. Adv.*, **2002**, *20*, 321–339.

[93] S. Zhang, *Nature Biotech.*, **2003**, *21*, 1171–1178.

[94] S. Zhang, T. Holmes, C. Lockshin, and A. Rich, *Proc. Natl. Acad. Sci. U.S.A.*, **1993**, *90*, 3334–3338.

[95] T. C. Holmes, S. de Lacalle, X. Su, G. Liu, A. Rich, and S. Zhang, *Proc. Natl. Acad. Sci. U.S.A.*, **2000**, *97*, 6728–6733.

[96] J. Kisiday, M. Jin, B. Kurz, H. Hung, C. Semino, S. Zhang, and A. J. Grodzinsky, *Proc. Natl. Acad. Sci. U.S.A.*, **2002**, *99*, 9996–10001.

[97] S. Zhang, D. M. Marini, W. Hwang, and S. Santoso, *Curr. Opin. Chem. Biol.*, **2002**, *6*, 865–871.

[98] D. M. Marini, W. Hwang, D. A. Lauffenburger, S. Zhang, and R. D. Kamm, *Nano Lett.*, **2002**, *2*, 295–299.

[99] M. R. Caplan, P. N. Moore, S. Zhang, R. D. Kamm, and D. A. Lauffenburger, *Biomacromolecules*, **2000**, *1*, 627–631.

[100] J. D. Hartgerink, E. Beniash, and S. I. Stupp, *Science*, **2001**, *294*, 1684–1688.

[101] J. D. Hartgerink, E. Beniash, and S. I. Stupp, *Proc. Natl. Acad. Sci. U.S.A.*, **2002**, *99*, 5133–5138.

[102] A. P. Nowak, V. Breedveld, L. Pakstis, B. Ozbas, D. J. Pine, D. Pochan, and T. J. Deming, *Nature*, **2002**, *417*, 424–428.

[103] W. A. Petka, J. L. Harden, K. P. McGrath, D. Wirtz, and D. A. Tirrell, *Science*, **1998**, *281*, 389–392.

[104] S. Zhang, C. Lockshin, R. Cook, and A. Rich, *Biopolymers*, **1994**, *34*, 663–672.

[105] W. Hwang, D. M. Marini, R. D. Kamm, and S. Zhang, *J. Chem. Phys.*, **2003**, *118*, 389–397.

[106] E. J. Leon, N. Verma, S. Zhang, D. A. Lauffenburger, and R. D. Kamm, *J. Biomater. Sci. Polymer Edn*, **1998**, *9*, 297–312.

[107] M. R. Caplan, E. M. Schwartzfarb, S. Zhang, R. D. Kamm, and D. A. Lauffenburger, *Biomaterials*, **2002**, *23*, 219–227.

[108] W. Hwang, S. Zhang, R. D. Kamm, and M. Karplus, *Proc. Natl. Acad. Sci. U.S.A.*, **2004**, *101*, 12916–12921.

[109] M. Balbirnie, R. Grothe, and D. S. Eisenberg, *Proc. Natl. Acad. Sci. U.S.A.*, **2001**, *98*, 2375–2380.

[110] M. R. Caplan, E. M. Schwartzfarb, S. Zhang, R. D. Kamm, and D. A. Lauffenburger, *J. Biomater. Sci. Polymer Edn.*, **2002**, *13*, 225–236.

[111] C. Heinemann, F. Cardinaux, F. Scheffoldb, P. Schurtenbergerb, F. Eschera, and B. Conde-Petit, *Carbo-. hydr. Polym.*, **2004**, *55*, 155–161.

[112] R. P. Slopek, H. McKinley, C. L. Henderson, and V. Breedveld, *Polymer*, **2006**, *47*, 2263–2268.

[113] L. Stryer, *Biochemistry;* W. H. Freeman and Company, New York, NY, 2000.

[114] P. J. Kundrotas and A. Karshikoff, *Phys. Rev. E*, **2001**, *65*, 011901.

[115] H. H. Winter and F. Chambon, *J. Rheol.*, **1986**, *30*, 367–382.

[116] H. H. Winter and M. M. Mours, *Adv. Polym. Sci.*, **1997**, *134*, 165–234.

[117] J. E. Martin, D. Adolf, and J. P. Wilcoxon, *Phys. Rev. Lett.*, **1988**, *61*, 2620–2623.

[118] C. P. Lusignan, T. H. Mourey, J. C. Wilson, and R. H. Colby, *Phys. Rev. E*, **1995**, *52*, 6271–6280.

[119] D. Adolf, J. E. Martin, and J. P. Wilcoxon, *Macromolecules*, **1990**, *23*, 527 – 531.

[120] W. Hess, T. A. Vilgis, and H. H. Winter, *Macromolecules*, **1988**, *21*, 2536 – 2542.

[121] P. C. Hiemenz and R. Rajagopalan, *Principles of Colloid and Surface Chemistry;* Marcel Dekker, New-York, NY, 1997.

[122] V. A. Davis, L.M. Ericson, A. N. G. Parra-Vasquez, H. Fan, Y. Wang, V. Prieto, J. A. Longoria, S. Ramesh, R. K. Saini, C. Kittrell, W. E. Billups, W. W. Adams, R. H. Hauge, R. E. Smalley, and M. Pasquali, *Macromolecules*, **2004**, *37*, 154–160.

[123] H. Ohshima, *J. Colloid Interface Sci.*, **1998**, *200*, 291–297.

[124] D. Leckband and S. Sivasankar, *Colloids Surf. B, Biointerfaces*, **1999**, *14*, 83–97.

[125] J. J. Grigsby, H. W. Blanch, and J. M. Prausnitz, *Biophys. Chem.*, **2002**, *99*, 107–116.

[126] S. Nir, *Prog. Surf. Sci.*, **1976**, *8*, 1–58.

[127] C. M. Roth, B. L. Neal, and A. M. Lenhoff, *Biophys. J.*, **1996**, *70*, 977–987.

[128] F. W. Tavares, D. Bratko, H. W. Blanch, and J. M. Prausnitz, *Journal of Physical Chemistry B*, **2004**, *108*, 9228–9235.

[129] H. Yokoi, T. Kinoshita, and S. Zhang, *Proc. Natl. Acad. Sci. U.S.A.*, **2005**, *102*, 8414–8419.

[130] J. R. Janesick, K. P. Klaasen, and T. Elliott, *Opt. Eng.*, **1987**, *26*, 972–980.

[131] Y. Reibel, M. Jung, M. Bouhifd, B. Cunin, and C. Draman, *Eur. Phys. J.-Appl. Phys*, **2003**, *21*, 75–80.